Coastal Carolina University

CCU Digital Commons

Summer 8-1-2023

Ocean Wave-Coherent Temperature and Humidity Near-Surface Vertical Distributions and Their Effect on Radar Performance over the Ocean

Mathew James Stanek
Coastal Carolina University

Recommended Citation

Ocean Wave-Coherent Temperature and Humidity Near-Surface Vertical Distributions
and Their Effect on Radar Performance over the Ocean
By

Mathew James Stanek

Submitted in Partial Fulfillment of the

Requirements for the Degree of Doctor of Philosophy in

Marine Science: Coastal and Marine Systems Science in the

Gupta College of Science

Coastal Carolina University

2023

X

Erin E. Hackett, Ph.D., Advisor
Coastal Carolina University

X

Diane Fribance, Ph.D., Committee
Coastal Carolina University

X

Craig Gilman, Ph.D., Committee
Coastal Carolina University

X

Anne Fullerton, Ph.D., Committee
Naval Surface Warfare Center - Carderock Di...

X

Roberto Padilla-Hernandez, Ph.D., Committee
Fleet Numerical Meterology and Oceanogra...

X

Erin Hackett, Ph.D.
CMSS Graduate Programs Director

X

Chad Leverette, Ph.D.
Dean, Gupta College of Science

Dedication

For my paternal grandparents,

Howard and Bev. Stanek, who I lost along the way of this academic pursuit.

Acknowledgements

Abstract

Large knowledge gaps concerning the effect of ocean surface waves on near-surface vertical distributions of temperature and humidity in the marine atmospheric surface layer exist due to practical limitations and sensor fidelity challenges of direct measurements. Wave effects on these distributions between the wave trough and crest are least studied within the literature. These scalar distributions influence atmospheric refractivity, which can lead to anomalous propagation of electromagnetic energy. Measurements of temperature and humidity are classically made using rocket- or radiosondes and fixed weather stations, and can utilize tethered profiling systems. However, these measurement systems have limitations when obtaining measurements near the sea surface. Consequently, boundary layer similarity models (i.e., Monin Obuhkov (MO) theory) are commonly employed to fill in these near-surface measurement gaps despite the documented shortcomings of these models in this region. To address this observational gap, this research develops a novel near-surface wave-coherent instantaneous profiling system (NWIPS) to aid in enriching our current knowledge regarding the influence of waves on near-surface vertical scalar distributions. Eighty minutes of wave-coherent instantaneous vertical scalar distributions were measured by NWIPS in an unstable atmosphere. It is the first attempt to obtain high resolution, wave-coherent vertical distributions of temperature and humidity within the lowest 3 m of altitude. Utilizing these measurements, the variability of near-surface vertical scalar distributions is investigated. These results are

discussed in the context of their impact on propagation loss predictions for X-band and K-band frequencies.

Comparisons between classical MO theory profiles and NWIPS measured profiles showed disagreement below 4 m, whereas above this altitude, there was good agreement. Comparisons between PL predictions for the two refractivity profiles revealed lower propagation loss at long range for MO theory, and differences are most significant for K-band. Below 4 m, distinct, persistent, vertical structure in both ten-minute and 80-minute ensembles and 80-minute wave phase-averaged vertical scalar profiles were observed. The complex structure in the mean temperature vertical distribution near the surface is consistent with prior laboratory and numerical studies. Variations in refractivity over wave phase showed the primary difference between refractivity profiles at the crest, trough, upslope, and downslope was the vertical shifting of the profiles resulting from the shifting surface. The phase-averaged profiles were also found to be steady over the 80-minute experiment consistent with the similar wave conditions during this time. The differences in the refractivity profiles for the various wave phases are shown to be relatively insignificant to X-band propagation predictions, while for K-band some discrepancies are observed over both flat and wavy surfaces. The differences resulting from the duct height shifting in range and/or the introduction of a wavy surface causes larger differences in propagation predictions than do changes in the refractivity profile with phase.

Table of Contents

List of Tables

List of Figures

List of Abbreviations and Acronyms

AHRS ....Attitude Heading Reference System
CASPER .... Coupled Air-Sea Processes and Electromagnetic Ducting Research
CE .... Coastal Explorer
COARE ....Coupled Ocean Atmosphere Response Experiment
ED ....Evaporation Duct
EDH ....Evaporation Duct Height
EM ....Electromagnetic
FLIP .... FLoating Instrument Platform
HEXOS ....Humidity Exchange Over the Sea
LES ....Large Eddy Simulation
MAD ....Mean Absolute Difference
MAPS.. Marine Atmospheric Profiling System
MASL ....Marine Atmospheric Surface Layer
MO ....Monin Obukhov
MSL .... Mean Sea Level
MWL .... Mean Water Level
NAVSLaM ....Navy's Atmospheric Vertical Surface Layer Model
NDBC ....National Data Buoy Center
NOAA ....National Oceanic and Atmospheric Administration
NWP .... Numerical Weather Prediction
NWIPS ....Near-Surface Wave-coherent Instantaneous Profiling System
PVC ....PolyVinyl Chloride
R/P... Research Platform
R/V ....Research Vessel
RF ....Radio Frequency
RMSE ....Root Mean Squared Error
TOGA ....Tropical Ocean Global Atmospheres
VTRPE ....Variable Terrain Radio-wave Parabolic Equation

List of Symbols

c Wave phase speed

e_p Partial vapor pressure

f_0 Empirical fit constant

f_1 Empirical fit constant

f_2 Empirical fit constant

f_p Peak spectral energy

g Acceleration due to gravity

H_s Significant wave height

L Obukhov length

L_w Wavelength

M Modified refractivity

M_{fit} Modified refractivity fit

m_0 Zeroth moment of wave spectrum

P Pressure

P_w Atmospheric pressure from windsond

P_{atm} Surface level pressure

P_{abs} Absolute pressure

q Specific humidity

q_0 Surface specific humidity

q_{*0} Specific humidity surface scaling

R_e Radius of earth

R_r Reynolds roughness number

r	$\sqrt[3]{1 - \gamma_1 \zeta}$
T	Temperature
T_B	Bulk sea-surface temperature
T_p	Peak wave period
T_v	Absolute virtual temperature
T_{lw}	Temperature under low wind conditions
T_{hw}	Temperature under high wind conditions
t	Time
U	Mean wind speed
U_{10}	Wind speed at 10 meters
u	Horizontal wind component
u_f	Free convective momentum scaling parameter
u_*	Friction velocity
u_{*0}	Friction velocity at the surface
x	$(1 - \gamma_1 \zeta)^{1/4}$
y	$(1 - \gamma_2 \zeta)^{1/2}$
z	Altitude
z_d	Evaporation duct height
z_q	Humidity surface roughness length
z_T	Temperature surface roughness length
z_0	Aerodynamic surface roughness length
w	Vertical wind component
w'	Vertical turbulent wind component
α_c	Charnock constant [0.012 – 0.035]
α_1	Empirical free convective constant [~0.7]
β_1	Empirical coefficient [4.7-6.9; 4.7 -9.2]
γ_1	Empirical coefficient [16-28]

γ_2 Empirical coefficient [9-14]

ΔT_l Low wind sea-surface temperature correction

ΔT_h High wind sea-surface temperature correction

ΔT_{local} Local sea-surface temperature correction

δM Modified index of refraction deficit

ε Wind induced pitch angle

ζ Dimensionless stability parameter

η Surface elevation

θ Potential temperature

θ_f Free convective temperature scaling parameter

θ_0 Surface potential temperature

θ_v Virtual potential temperature

θ_{v*0} Virtual potential temperature surface scaling

θ_v' Turbulent virtual potential temperature

κ von Karman constant

λ_m Maximum trapped wavelength

φ Skin sea-surface temperature

ν Kinematic viscosity

ρ_w Density of water

Φ_T Universal gradient function for temperature

Φ_U Universal gradient function for wind speed

Φ_q Universal gradient function for moisture

ψ_T Stability function for temperature

ψ_U Stability function for wind speed

ψ_q Stability function for specific humidity

1 Introduction and Background

1.1 Motivation

Air-sea interactions and boundary layer turbulence cause the region just above the sea surface, in the lowest portion of the marine atmospheric surface layer (MASL), to be extremely complex and present a number of challenges for direct measurement of this region. This region is characterized by having large exchanges of momentum, heat, and water vapor with varying spatiotemporal scales. The presence of a non-stationary, moving surface – i.e., ocean surface waves – further complicates this region modifying both the transfer of heat and the mechanical mixing through a variety of processes including effects of sea-spray and skin sea-surface temperature inhomogeneities. Currently, it is not well understood how heat and water vapor distributions are impacted by ocean surface waves. This lack of understanding is a consequence of the fully coupled nature of the ocean with the atmosphere.

Within the MASL, temperature, humidity, and wind vertical distributions are commonly modeled utilizing Monin Obukhov (MO) similarity theory or similar bulk parameterizations despite documented shortcomings. Two major shortcomings of this theory have been reported: (i) validity of assumptions regarding constant heat and water

vapor fluxes (Mueller and Veron, 2014) and (ii) neglect of effects due to the ocean free surface (non-stationary surface; Rutgersson et al., 2001; McKenna and McGillis, 2004). In fact, MO derived profiles have been shown to be inaccurate for altitudes below ~3 significant wave heights (H_s) and as high as 10% of the (50-100m) surface layer (Bourassa et al., 1999).

One of the issues that continues to limit further development of empirical and theoretical relationships addressing these knowledge gaps is a lack of *in-situ* near-surface data. Most previous measurements of temperature and moisture over the marine surface are performed using radiosondes, fixed weather stations, or tethered balloon profiling systems (e.g., Marine Atmospheric Profiling System (MAPS) used during the Coupled Air Sea Processes and Electromagnetic Ducting Research (CASPER) East; Wang et al., 2018). These measurement systems are not able to perform wave-coherent measurements in the near surface region. For example, these systems can have bulky sensor housings, and utilize profiling techniques that cannot measure instantaneous profiles (O(1s)).

Very limited wave-coherent measurements of near-surface humidity and temperature have been made to provide insight into heat and moisture exchanges near the air-sea interface. Fine resolution scalar profile measurements over the marine surface continue to be rare where existing profile measurements are limited in number of levels observed (Ortiz-Suslow, 2021). Most previous studies obtain less than four vertical measurement levels to construct vertical profiles (Fang et al., 2018; Li et al., 2018; Katz and Zhou, 2017; Shabani et al., 2014; and Zhao et al., 2015). Consequently, there is a need for development of a

wave-coherent surface measurement platform that is suited to perform measurements across a wide range of wind and wave conditions (Cronin et al., 2019).

Prediction of radar system performance is influenced by the surface and these meteorological properties in the near surface wave-influenced regions of the surface layer. Radar systems transmit electromagnetic (EM) waves in the radio frequency (RF) band in order to sense range, altitude, direction, and/or speed of a target. Radar wave propagation is affected when it encounters different surface geometries (e.g., wind waves), which can scatter the signals leading to complex and unpredictable effects on propagation (Craig and Levy, 1991). Multipath is an example of a surface interaction effect, which occurs when EM waves interfere when reaching a target/are received via direct and indirect (includes a surface bounce) pathways. Consequently, modulation of the EM waves occurs creating instances of constructive and destructive interference. Sirkova (2012) and Lentini and Hackett (2015) found that waves (i.e., sea state) through their interactions with refractivity can influence propagation nearly as much as atmospheric conditions alone.

Changes in atmospheric fluxes of moisture and heat directly alter atmospheric refractivity (Bean and Dutton, 1968). In a vacuum, EM waves will travel in a straight line; however, this is not the case through the atmosphere which has spatial and temporal variations of humidity, temperature, and pressure. As a consequence of these variations, the propagation paths of EM waves are bent. In the near-surface region, this refraction of EM waves can have a significant effect on propagation, and the distribution of refractivity in this region is greatly impacted by turbulent processes. These processes, which are affected by waves,

lead to a highly dynamic environment that is directly responsible for both the attenuation and enhancement of EM wave propagation power.

One extreme impact of refraction is "trapping" which occurs when steep vertical gradients of humidity are present. This process refracts EM waves toward the surface, which are then bounced off the surface and then refracted back towards the surface again causing EM waves to travel within a layer close to Earth's surface – called a trapping layer. These trapping layers can cause anomalously high EM energy to propagate beyond the radar horizon/line of sight (Cherrett, 2015). Ducting can have profound impacts on communications and target detection ranges. When ducting conditions are within 1 m of the ocean surface, which can be below the wave boundary layer (WBL) height, radar performance can be significantly diminished (Paulus, 1990; Babin and Dockery, 2002).

Evaporation ducts (ED) are a type of surface duct most commonly present in the marine environment (Babin et al., 1997). The top of the trapping layer is set by the duct height which is the location where the vertical gradient of modified refractivity is zero. EDs are commonly characterized using modified atmospheric refractivity (M) because it accounts for the curvature of earth such that negative gradients of M with height indicate a duct:

$$M = \left(77.6\frac{P}{T} + 373{,}256\frac{e_p}{T^2} + \frac{z}{R_e}\right) \times 10^6 \tag{1}$$

where P (mb) is pressure, T is temperature (K), e_p (mb) is partial vapor pressure, z (m) is altitude, and R_e (m) is the radius of earth. Thus, the role of waves in altering modified

refractivity near the surface and its associated impacts on EM propagation predictions is central to this research.

Modified refractivity vertical distributions are currently estimated using various methods (Pastore et al., 2021). Bulk algorithms, such as the Coupled Ocean Atmosphere Response algorithm (COARE; Fairall et al., 1996 and Fairrall et al., 2003) and the Navy's Atmospheric Vertical Surface Layer Model (NAVSLaM; Fredrickson, 2015), are commonly employed due to their simplicity. These methods utilize measurements of mean temperature, humidity, and wind speed at the surface and at a reference height to estimate scalar vertical profiles based on MO similarity theory, which are subsequently used to estimate modified refractivity. Alternatively, numerical weather prediction (NWP) models can be used, but they require specialized knowledge and complex data assimilation schemes to obtain the scalar profiles to estimate modified refractivity, and ultimately, have to be merged with aforementioned bulk surface layer models to obtain sufficient vertical resolution in the surface layer. But NWP does have the advantage of not requiring any measurements other than those routinely used for data assimilation. Another approach involves direct measurements such as those performed with tethered balloon ascents/descents of a radiosonde (Anderson et al., 2004; Kang and Wang, 2016; and Wang et al., 2018). However, this particular method has limitations due to poor temporal and horizontal spatial resolution, and lack of truly instantaneous vertical profile measurements. Furthermore, data often have to be extrapolated to the surface – which may not accurately represent the "true nature" of the environment in that region.

Regardless of the shortcomings of these refractivity estimation methods, propagation loss simulations must simulate EM wave propagation up-to the surface and capture its interactions with the surface as accurately as possible. Often times, propagation simulations must simulate refractivity and sea surfaces in inaccurate ways due to incomplete information. How a rough ocean surface interacts with an evaporation duct is often modeled based-on little to no information. For example, how to model the refractivity in the region between a crest and trough in a phase-resolved sea surface using a measured or simulated mean refractive profile referenced to mean sea level is an open question.

This research aims to provide insights into refractivity in the near-surface region over rough ocean surfaces. Despite its well-documented limitations regarding its application over wavy ocean surfaces, the COARE algorithm scalar profiles are still widely used for estimating modified refractivity vertical profiles. Therefore, the COARE algorithm is used as a benchmark comparison for measured refractivity and associated propagation predictions. Furthermore, ocean wave phase-averaged vertical refractivity profiles are compared with ensemble profiles to determine how they deviate from the mean and whether those deviations significantly impact propagation predictions. To provide a broader context of the implications, the analysis is carried out for two radar frequencies to examine differences in trends with radar frequency.

1.2 Background

This section explores the processes that influence the near surface region and consequently temperature and humidity. Figure 1 is a generalized schematic of various processes, which occur near the ocean-surface. Buoyancy and shear are the dominant driving factors for turbulent processes.

1.2.1 Near Surface Processes

Buoyancy effects are caused by uneven heating and moisture in the air, which affects atmospheric density and stability. The atmosphere is considered stable when temperature increases with height, neutral when temperature is the same as the dry adiabatic rate, and unstable when cold air is above warm air. The exchange of energy near the air-sea interface is driven by temperature and humidity gradients (Bradley et al., 1991). In open ocean conditions, unstable conditions are common where colder air sits over warmer ocean water.

The thermal structure of the oceanic surface layer is a direct consequence of the variability of various heat mechanisms – long and short-wave radiation, latent and sensible heat, and evaporation. Ohlmann and Siegel (2000) identified primary controls on the radiative heating of the surface waters of the ocean: i) solar zenith angle under clear skies and ii) cloud index (cloud cover) during cloudy periods. Ultimately, the amount of long-wave radiation emitted back at the surface drives the heat exchange between the ocean and atmosphere (Saunders, 1967). In the absence of short-wave radiation, there would be a net

heat loss at the air-sea interface due to evaporation, sensible heat, and long-wave radiation heat loss (Hasse, 1971).

These controls aid in creating distinct sublayers in the ocean surface layer. Although small, the cool-skin layer (thermal sublayer) plays a significant role in modulating air-sea heat flux differences. Temperature fluctuations in the skin-layer can be > 0.5 °C, extend to depths of a few centimeters (Soloviev and Schlüssel, 1996), and differ from the surface layer bulk temperature by 0.3 °C (Woodcock, 1941). The temperature difference from skin to bulk under light wind conditions can be as high as 1 °C (Saunders, 1967).

Variations of solar transmission are important under light wind conditions (Fairall et al., 1996). The ocean is responsible for "giving" heat to the atmosphere and modifying the boundary layer (Sui et al., 1997). Consequently, a temperature gradient between the sea and air exists, providing a measure of potential energy exchange up to a few meters (Hasse, 1971). These gradients can be large under calm conditions (Sui et al., 1997). Under a warm ocean surface layer temperature, the air temperature increases as the surface is approached, or $\frac{\partial T}{\partial z} < 0$.

Over the open ocean, conditions do exist where the surface is considered smooth. This "smooth" oceanic surface will still have a wind-stress forcing the surface and can appear to have slight chop. The minor surface disturbance (roughness) will modulate both the temperature and water vapor profiles, changing both the gradients and respective fluxes (Mueller and Veron, 2010). A smooth surface no longer persists when wind speeds exceed

3 m s^{-1} (Godfrey and Beljaars, 1991). Under light wind conditions (U < 0.5 m s^{-1} – 1 m s^{-1}) and at "zero" wind speed, random near surface winds termed "gusts" are generated and have been linked to convective overturning within the atmospheric boundary layer (Businger, 1973 and Godfrey and Beljaars, 1991). This "gustiness" depends on the intensity of the convection and can be quite large. When convection is active this causes an increase in the latent heat flux and ultimately a substantial net heat loss (Bhat, 2003). This overturning arises as a result of density differences and causes mixing which ultimately generates a quick and sudden wind. Within the atmospheric boundary layer turbulent fluxes dominate (Zhuang et al., 2018).

1.2.2 Wave Influences on Near Surface Processes

The ocean surface is comprised of many wind-generated waves, which create a wave field. These waves vary on time scales from seconds (i.e., high frequency waves; capillary) to tens of seconds (low frequency waves; swell) and on length scales from centimeters (capillary) to hundreds of meters (swell). Because of rapidly changing conditions, and the coupled nature of the ocean surface with the atmosphere, it is difficult to describe the ocean surface (Pierson and Moskowitz, 1964). Frequently, in any one location, a combination of capillary, wind, and swell waves will co-exist to comprise this wave field. These wave fields are pseudo-random, propagate rapidly, break intermittently, and aid in forcing winds in the atmosphere (Sullivan and McWilliams, 2010).

Not only does wind play a substantial role in generating waves, it also has a profound effect on altering the heat and moisture content above the air-sea interface. On the aqueous side, it alters the thermal structures that are generated in the absence of waves (§1.2.1), such as increasing and decreasing the skin-layer temperature. On the air side, the development of the waves causes a boundary-layer to form which creates unique velocity profiles on the crest and the trough of a wave. A wave boundary-layer (WBL) is defined as the part of the atmospheric surface layer that is directly influenced by waves. Under growing seas, the wave boundary layer thickness is ~ 1 m (Janssen, 2004) and substantially larger for swell. The momentum transfer above a wave is a consequence of the non-uniform momentum flux with height (Garbe et al., 2013). The surface stress is dependent on wave characteristics (Garbe et al., 2013). The dominate momentum transfer processes within the WBL are viscosity and pressure perturbations, which show wind speed dependence, whereas heat transfer is a result of diffusivity (Garbe et al., 2013). This WBL is responsible for turbulent dispersion of water droplets above the air-sea interface (Fairall and Edson, 1994).

In the presence of waves, the cool-skin layer is impacted. Under low to moderate wind speeds, capillary waves play an important role. As a result of a surface water divergence, a large strain-rate, caused by high vorticity pockets (Okuda, 1982), is produced leading to substantial increases, and decreases in skin-layer temperature. At low wind speeds (U< 4 m s^{-1}), Veron et al. (2011) found that surface renewal theory was insufficient at explaining the temperature time decay, which is a function of wind speed. They attributed this departure to be a consequence of free convection being the dominate mechanism (Soloviev

and Schlüssel, 1994 and Wick,1995) suggesting that shear production is not the only contributor to this phenomenon (Veron et al., 2011).

When locally generated wind waves are present, the surface temperature is largest near the wave crest (Witting, 1971; 1972). At low wind speeds, the temperature maximum is located downwind (downslope phase) of the wave crest (Veron et al., 2008). When wind speed increases and or is above 1- 2 m s^{-1} this maximum temperature shifts upwind of the wave crest (Miller and Street, 1978; Veron et al., 2008). In addition, Schooley (1975) found that the maximum air-temperature occurs within the trough region and substantial drops in temperature occur at the wave crest. Hence, the strength of wind plays a role in shifting the location of maximum skin temperature over one wavelength.

DeCosmo et al. (1996) during their field campaign found for altitudes 6m-8m above mean sea-level (MSL) that water vapor flux was wave age dependent. Latent heat flux was found to dominate the heat budget. However, they indicated that it would be incorrect to draw conclusions for turbulent fluxes in the near surface region from higher altitudes. Yang and Shen (2017) found complimentary evidence that scalar transport had wave age dependency above a wave. Air moisture content (i.e., humidity) above the air-sea interface is a linear function between the surface and $\sim 0.35 H_s$ and decreases ~40% over this range (Schooley, 1975). For young wave ages, a region of large temperature fluctuations is located above the trough, and for developing and near-fully developed waves, this region is located above the windward wave crest face (Yang and Shen, 2017). The results of both Schooley (1975)

and Yang and Shen (2017) suggest that wave influences on thermodynamic properties are contained within a region very close to the interface.

Sea-spray inherently alters thermodynamic distributions and is a large source for moisture in the air. The vertical extent and concentration of spray droplets is a result of the redistribution of the droplets by the turbulent flow field augmented by the presence of waves (Belcher and Hunt, 1998; Sullivan and McWilliams, 2002). As a result of various droplet types, the near-surface atmosphere is moistened and cooled because of the evaporation of some of these droplets (DeCosmo et al., 1996). Depending upon the air-sea temperature difference, the exchange of sensible heat can either warm or cool the surrounding air (Hasse, 1963). The reduction of sensible heat flux with an increase in altitude (DeCosmo et al., 1996) is directly related to the droplet concentration, size, and vertical extent. The alteration of heat and moisture content in the MASL is a result of spray/droplet residence times.

Another potential mechanism for observed humidity and temperature distributions is a result of the air flow separation process above a wave crest. This process is common over young developing seas (Buckley and Veron, 2019). Air flow separation is highly unsteady, rapid, and persists for a short period of time (Reul et al., 1999; Reul et al., 2008). When wind and wave speed increase, air-flow separation is more common (Tian and Choi, 2013); however, under low wind speed conditions or low wave steepness (S), air flow separation may not occur (Tian and Choi, 2013). Donelan et al. (2006) obtained supporting evidence for flow-separation without breaking. In contrast, Banner and Melville (1976) and Kharif

et al. (2008) found that air-flow separation typically only occurred during breaking events. Nonetheless, air flow separation or lack thereof plays an important role in scalar field redistribution.

Various turbulence parameters have been found to be phase dependent. A laboratory study by Buckley and Veron (2019) found that normalized Reynolds stress ($\frac{\overline{u'w'}}{u_*^2}$; u_* friction velcoity) displays a strong coupling with waves on the leeward side. Sullivan and McWilliams (2010) found that turbulent kinetic energy production exhibits unique structures in the trough region, and Newgard and Hay (2007) found that the highest turbulence intensity occurs above the wave crest. Reul et al. (1999) identified a well-defined recirculating structure (i.e., vortex pocket) up to the wave crest that is sustained as a result of re-entrainment processes. Overall, wave-impacted turbulence quickly blends into the bulk wind over a vertical distance dependent upon wave age (Sullivan et al., 2014). When wave phase speed (c) equals the mean wind speed, a decrease in coherence with the wave is observed and the wave induced wind velocity component nearly vanishes. Under mature seas, the wave induced flux measured 10 m above MSL was upward and had a magnitude that is equivalent to 20% of the total downward momentum flux.

1.2.3 MO Theory

Modeling of near surface temperature and humidity as a function of altitude is typically performed using classic MO similarity theory (1946). The most commonly used empirical coefficients for MO theory are from the Kansas land experiments (Businger et al., 1971).

For obvious reasons, these coefficients have been refined from studies over water (see for example Charnock, 1955; Smith, 1989; and Godfrey and Beljaars, 1991). Bulk inputs used for MO theory are based-on mean atmospheric conditions utilizing 10-minute (Yaglom, 1977) to 1-hour (Huagen et al., 1971 and Fairall et al., 2003) ensemble averages. An overview of averaging windows and experiment types are provided in Table 1. Fundamental to MO theory is the Obukhov length scale (L). It has a dimension of length and indicates the height at which buoyancy driven turbulence is similar in magnitude to that driven by shear:

$$L = \frac{-u_{*0}^{3}}{\left[\kappa(\frac{g}{\theta_v})\overline{w'\theta_v'}\right]} \tag{2}$$

where u_{*0} is the friction velocity at the surface, κ the von Karman constant, g acceleration due to gravity, θ_v mean virtual potential temperature, w' the turbulent vertical wind component, and θ_v' the turbulent virtual potential temperature. L is used to scale height above MSL (z) to yield the dimensionless stability parameter $\zeta = z/L$.

One of the dominant characteristics of the atmospheric boundary layer is vertical turbulent transfer of mass, momentum, and heat. Difficulty lies in quantifying the associated surface fluxes of these parameters, and the height variation of the fluxes through the entire thickness of the surface boundary layer (Garratt, 1992). MO similarity theory has been developed for the atmospheric surface layer, where the nondimensionalized gradient functions of momentum/wind, temperature, and specific humidity (i.e., ratio of mass of water vapor to the total mass), denoted by subscripts U, T, and q, respectively, are (Garratt, 1992):

$$\Phi_U(\zeta) = \left(\frac{\kappa z}{u_{*0}}\right)\frac{\partial \overline{U}}{\partial z} \tag{3}$$

$$\Phi_T(\zeta) = \left(\frac{kz}{\theta_{v_{*0}}}\right)\frac{\partial \overline{\theta_v}}{\partial z} \tag{4}$$

$$\Phi_q(\zeta) = \left(\frac{kz}{q_{*0}}\right)\frac{\partial \overline{q}}{\partial z} \tag{5}$$

where, an overbar indicates an ensemble average, $\theta_{v_{*0}}$ is the surface virtual potential temperature scaling $(\theta_{v*0} = -(\overline{w'\theta_v'})_0/u_{*0})$ and q_{*0} is surface specific humidity scaling $(q_{*0} = -(\overline{w'q'})_0/u_{*0}$. Equations (3)-(5) inherently contain three asymptotic limits of interest: the unstable limit ($\zeta \to -\infty$), stable limit ($\zeta \to \infty$), and neutral limit ($\zeta \to 0$).

Under highly unstable conditions ($\zeta \leq -5$), the system approaches a state of local free-convection (Tennekes and Lumley, 1972), which dominates any shear-driven turbulence. Further, MO similarity theory (Eq. (3)-(5)) fails under these conditions because u_{*0} is no longer a relevant parameter. A state of free-convection occurs when u_{*0} approaches zero, but buoyancy flux $(\overline{w'\theta_v'})$ does not (Fairall et al., 1996). At this limit ($\zeta \to -\infty$), wind shear is negligible, and the only parameter of interest is the θ_v profile. The vertical gradient of mean virtual potential temperature for free-convective conditions scales as:

$$\frac{\partial \overline{\theta_v}}{\partial z} = -\alpha_1(\overline{w'\theta_v'})_0^{\frac{2}{3}}\left(\frac{g}{\theta_v}\right)^{-\frac{1}{3}}z^{-\frac{4}{3}} \tag{6}$$

where α_1 is a positive constant, ~0.7 (Garratt, 1992). MO scaling can be replaced with free-convective scaling for the highly unstable scenario (Wyngaard et al., 1971). These scaling parameters for velocity (u_f) and temperature (θ_f) are, respectively (Garratt, 1992):

$$u_f = \left[z \left(\frac{g}{\theta_v} \right) \overline{(w'\theta_v')}_0 \right]^{\frac{1}{3}} \tag{7}$$

$$\theta_f = \left[\frac{\overline{(w'\theta_v')}_0{}^2}{z \left(\frac{g}{\theta_v} \right)} \right]^{\frac{1}{3}} \tag{8}$$

Under slightly unstable, stable, and neutral conditions, simple integration of Equations (3), (4), and (5) yields logarithmic profiles:

$$\frac{\kappa \overline{U}}{u_{*0}} = ln \left(\frac{z}{z_0} \right) - \psi_U(\zeta) \tag{9}$$

$$\frac{\kappa (\overline{\theta_v} - \theta_0)}{\theta_{v*0}} = ln \left(\frac{z}{z_T} \right) - \psi_H(\zeta) \tag{10}$$

$$\frac{\kappa (\bar{q} - q_0)}{q_{*0}} = ln \left(\frac{z}{z_q} \right) - \psi_W(\zeta) \tag{11}$$

where z_0 is aerodynamic surface roughness, z_q is the scalar roughness length for humidity, and z_T is the scalar roughness length for temperature (discussed at the end of this sub-section). $\psi_U(\zeta), \psi_W(\zeta)$, and $\psi_H(\zeta)$ are stability functions for wind, humidity, and temperature, respectively, and are the integral of the universal gradient functions ($\Phi_U, \Phi_H,$ and Φ_W). The effects of buoyancy in this form can be interpreted as a deviation from the neutral case. Observational studies of the surface layer, primarily over land, have yielded empirical forms of Φ_U, Φ_H, and Φ_W(Garratt, 1992). Φ_H has been based on observations of potential temperature profiles, and it is common to assume that $\Phi_H = \Phi_W$.

For the unstable case, $-5 < \zeta < 0$, these empirical functions are $\Phi_U(\zeta) = (1 - \gamma_1\zeta)^{-1/4}$ and $\Phi_H(\zeta) = \Phi_W(\zeta) = (1 - \gamma_2\zeta)^{-1/2}$. For the stable case $(0 < \zeta < 1)$, $\Phi_H(\zeta) = \Phi_W(\zeta) = \Phi_U(\zeta) = 1 + \beta_1\zeta$. Although values can vary slightly, typically $\gamma_1 \approx \gamma_2 \approx 16$ and $\beta_1 \approx 5$. With these functions, $\psi_U(\zeta)$, $\psi_H(\zeta)$, and $\psi_W(\zeta)$ can be estimated.

Using the $\Phi_U(\zeta)$ and $\Phi_H(\zeta) = \Phi_W(\zeta)$ for $-5 < \zeta < 0$ (unstable case), integration of Equations (3-5) results in:

$$\psi_U(\zeta) = 2ln\left[\frac{1+x}{2}\right] + ln\left[\frac{1+x^2}{2}\right] - 2\tan^{-1}x + \frac{\pi}{2} \qquad (12)$$

$$\psi_H(\zeta) = \psi_W(\zeta) = 2\ln\left[\frac{1+y}{2}\right] \qquad (13)$$

where $x = (1 - \gamma_1\zeta)^{1/4}$ and $y = (1 - \gamma_2\zeta)^{1/2}$. Values of γ_1 (empirical coefficient) range between 16 and 28 and γ_2 (empirical coefficient) range between 9 and 14 (Dyer and Hicks, 1970; Businger et al. 1971; Wieringa, 1980; Dyer and Bradley, 1982; Webb, 1982; and Hogstrom, 1988; Dyer, 1974). Dyer (1974; review) found that the appropriate values were $\gamma_1 = \gamma_2 = 16$. The profile stability function for the unstable case has only been validated for $-2 < \zeta < 0$ because reliable measurements only exist for $\zeta > -2$. At $\zeta \leq -5$, the only profile of concern is the temperature profile (θ_v) and its stability function is:

$$\psi_c = 1.5ln\left[\frac{r^2 + y + 1}{3}\right] - \sqrt{3}\,\tan^{-1}\left[\frac{2r+1}{\sqrt{3}}\right] + \frac{\pi}{\sqrt{3}} \qquad (14)$$

where $r = \sqrt[3]{1 - \gamma_1\zeta}$. An example momentum (A), temperature (B), and humidity (C) profile for an unstable regime based-on MO theory is presented in Figure 2.

For the stable case, $0<\zeta<1$, the empirical functions are $\Phi_H(\zeta) = \Phi_W(\zeta) = \Phi_U(\zeta) = 1+\beta_1\zeta$, which after integration yields the stability functions:

$$\psi_H(\zeta) = \psi_W(\zeta) = \psi_U(\zeta) = -\beta_1\zeta \tag{15}$$

β_1 (empirical coefficient) for wind ranges between 4.7 and 6.9 (Garratt, 1992), while β_1 for temperature and humidity profiles range between 4.7 (Businger et al., 1971) and 9.2 (Wieringa, 1980). Dyer (1974; review) suggests $\beta_1= 5$ for all profiles. Under neutral conditions $\zeta = 0$, the profiles revert to the familiar logarithmic shape and the stability function is dropped, i.e., $\psi_H(\zeta) = \psi_W(\zeta) = \psi_U(\zeta) = 0$.

Surface roughness in Equation (9) is characterized through z_0. An increase in wind speed will affect the aerodynamic roughness length. The roughness length was originally investigated by Charnock (1955) and modified by Smith (1989) to include a smoothness term:

$$z_0 = \frac{\alpha_c u_*^2}{g} + \frac{0.11\nu}{u_*} \tag{16}$$

where ν is kinematic viscosity and α_c the Charnock constant. The Charnock constant (α_c) has been found to range from 0.012 (Charnock, 1955) to 0.035 (Kitaigorodskii and Volkov, 1965). Taylor and Yelland (2001) and Oost et al. (2001) estimated z_0 from wave properties. Both equations are relatively similar and include the smoothness term from Smith (1989).

Unlike surface roughness, less consensus can be found for temperature and humidity roughness lengths in Equations (10) – (11). It is, however, common practice within the literature to have $z_T = z_q$ (Beljaars and Holtslag, 1991; Fairall et al., 2003). Fairall et al. (2003) adopted an empirical fit to the Tropical Ocean Global Atmospheres (TOGA) Coupled Ocean Atmosphere Response Experiment (COARE) and the Humidity Exchange Over the Sea (HEXOS) data to obtain estimates of $z_T = z_q$:

$$z_q = \min(1 \times 10^{-4}, 5.5 \times 10^{-5} R_r^{-0.6}) \tag{17}$$

Here R_r is the Reynold's roughness number. Geernaert et al., (1987) set roughness lengths for both humidity and temperature to a constant of 2×10^{-5} m, which implies that humidity and temperature flux do not vary with wind-wave conditions. Within the literature there is general consensus regarding temperature and humidity surface roughness lengths in terms of order-of-magnitude, but slight variations occur via differing empirical coefficients (Kondo, 1975; Brutsaert, 1982; DeCosmo et al. (1996).

Various LES (Sullivan et al., 2014 and Jiang, 2020) studies and a field study (Anderson et al., 2004) investigating MO theory's validity over a wavy surface conclude that scalar profiles deviate from their classically held shape – specifically, profiles were not found to monotonically decrease with height above the sea-surface. Profiles of temperature and humidity over waves were sheared and momentum profiles followed a log-linear profile shape higher in altitude (Sullivan et al., 2014). Jiang (2020) found when wind opposed swell, the boundary layer height was increased. For opposite conditions, scalar profiles show concavity in a shallow layer directly above the surface and a reduction in the moisture

gradient. MO theory is unable to account for these effects (Rutgersson et al., 2001 &

McKenna and McGillis 2004) and begins to be applicable at $3H_S$ up to about 4%-10% of

the surface layer (50-100 meters; Bourassa et al., 1999). Currently, because application of

MO theory near the air-sea interface is questionable, a knowledge gap exists limiting our

ability to model near-surface humidity and temperature profiles.

1.3 Research Overview

The research described herein achieves several objectives. First, the design, development,

and deployment of a novel near-surface wave-coherent instantaneous profiling system

(NWIPS) for *in-situ* atmospheric measurements is described in Chapter 2.[1] The results

from the deployment of NWIPS are discussed in Chapter 3. The high temporal and spatial

resolution measurements acquired with NWIPS are novel and unique. They enable the

examination of vertical distributions of temperature and moisture very near the air-sea

interface. These measurements allow for direct evaluation of wave-coherent vertical

profiles and evaluation of MO theory in this near surface region. Specific research

questions explored in Chapter 3 include:

---

[1] Chapter 2 is based-on the following published paper: **Stanek, M. J.**, Pastore, D. M., and
Hackett, E.E. 2023. A novel near-surface wave-coherent instantaneous profiling system for
atmospheric measurements. *Sensors 23. 4099.*

i. Are MO theory temperature (eq 10) and humidity (eq 11) predictions valid near the surface (i.e., within several significant wave heights above the surface), and to what extent?

ii. How do ensemble humidity and temperature impact refractivity vertical distributions?

iii. Are humidity and temperature vertical profiles wave phase dependent?

iv. On time scales of ~ 20 minutes are wave phase dependent humidity and temperature vertical profiles steady?

As demonstrated in Chapter 3, the high spatial resolution *in-situ* measurements deviate from MO theory temperature and humidity vertical profiles within the lowest 3 m of the MASL. In Chapter 4, the impacts of these discrepancies on propagation loss are discussed. In addition, the NWIPS performance during the field experiment is evaluated and future improvements discussed. The specific research question to be addressed in this chapter is:

v. How do the observed changes in refractivity vertical distributions impact radar wave propagation?

Chapter 5 provides a summary and highlights main conclusions of the research.

Table 1 Review of averaging windows used for parameter estimates in universal gradient functions and related stability functions for temperature and moisture applied in MO theory.

Author	Temporal Averaging Window	Type
Businger et al., 1971	15 minutes	Land
Huagen et al., 1971	1 hour	Land
Hanafusa, 1971	15 minutes	Land
Yaglom, 1977	10 minutes	Review
Grachev and Fairall, 1996	50 minutes	Ocean
Fairall et al., 2003	10 minute – 1 hour	Ocean
Gerbi et al., 2008	20 minutes	Ocean
Ortiz-Suslow et al., 2021	30 minutes	Ocean
Jiang and Wang, 2021	3 minutes – > 30 minutes	Ocean
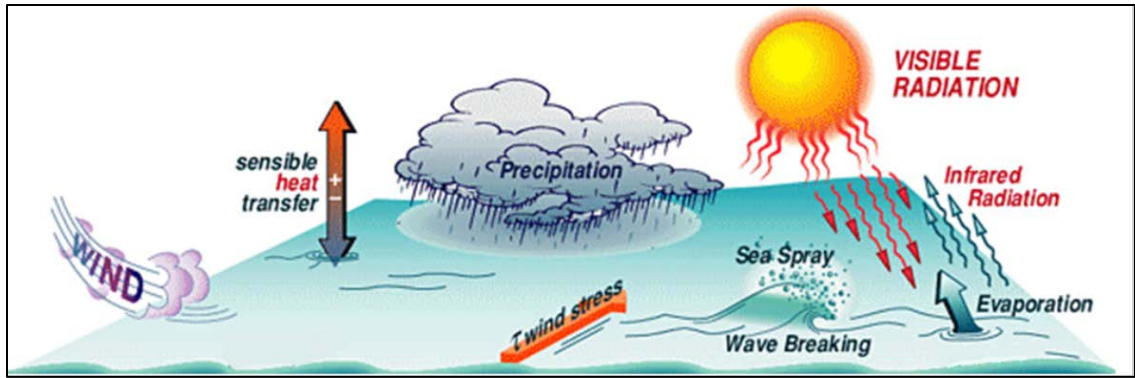
Figure 1 Generalized schematic of processes which occur near the air-sea interface (modified from Weller, R. WHOI, http://uop.whoi.edu).
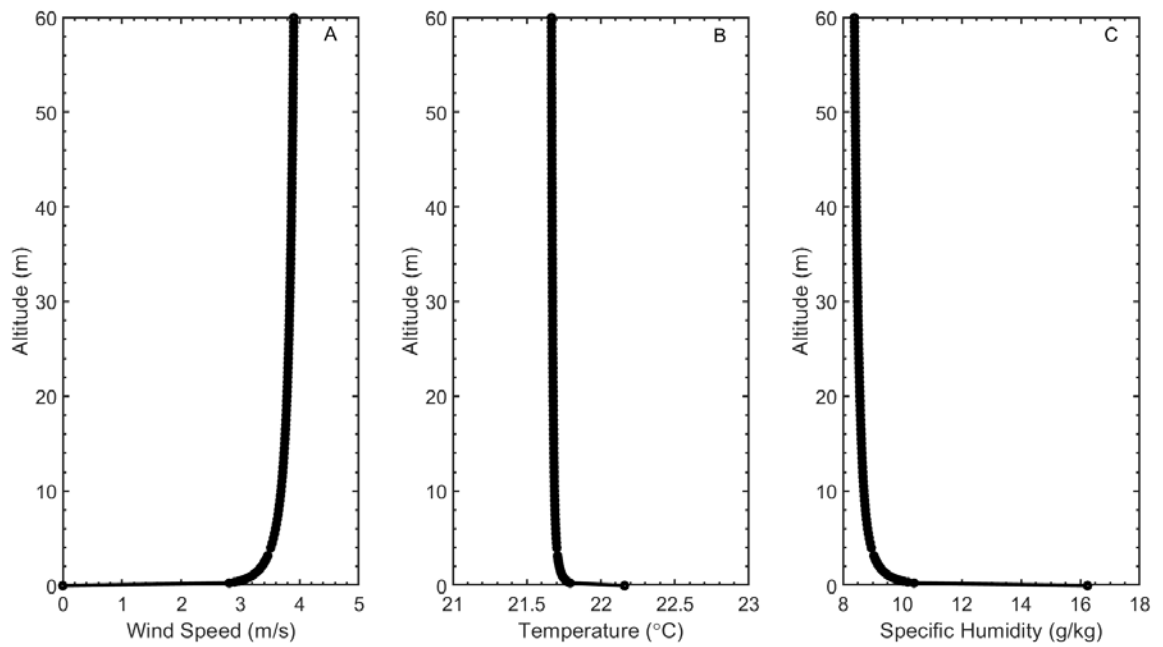
Figure 2 Example unstable regime, wind speed (A), temperature (B), and specific humidity (C) profile generated using COARE 3.0 (Fairall et al., 2003).

2 NWIPS Design, Development, and Deployment

This chapter presents a novel near-surface wave-coherent measurement platform, as well as its deployment in a field experiment during October 2022, that measures with high spatial and temporal resolution temperature and humidity vertical distributions. This chapter begins with the design of NWIPS and corresponding instrumentation, as well as discusses instrumentation onboard the Research Vessel Coastal Explorer (hereinafter R/V CE) from which NWIPS was deployed. Presentation of experimental conditions from the field experiment concludes the chapter.

2.1 Near-surface Wave-coherent Instantaneous Profiling System

The near-surface wave-coherent instantaneous profiling system (NWIPS) is illustrated in Figure 3. This platform is a custom-designed large discus-type buoy based on the National Oceanic and Atmospheric Administration (NOAA) National Data Buoy Center's (NDBC) 3 m discus buoy (Hall et al., 2018). The buoy implements lightweight and cost-effective materials. The platform incorporates a vertical array of small temperature and humidity sensors spanning 0-3 m above the instantaneous sea surface. With measurements approximately every 10 cm over this interval, the vertical resolution is high compared to other buoy (e.g. Fredrickson et al., 2003) and platform studies, such as those which use R/P

FLIP (Ortiz-Suslow, 2021). In addition, NWIPS incorporates a stern mounted tethered weather balloon with miniature radiosonde systems (Windsond), providing four additional upper altitude measurements (Figure 3A).

The hull is constructed of ¾ inch plywood, which is kerf cut to provide a hexadecagon (very close to circular) shape. Three layers of 1.5 oz fiberglass are used to fortify the wooden structure and ensure a robust watertight hull. The buoy has a hull diameter of 2.4 m, a depth of 0.75 m, and a draft of ~0.10 m (481 kg) where the overall design provides a 0.65 m freeboard depth. The center of mass is 0.63 m on center above the bottom of the buoy and the center of buoyancy lies at the geometric center of the displaced amount of water which is ~.05 m above the buoy bottom.

The NWIPS's mast is constructed from polyvinyl chloride (PVC) extending from below the buoy deck (i.e., from within the hull) to ~ 3 m above the buoy deck. PVC is utilized as mast material because it is white as well as being light weight and rigid. White is chosen as the primary color of the buoy platform and mast to minimize surface heating of the structure caused by shortwave radiation. The mast is constructed in a triangular truss to promote stability where measurement arms protrude from the forward mast and extend outward radially from the buoy. The overall length of a measurement arm is 0.63 m where ~0.12 m extends over the water surface. The lowest measurement position is 0.27 m above the instantaneous water level with a sensor every 0.10 m above this point up to 3.0 m altitude. This sampling interval provides for a spatial resolution of 0.2 m. The lowest four measurement arms protrude out from the buoy hull to obtain measurements as close to the

sea surface as possible (Figure 3B – see inset). Each measurement arm houses an SHT-85 sensor, which measures temperature and humidity. This sensor has previously been used as a calibration sensor on unmanned aircraft systems (Boer et al., 2022). Side-by-side comparisons of this sensor with a MaxiMet weather station show similar performance under a range of field and lab conditions (Stanek and Hackett, 2021; Stanek et al., 2021). Above the mast, a weather balloon is attached with Windsond measurements nominally located at 7 m, 10 m, 12 m, and 15 m above mean water level (MWL). However, the Windsond altitudes vary (at or below the nominal altitude) as a result of the movement of the balloon caused by the wind (Figure 3A); thus, their exact altitude for each temperature/humidity measurement is measured via pressure by the Windsond. Below the mast and buoy hull, a HOBO U20 water level data logger is used to obtain bulk sea-surface temperatures and absolute pressure, and is mounted at a depth of ~0.27 m below instantaneous water level immediately below and forward of the buoy hull.

To ensure thermodynamic variable measurements are not disturbed by the platform wake, two windsocks are positioned atop each of the stern vertical masts self-orienting the buoy and measurement mast into the wind. This positioning minimizes mast structure interference on measurements and further aid in reducing both thermal and flow distortions (e.g., Mitsuta and Fujitani, 1974 and Bradley et al., 1991). Buoy orientation is determined via 3DM-GX5-25 micro-strain attitude heading reference system (AHRS; Lord Parker), mounted within the buoy hull.

NWIPS SHT-85 sensor integration is accomplished through the implementation of a series of watertight electronics boxes housed interior of the hull. Each box contains an Arduino Uno microcontroller, datalogging shield with real-time clock, and an inter integrated circuit (I^2C) multiplexer (TCA9548A by Adafruit). The I^2C multiplexer allows multiple SHT-85 sensors, which have the same serial address, to operate simultaneously. Prior to deployment, all electronics boxes are initialized and validated for correct time stamps. The AHRS system is controlled using a small Raspberry Pi which handles sensor initialization and data-logging. Lastly, the HOBO U20 and Sparv Embedded windsonds operate on self-contained and telemetry packages, respectively. Atmospheric sensor specifications are presented in Table 2 below.

The R/V CE was used for launch and recovery of NWIPS. In addition, it was outfitted with a Vaisala WXT536 weather station and a Kipp Zonan SMP3 pyranometer (radiation) providing bulk atmospheric measurements. Both instruments are mounted on a beam off the starboard gunnel at a sweep angle of ~20° from along axis of the vessel (the angle is to prevent interactions with the dive platform on the CE). The pyranometer was mounted 2 m away from the gunnel at a height of ~2.07 m above MSL. Spaced 0.85 m aftward from the pyranometer, is the Vaisala WXT536 weather station, which is ~2.37 m above MSL. Sensor specifications onboard the R/V CE are found in Table 2 and setup schematic in Figure 4. The bulk meteorological measurements from the R/V CE are used as inputs into the COARE 3.0 bulk prediction model. During experiments the R/V CE was generally orientated in an easterly position providing for maximum vessel stability and undisturbed flow at the weather station.

2.2 Field Experiment

The NWIPS meteorological sensors were tested extensively in the lab and field (over land and enclosed water bodies) and compared with measurements from a weather station (Stanek and Hackett, 2021), and the NWIPS system as a whole, was deployed in two test events prior to the deployment collecting the measurements described in this dissertation. The sensor testing verified that the SHT-85 sensors were sufficient in accuracy for these field measurements, and the prior field tests of NWIPS enabled development of deployment procedures resulting in collection of a continuous high-resolution dataset with sufficient environmental context. The field experiment and these test events collectively enabled the following objectives: (i) to test the NWIPS including its various components (e.g., temperature and humidity sensors) and (ii) assess the performance of NWIPS wave-coherent measurements. Objective (i) corresponds directly to the accuracy and longevity of the SHT-85 sensors onboard the platform, especially at the lowest measurement positions, and how quickly sensor accuracy deteriorates or ceases operating due to salt fouling (DeCosmo et al., 1996). Furthermore, we sought to understand platform contamination including efficacy of the windsock-based orientation system. Between each test event, and the field experiment, several modifications were performed including but not limited to – radiation shields, redundant sensors, additional upper altitude measurements, and new electronics integration.

The NWIPS field experiment, which represent the data presented in this dissertation, took place 6 - 8 km offshore Little River, SC in October 2022. Measurements were performed

over ~2 hours. However, due to technical issues with onboard R/V CE vessel positioning data only 80 minutes of NWIPS data are used. Position and heading data are required to correct wind speed (and direction) measured by a Vaisala WXT536 onboard the R/V CE, and wind speed is needed for bulk to skin sea-surface temperature corrections. Thus, a complete vertical temperature profile is only possible when these corrections can be made. Additionally, two of the Windsonds failed due to issues with the telemetry system, so only two upper altitude measurements from the weather balloon are used in this dissertation (those at nominally 7 m and 15 m). During the experiment, the buoy remained within 30 m -160 m of the research vessel.

Supplementary meteorological measurements were obtained from a shipboard-mounted Vaisala WXT536 weather station. During the experiment, these meteorological measurements did not vary extensively. Atmospheric stability $\left(\frac{z}{L}\right)$ is estimated to be in the unstable regime ($-0.72 < \frac{z}{L} < -0.27$), where $z= 2.37$ m (the altitude of measurements) and the Coupled Ocean Atmospheric Response Experiment (COARE; Fairall et al., 1996; Fairall et al., 2003) bulk algorithm is used to estimate the Obukhov length (*L*). The general wind direction for the duration of the experiment was North to Northwest. Air temperature varied between 17 °C - 19 °C and water temperature was relatively constant at ~22 °C. Wind speed was observed to be between 1 ms^{-1} and 6 ms^{-1} and relative humidity between ~50% and ~65%. Relative humidity is the ratio of the vapor pressure to the saturation vapor pressure (for that air temperature). A time series of the prevailing environmental conditions is provided in Figure 5.

Comparison time series of temperature and relative humidity between NWIPS and measurements performed aboard the R/V CE by the Vaisala weather station are shown in Figure 6. Measurements in Figure 6 are for similar altitudes above the instantaneous sea surface (~2.37 m) for both the weather station and NWIPS. For the duration of the experiment, trends over time of measurements from both platforms are in relatively good agreement despite an apparent bias for temperature. Differences between air temperature measurements are within 2.5°C with a root mean square error (RMSE) of 2.31 °C and average difference of -2.28 °C. This bias is an order of magnitude larger than that observed under a range of wind speeds (0 ms^{-1} – 10 ms^{-1}) inside a small wind tunnel in controlled laboratory conditions. However, when the sensors were in close proximity during deployment preparation on-station, a bias (average difference) of -1.5 °C was observed – at least partly explaining the bias observed in Figure 6. Because the bias was not observed during wind tunnel testing, we conclude that the observed bias is likely related to differences in radiation – both how it is mitigated by each sensor and or differences in incoming radiation due to sensor positioning.

There are several possible sources of uncertainty stemming from discrepancies in the radiation itself or how it is mitigated. First, the type of radiation shield used by the weather station differs from that used on the SHT-85 sensors (i.e., stacked plate vs. slit-style). Second, the R/V CE must be aligned with the waves for stability purposes while drifting, which on this particular day, caused the weather station to be located in the shade of the ship's superstructure. Perhaps the difference in the radiation between the two locations was

significant enough to contribute to this temperature discrepancy. Lastly, naturally ventilated weather stations under full sunlight and $U < \sim 4$ ms^{-1} can lead to inaccuracies of $> \pm 1$ °C (Tanner, 1990). Furthermore, stacked plate radiation shields (utilized by the Vaisala weather station) can have errors between ± 3 °C to ± 1 °C for winds ranging from 0.5 ms^{-1} to 5 ms^{-1}, respectively (Gill, 1983). Measured wind speeds during the field experiment were < 5 ms^{-1} 97% of the time; thus, ventilation issues could also be contributing to the discrepancy. Finally, it should be noted that a portion of the difference could also be associated with spatial inhomogeneity.

Relative humidity, which has the greatest measurement uncertainty, has a 5.4% RMSE and an average difference of 4.26%, which is slightly higher than the cumulative error from both sources (i.e., Vaisala WXT536 relative humidity error is $\pm 3\%$ and the SHT85 is $\pm 1.5\%$). In addition, like the temperature, these slight humidity variations between the R/V CE and NWIPS may also be at least partly a result of inhomogeneity. Time series of atmospheric sensors (mast-mounted SHT-85 and Windsond) onboard NWIPS is presented in Figure 7.

Sea surface spectra measured during the experiment exhibited a single peak in the wind-wave frequency range. The peak wind-sea period and significant wave height were 2.5 s and 0.18 m, respectively. Sea-state spectrum indicate a pure wind-sea and thus wind and wave direction are aligned. A qualitative assessment, via video recording, of white capping conditions indicates that whitecap coverage was <5% in the vicinity of the experiment, consistent with observed coverage in similar wind speeds (Brumer et al., 2017).

Table 2 Manufacturer accuracy for sensors.

	Sensirion SHT-85	Sparv Embedded Windsond (S1H3)	Vaisala WXT536
Temperature	± 0.1 ℃ τ = 5 s	± 0.2 ℃ τ = 6 s	± 0.3℃ τ = not provided
Relative Humidity	± 1.5 % RH τ = 8 s	± 1.8% τ = 6 s	± 3% at 0% - 90% RH ± 5% at 90% -100% RH τ = not provided
Pressure	X	±1 mb	±1mb
Wind Speed	X	X	±3% at 10 m/s τ = 0.25 s
Wind Direction	X	X	± 3.0° at 10 m/s
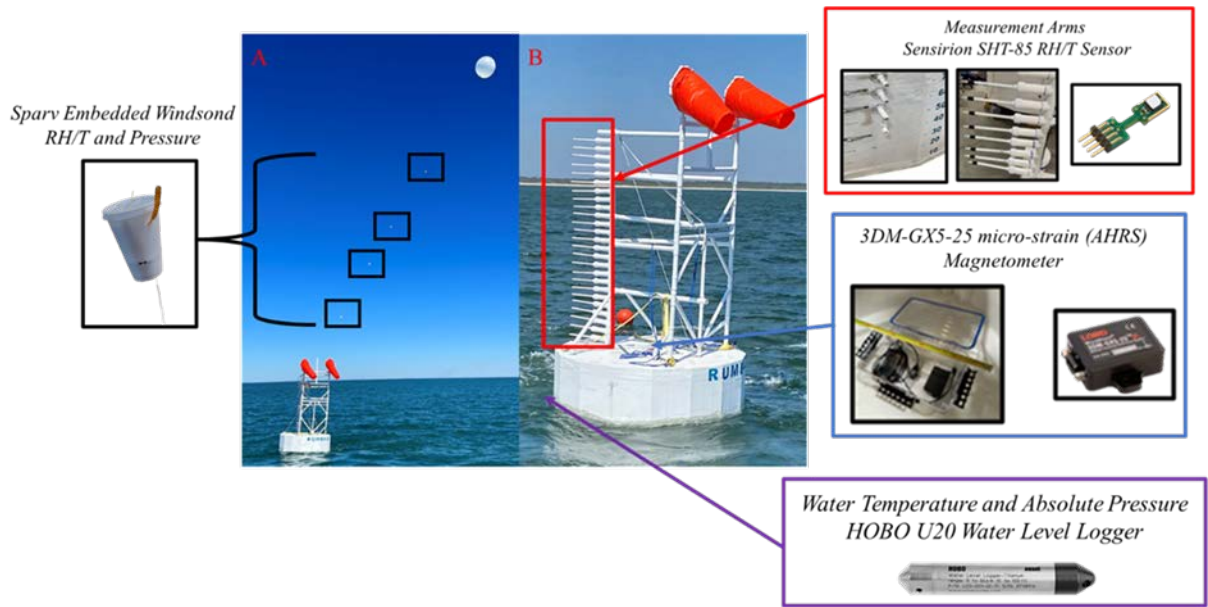
Figure 3 Image of the NWIPS associated sensors. Panel (A) shows NWIPS deployed, and Panel (B) is a zoom-in of the buoy and mast from Panel (A).
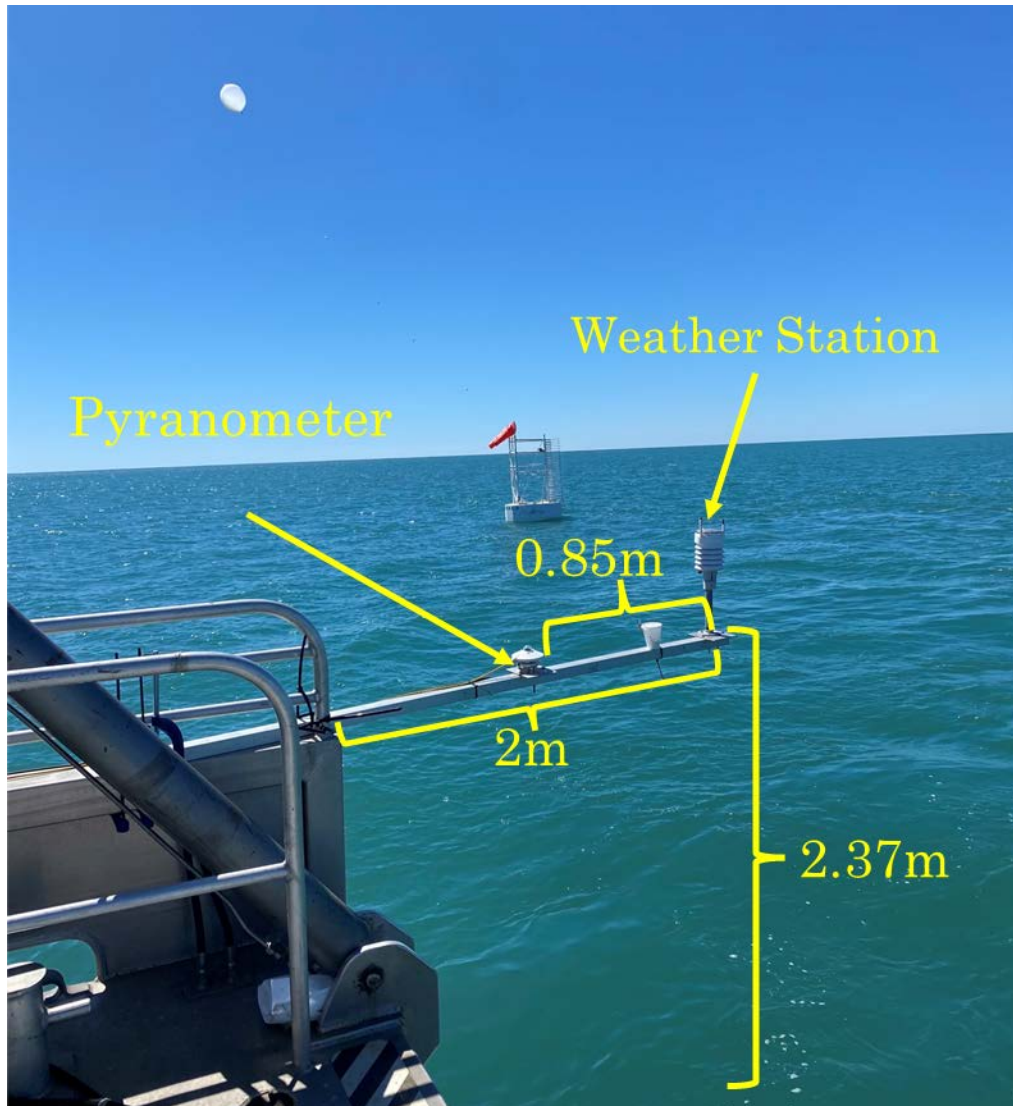
Figure 4 Image of CE instrumentation and respective locations.
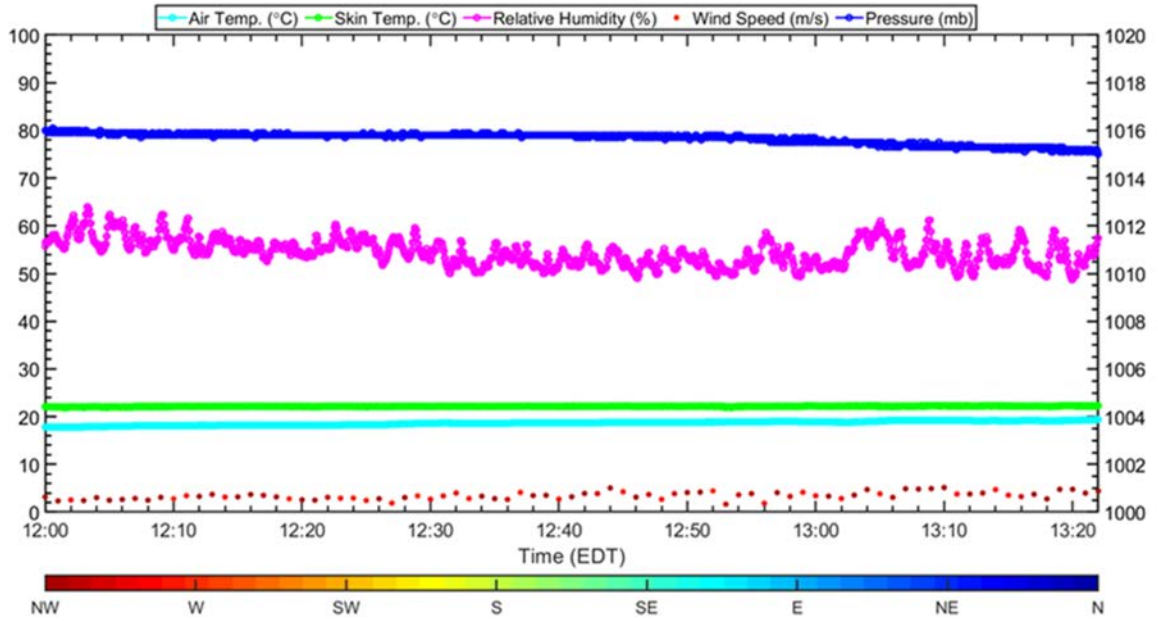
Figure 5 Time series of prevailing environmental conditions. The left y-axis shows air temperature (℃), sea-surface skin temperature (℃), relative humidity(%), and wind speed (m s⁻¹). Wind direction is denoted by the colorbar and reflected by the color of the wind speed markers. The right y-axis is pressure (mb).
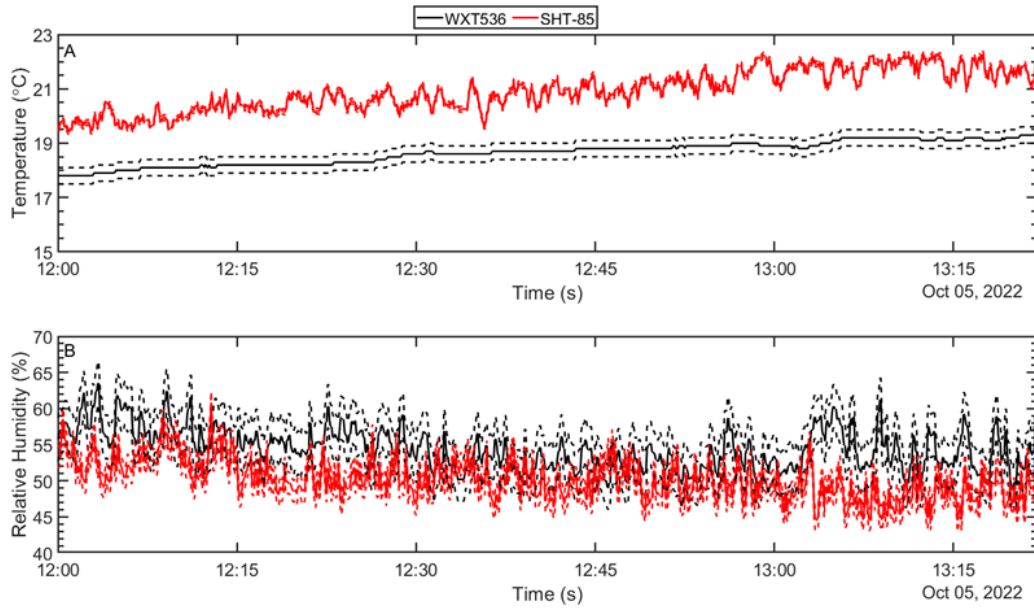
Figure 6 Time series of air temperature (A), and relative humidity (B) obtained aboard the R/V CE (Vaisala WXT536; black) compared to the measurements obtained from NWIPS (SHT-85; red) at a similar altitude (2.37 m above instantaneous sea-surface elevation). Dashed lines correspond to instrument error reported by the manufacturer for each respective sensor.
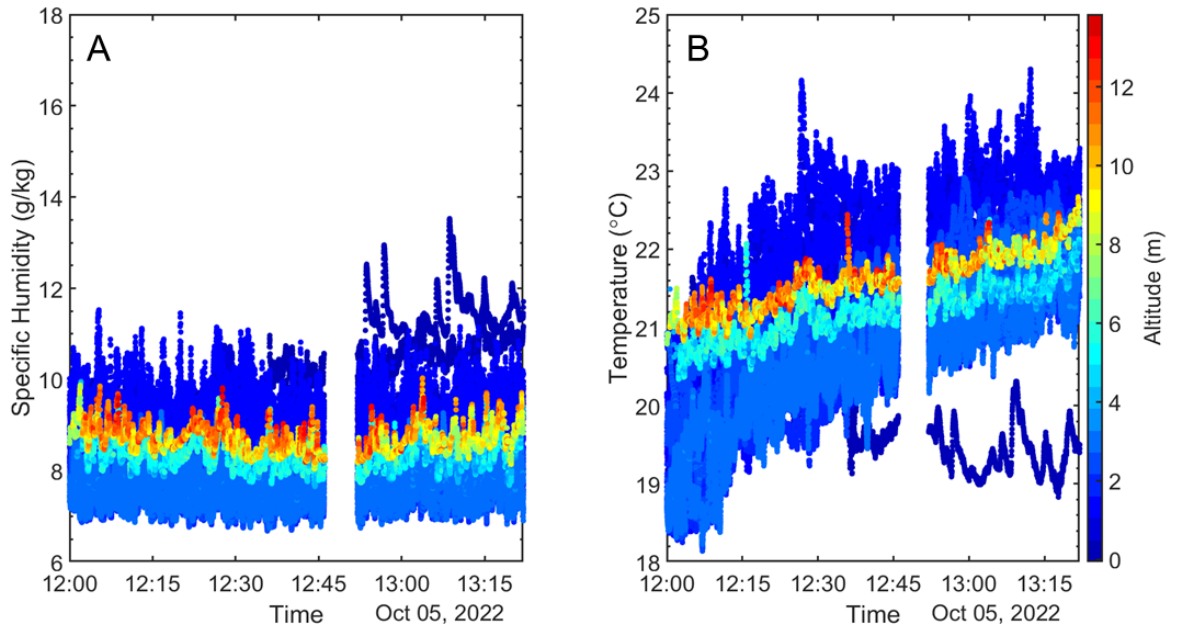
Figure 7 Time series of air temperature (A), and relative humidity (B) obtained onboard NWIPS. The colorbar represents the sensors respective altitude.

3 Temperature and Humidity Vertical Distributions over a Wavy Surface

This chapter discusses ensemble and phase averaged temperature and humidity vertical profile measurements from NWIPS along with supporting bulk meteorological measurements made aboard the R/V CE. The ensemble average profiles are compared to MO theory. The phase-resolved vertical profiles are compared to the ensemble profile, and steadiness of the phase-averaged profiles is also examined. These comparisons as well as discussion of key features of these profiles are presented in the subsequent subsections.

Prior to all analyses, data were first quality controlled. Due to inherent potential for salt-fouling, a pair of redundant sensors were used on NWIPS at the lowest measurement positions. The redundant sensors were covered for the first ~30 minutes of the experiment, and then uncovered to ensure continuous sampling at the lowest measurement positions. Thus, the data from the pair of redundant sensors is merged in this analysis, using the least contaminated sensor for all times (based on duration of exposure). Each vertical profile was visually inspected for outliers and invalid data. Outliers were investigated by visually comparing time series with time series from the two nearest mast positions. No obvious outliers were found during this visual inspection. However, invalid data in the form of sensor failure was observed in the dataset leading to gaps in the vertical profile. The largest

gap in any one instantaneous vertical profile was four consecutive missing data points or sensors. Linear interpolation was used to fill these data gaps.

3.1 Ensemble Vertical Temperature and Humidity Profiles

Direct profile measurements within the MASL are extremely rare, especially at altitudes within 3 m of MSL. Consequently, bulk measurements are often relied upon to extrapolate measured vertical profiles of temperature and humidity to the surface (e.g., Karimian et al., 2013). This section seeks to address the question of how well MO theory (eq 10-11), implemented here via COARE 3.0, can represent NWIPS-measured temperature and humidity vertical distributions?

An instantaneous vertical profile is constructed from the 30 separate temperature and humidity NWIPS mast SHT-85 sensors (see § 2.2; Figure 7) and one sea-surface temperature measurement. These measurements are put into better context with the addition of supplementary measurements made by the Windsonds nominally located at 7 m and 15 m in altitude. Scalar profiles were sampled at 1Hz (temporal resolution of 2 s) providing a total of 4800 instantaneous profiles.

The measured bulk sea-surface temperature (T_B) is corrected to skin temperature by the process detailed in Alappattu et al. (2017). Skin temperature (φ) is defined for low ($U < 4$ ms^{-1}) and high ($U \geq 4$ ms^{-1}) instantaneous wind speeds as:

$$\varphi_l = T_B - \Delta T_l - \Delta T_{local} \qquad (18)$$

$$\varphi_h = T_B - \Delta T_h \tag{19}$$

where subscripts "l" and "h" denote low and high wind conditions, respectively. Correction factors ΔT_l and ΔT_h are defined as (Alappattu et al., 2017):

$$\Delta T_l = 0.035U^2 + (-0.24U) + 0.85, U < 4 \text{ m}s^{-1} \tag{20}$$

$$\Delta T_h = -0.0037U + 0.35, U \geq 4 \text{ m}s^{-1} \tag{21}$$

where U is wind speed obtained from the meteorological station located onboard the R/V CE. In low wind speed regimes, local diurnal heating affects must also be accounted for in (2) as (Alappattu et al., 2017):

$$\Delta T_{local} = 0.11 \sin(10.35t + 0.67) \tag{22}$$

where t is the local hour in 24-hour format (e.g. 1PM = 13). Wind speed is considered the primary driver of variability in sea surface temperature for $U \geq 4 \text{ m}s^{-1}$ (Alappattu et al., 2017).

The profiles were averaged over ten-minute windows. This window length is minimized in order to study time evolution over the experiment to capture larger scale changes such as diurnal variability while also maintaining an average comparable to other studies (see Table 1 in § 1.2). The upper altitude measurements (made by the Windsonds) are also altitudinally bin averaged. Bin averaging of the upper altitudes is required because these measurements vary in altitude as a result of the movement of the balloon caused by the wind. The exact altitude of these measurements is obtained via atmospheric pressure (P_W) measurements made by the Windsonds in conjunction with the surface level pressure

(P_{atm}) measurement from the Vaisala WXT536. The measurements are binned into 0.5 m bins from 4 m up to 15 m and each altitude bin, on average, contains 60 measurements. Altitudes closer to the maximum height extent have fewer measurements than the lower levels since only one Windsond covers this region occasionally. This averaging was performed for specific humidity and temperature, which are subsequently used to estimate modified refractivity (assuming sea-level pressure is uniform in height up to 60m; eq 1).

The Coupled Ocean Atmosphere Experiment algorithm (COARE version 3.0, Fairall et al., 1996; Fairall et al., 2003) uses MO theory to model vertical mean profiles of temperature, humidity, and wind speed. COARE requires the following parameters: sea-surface temperature (SST), and wind speed, pressure, specific humidity, and temperature at a reference height. Pressure and wind speed are obtained from the Vaisala WXT536 weather station. The Windsond temperature and humidity measurements at the 10 m bin-average and the HOBO U20 SST measurements are used in COARE . Specific humidity at the surface is assumed to be 98% relative humidity and uses a saturation value based on the SST (Buck, 1981). All these bulk parameters are averaged over 10-minutes before utilized in the COARE model. This implementation of COARE assumes a smooth sea-surface, which is reasonable because during the experiment wind speeds were primarily < 5 ms^{-1} and sea surface conditions only become fully rough at U > 8 ms^{-1} (Fairall et al., 1996).

Comparisons of the 10-minute NWIPS ensemble averages and COARE are presented in Figure 8 for temperature (A – H), specific humidity (I – P), and modified refractivity (Q – X), and Table 3 shows RMSEs for various altitude ranges for temperature, humidity, and

modified refractivity. In general, the two vertical distributions are similar, especially above

~3 m of altitude. In fact, upper altitude comparisons (> 3 m) match the measured data

remarkably well for temperature (mean RMSE of 0.32 ± 0.04 °C), specific humidity (0.34

± 0.09 g kg^{-1}), and modified refractivity (1.91 ± 0.49 M-units). Relative agreement with

MO theory over all measured altitudes for humidity was also found during the RED

experiment using radiosonde measurements (Davidson et al., 2003 and Anderson et al.,

2004). On the contrary, their temperature comparisons showed discrepancies over all

measured altitudes; these discrepancies were attributed to sensor accuracies. This

difference likely drove the error between the modified refractivity profiles based on

COARE and those measured in the RED experiment (Davidson et al., 2003 and Anderson

et al., 2004). Here, below 3 m, considerable small-scale structure is observed in the NWIPS

ensemble data that is not present in the COARE predictions. Davidson et al., (2003) and

Anderson et al. (2004) under much larger sea-states (i.e., larger U and H_s) showed

deviations from MO theory at altitudes < 3.5 m . These small-scale variations in the vertical

profiles occur for both humidity and temperature, but the vertical structure of the

temperature is more complex than that of humidity. It is clear from comparison of humidity

and modified refractivity vertical profiles (Figure 8) that these low altitude variations of

humidity are the primary contributor to the observed differences between COARE and

NWIPS modified refractivity. Consistent with these observations, the largest RMSEs

between COARE and the measured profiles occur within the 1 m - 3 m range. Modified

refractivity also shows a large RMSE from 0-1 m suggesting surface refractivity, based on

SST, differs.

The small-scale features of the vertical profiles below ~ 3m are clearly contributing to the large RMSEs in the 1-3 m altitude range. Like Anderson et al. (2004), in the RED experiment, it might be logical to assume that these features are driven by variations in sensor accuracy. To explore this concept, we present Figure 9 showing a representative NWIPS temperature and relative humidity profile (Figure 8A for temperature) over the 0 m – 3 m altitude range, so these small-scale vertical variations are more visible. Also shown in Figure 9 are three separate laboratory tests of the NWIPS mast with the same sensors used in the experiment, each configured in a different order. Relative humidity is used for this humidity comparison because supplementary measurements required for conversion to specific humidity were not taken during the three laboratory tests. Very much unlike the data collected in the field, the three control profiles show very little variability with height and time; the standard deviations of measurements are at or very near the manufacturer reported accuracies of the SHT-85 sensor. This comparison with control profiles suggests that either physical processes are driving the observed near-surface vertical structure, or inaccuracies are introduced that are associated with environmental influences; however, individual SHT-85 sensors were also tested extensively over land and enclosed water bodies relative to a MaxiMet weather station (GMX536) with no discernable bias (Stanek and Hackett, 2021), thus, it is conjectured that the former is more likely.

This conjecture is also supported by laboratory and modeling studies of air flow over wavy surfaces. Kruse and von Rohr (2006) using particle image thermometry in a laboratory experiment for similar normalized altitudes (normalized by wavelength), found supporting

evidence of alternating warm-cold pockets of mean temperature. Similarly, using LES simulations, Wagner et al. (2010) found evidence of alternating pockets of warm and cold mean temperatures over both a 2D and 3D wavy surfaces. Kruse and von Rohr (2006), Zhang et al. (2021), and Yang and Shen (2017) all found evidence of highly complex three-dimensional structures similar to those of a type 2 Craik-Leibovich instability (Phillips and Wu, 1994). The effect of the features reported in the LES and laboratory studies on NWIPS profile measurements in the field would show layers of differing mean temperatures as the vertical transect cuts through the warm and cold pockets. And this in-fact, is how the temperature field is structured vertically near the surface supporting the notion that the small-scale near-surface variability is a physical consequence of the coupling of the air and water flow with each other and the associated scalar transport.

Discrepancies between COARE and NWIPS ensemble averages can stem from differences in the universal dimensionless gradient functions (Φ; Drennan, 2006):

$$\Phi_H \left(\frac{z}{L}\right) = \frac{kz}{T_*} \frac{\partial \bar{T}}{\partial z} \tag{23}$$

$$\Phi_W \left(\frac{z}{L}\right) = \frac{kz}{q_*} \frac{\partial \bar{q}}{\partial z} \tag{24}$$

The right-hand-side (RHS) of eq (23) and eq (24) are estimated from the NWIPS data; however, because direct measurement of the fluxes are not available, the scaling parameters (T_*, q_*) are obtained from bulk measurements and transfer coefficients (Garratt, 1977; Smith 1988), implemented via the COARE algorithm (Fairall et al., 1996; Fairall et al., 2003). In COARE, the scaling parameter estimates inherently rely on Φ, which for the

observed stability regime, assumes the Kansas empirical formulation (i.e., Businger et al., 1971) (Fairall et al., 2003).

To obtain the scaling parameters from COARE, the bulk measurements are taken at the 10 m and 1.5 m altitude from the 10-minute ensemble profiles. To compute the gradients of the mean profiles in eq (23) and eq (24) from the NWIPS data, the vertical gradient of the corresponding 10-minute ensemble averaged vertical profile is computed using a least squares approach that minimizes edge effects on the gradient calculation (e.g., Stanek, 2018). Subsequently, a 5-point moving average filter is applied to each ensemble gradient vertical profile to smooth small-scale variability in the gradients. Then, the gradients are averaged over two altitude ranges: 0.3 m $< z <$ 3.2 m and 9 m $\leq z \leq$ 11 m.

The NWIPS-COARE estimated universal dimensionless gradient functions (i.e., RHS of eq (23) and eq (24)) are compared to empirical formulations of other authors in Figure 10. At this atmospheric stability ($\zeta = \frac{z}{L}$; $-0.7 < \zeta < 0$), many of the NWIPS-based results qualitatively agree with the empirical curves within a factor of ~2. Estimates for heat are most in error with five estimates for ~10 m, and two estimates for below 3.2 m showing more significant disagreement with the empirical curves. Deviations of temperature and humidity from the classically held forms was also found by Anderson et al. (2004) for 30-minute averages. These results of departure from the classically held form was confirmed by LES studies by Sullivan et al., (2014) and Jiang, (2020). They also observed larger discrepancies for temperature than for moisture. Some of the empirical curves shown in Figure 10 were derived from land-based data, which has different gradients (Oncley et al.,

1996). The NWIPS-based results for water vapor (humidity) show a consistent positive bias for estimates based on data below 3.2 m relative to the empirical curves, while data from 10 m shows good agreement. This result could be due to the observed small-scale variations in humidity near the surface that was shown to cause differences in modified refractivity near the surface (Figure 8). It is worth noting that some of the observed disagreement could be related to the COARE estimates of the scaling parameters (based on Businger et al., 1971; yellow line in Figure 10) being inconsistent with the measured gradients. Direct measurement of the fluxes would be preferable but obviously not available here due to the lack of wind velocity measurements and the 1 Hz sampling rate being insufficient.

3.2 Phase-resolved Vertical Temperature and Humidity Profiles

In this section, ocean surface wave-phase-resolved vertical profiles of humidity and temperature are investigated to explore how the vertical profile changes over a wave cycle. The subsection first discusses the methods used to compute the wave phase followed by discussion of the phase-resolved profiles and their steadiness over time (i.e., multiple wave cycles).

Utilizing NWIPS onboard subsurface pressure sensor measurements (accuracy of ± 1 cm), sea-surface displacement time series were obtained via the hydrostatic relationship:

$$\eta(t) = \frac{P_{abs}(t) - P_{atm}(t)}{\rho_w g} - h_{offset} \tag{25}$$

where P_{abs} is the absolute pressure measured from the forward located submerged pressure sensor (Figure 3), ρ_w is water density assumed to be 1024 kg m^{-3}, and h_{offset} is the depth of the pressure sensor below the buoy hull MWL. The water density assumption over the range, 1020 kg m$^{-3} < \rho_w < 1030$ kg m^{-3}, leads to differences of < 0.2 cm in $\eta(t)$. The maximum error attributed to the hydrostatic assumption in sea surface displacement time series is ± 0.012 m. Another source of error in the estimated surface displacement is related to the mean pitch angle of the buoy due to wind speed. Steele et al. (1990), obtained a quadratic relationship (drag force varies as the square of wind speed) to estimate (based on the NDBC 3 m discus type buoy, which NWIPS's hull is designed based-on) mean pitch angle:

$$\varepsilon = (1.16 \times 10^{-2})U^2 + (8.81 \times 10^{-2})U + 0.29 \tag{26}$$

Utilizing eq (26) the mean wind-induced pitch angle (ε) is ~1° for the observed experimental wind speeds. Although, this empirical relationship is based on a slightly different buoy design, it still provides a rough estimate on the implications of the pitch motion and subsequently displacement estimates. Under these conditions, the wind-induced mean-pitch angle is assumed to be negligible. It is similarly assumed that any heave motion of the buoy does not significantly impact the displacement estimates due to the size of the buoy and the forward upwind placement of the submerged pressure sensor. The sea surface displacement time series is shown in Figure 11A.

We utilize wave spectra computed using Welch's modified periodogram technique, and validate it with the zero-crossing method, to obtain characteristic sea-state parameters. Welch's modified periodogram (i.e., spectral method) technique applied to twenty-minute sea-surface displacement time series is typically the preferred method of choice for estimating wave-parameters (e.g., Steele et al., 1976; Magnavox, 1986; Steele et al., 1990; and Steele and Mettlach, 1994); however, zero-crossing methods have also been extensively used for wave parameters (Ducrozet et al., 2007; Sobey, 1992; and Francis and Atkinson, 2012). Using Welch's modified periodogram technique, 300-point segments of this sea-surface displacement data with an overlap of 50% for adjacent segments are used to estimate the mean power-spectral density of sea-surface displacement. Prior to computing the spectrum, the sea surface displacement time series are first detrended. This wave spectrum is computed for four 20-minute data-segments. The resulting wave spectra for each 20-minute segment as well as the average wave spectra over all four 20-minute segments is shown in Figure 11B. Apparent in the figure is non-negligible wave energy at the Nyquist frequency suggesting that unresolved wave energy could be impacting the resolved wave spectrum especially at the highest frequencies. The mean peak period (2.4 s) and various peak periods from 20-minute data segments (2.2-2.4 s; Table 4) are all above the Nyquist (2 s); thus, the energy levels are decreasing at the Nyquist frequency, so it is presumed any aliasing effects are relatively minimal. The wave spectra show fairly consistent wave conditions, indicative of a purely wind-driven sea throughout the experiment, with slightly higher wave energy in the latter 20-minute segments.

Peak wave period and significant wave height are computed from the wave spectra. The frequency of the peak spectral energy (f_p) is used to compute the peak wave period ($T_p = 1/f_p$). The significant wave height (H_s) is estimated as $4\sqrt{m_0}$, where m_0 is the zeroth moment of the wave spectrum. Sea-state characteristics for each 20-minute segment are computed and subsequently averaged to provide mean experimental wave conditions: $T_p = 2.3 \pm 0.09$ s and $H_s = 0.18 \pm .02$ m.

Significant wave height (H_s) and peak period (T_p) computed for four 20-minute data segments as well as their average for both methods are provided in Table 4. The zero-crossing method is applied to the detrended surface displacement time series. H_s on average is estimated to be 0.18 m, increasing slightly at the latter times. The zero-crossing method estimates a mean peak period of 2.4 s. The sea state characteristics obtained using Welch's method are used subsequently in this dissertation. The estimated values are compared to nearby buoys from NDBC. This comparison is shown in Figure 12, where wind rose plots and estimated significant wave heights from nearby NDBC buoys are presented. In general, the estimated H_s for this study is relatively similar, but slightly smaller, than that estimated at the Sunset Beach buoy. Instantaneous wind speeds and directions measured during this study are in relative agreement with measurements for the region. Discrepancies for wind speed, wind direction, and significant wave height relative to those from the nearest NDBC buoy (Sunset Beach) is likely due to several factors. First, the Sunset Beach buoy is located closer to shore (~15 km) than the measurements from the CE. This nearshore position may offer some shelter from offshore winds that would be consistent with the slightly lower wind speeds and different wind directions measured at Sunset Beach. Contradictory to

these wind speed patterns, the significant wave height at Sunset Beach is higher than that measured by NWIPS. This difference could reflect slight contamination of the NWIPS displacement estimates by motion of the buoy, as discussed previously.

The ocean surface wave phase is computed based on a Hilbert transform of $\eta(t)$; the Hilbert transform extracts frequency components from non-linear, non-stationary time series. It is computed via a Fourier transform of the detrended sea surface displacement time series $(\eta(t))$ and suppression of Fourier coefficients associated with negative frequencies, followed by an inverse Fourier transform. This procedure results in a complex time series signal from which a phase of the original signal can be extracted, as applied for calculation of ocean wave phase in Hackett et al. (2011). The phases are then binned into four wave phases: crest, trough, upslope, and downslope, demonstrated in Figure 13. The wave crest is located at 0°, wave trough at ±180°, upslope at -90°, and downslope at 90°. Each wave-phase bin spans ±30° of these phase locations. The crest, trough, upslope, and downslope have sample sizes of 855, 670, 696, 790, respectively. Data from other phases are discarded. The phase-averaged sea surface displacement over the 80-minute experiment for each phase are: 0.06 cm, -0.07 cm, 0.0 cm, and 0.0 cm, for the crest, trough, upslope, and downslope, respectively. The minor asymmetry in the 80-minute wave phase-averaged surface displacement for the crest and trough phases may be a consequence of the buoy motion on the pressure measurements.

Eighty – minute wave-phase averaged vertical atmospheric scalar profiles at the various wave phases are relatively similar as illustrated in Figure 14, and are also similar to the 80-

minute ensemble average (average of profiles discussed in §3.1; red line in Figure 14). In order to have enough statistical convergence for the wave phase-averaging, the entire 80-minute time series is needed for the phase-averages; thus, it is most logical to compare them to the 80-minute ensemble rather than an individual 10-minute ensemble from §3.1 – in any case, the 10-minute ensemble profiles over the 80-minute experiment are relatively similar. The similarity of the vertical profiles across wave phases will hereinafter be referred to as profile "uniformity". This vertical profile uniformity means that the profiles do not change their overall/general shape as a function of wave-phase. However, the profiles do shift vertically with the displacement of the sea surface. Vertical shifting of the profiles is largest at the crest and trough compared to the up/down slope phases, as expected. The shifting of the profiles means that the profile in the trough of the wave extends to the surface in a similar manner as it does in other phases of the wave cycle. The inset in panel (A) highlights this vertical shift. Humidity below the MWL (i.e., in the wave trough) seems to extend linearly from the values above MWL. This result is consistent with findings from Schooley (1975), who showed a linear trend between a crest and trough phase in a laboratory study. Profile uniformity over wave phase has also been found in prior numerical and laboratory studies (Yang and Shen, 2017; Kuhn and von Rohr, 2008). The primary difference among vertical scalar profiles relative to MWL is varying location of the small-scale structure in the profile near the surface (discussed in §3.1) due to the vertical shift. For example, locations where a change in slope of the temperature profile occurs shifts up/down with sea surface displacement.

We examine how steady these phase-averaged profiles are, given the variability in the wave field over the time period of the experiments (Figure 11B). Sea-state characteristics are typically estimated from 20-minute averages (Lang, 1987; Steele et al., 1990; Steele and Earle, 1991; Chaffin et al., 1992; and Earle 1996), thus we also adopt this averaging practice for the assessment of phase-averaged profile steadiness. Twenty-minute segments of wave phase-averaged profiles are presented in Figure 15. Panels (A-D) show relative humidity and Panels (E-H) show temperature profiles. Error bars show instrument manufacturer reported sensor accuracy. Relative humidity is used for this comparison because the manufacturer reports accuracy in percent relative humidity, which is used to evaluate whether differences in time are larger than instrument errors. On time-scales of 20-minutes, profiles appear to be steady for the wave conditions during the experiment. There are slight differences that exceed manufacturer specified accuracies at the latter time periods for temperature just below 2 m altitude, which may be related to the slightly larger wave heights at the latter times and could be indicative of the formation/shifting of a cool pocket at this altitude; however, generally, the profiles are all similar, consistent with the relatively similar wave spectra over this time period (Figure 11B).

Table 3 RMSEs between temperature, specific humidity, modified refractivity and corresponding COARE model predictions for each 10-minute averaging window as well as the mean (μ) and standard deviation (σ) of those RMSEs over all eight 10-minute averaging windows.

	0 - 10 min	10 - 20 min	20 - 30 min	30 - 40 min	40 - 50 min	50 - 60 min	60 -70 min	70 - 80 min	$\mu \pm \sigma$
Temperature RMSE (°C)									
$0\,m < z < 1\,m$	1.05	0.72	0.76	0.74	0.82	0.93	1.01	1.00	0.88 ± 0.13
$1\,m \le z \le 3\,m$	1.84	1.34	1.19	1.05	0.93	0.78	0.74	0.62	1.06 ± 0.40
$z > 3\,m$	0.27	0.33	0.27	0.30	0.34	0.30	0.35	0.36	0.32 ± 0.04
Specific Humidity RMSE (g kg^{-1})									
$0\,m < z < 1\,m$	0.89	0.87	0.82	0.51	0.78	0.75	1.07	1.00	0.84 ± 0.17
$1\,m \le z \le 3\,m$	1.42	1.40	1.53	1.25	1.39	1.17	1.58	1.58	1.42 ± 0.15
$z > 3\,m$	0.29	0.34	0.25	0.28	0.40	0.26	0.46	0.46	0.34 ± 0.09
Modified Refractivity RMSE (M-unit)									
$0\,m < z < 1\,m$	4.78	5.02	4.77	2.74	5.05	5.79	7.57	7.14	5.36 ± 1.51
$1\,m \le z \le 3\,m$	7.52	7.97	9.05	7.32	8.42	7.09	9.98	10.06	8.43 ± 1.16
$z > 3\,m$	1.84	1.85	1.27	1.59	2.26	1.40	2.61	2.45	1.91 ± 0.49

Table 4 Sea-state characteristics from zero-crossing and Welch's method. The last column shows the mean (μ) and standard deviation (σ) over all 20-minute segments.

	Parameter	0 - 20 min	20 -40 min	40 - 60 min	60 - 80 min	$\mu \pm \sigma$
Zero - crossing	$H_s\,(m)$	0.14	0.14	0.18	0.25	0.18 ± 0.05
	$T_p\,(s)$	2.65	2.57	2.52	2.25	2.4 ± 0.12
Welch	$H_s\,(m)$	0.15	0.16	0.19	0.2	0.18 ± 0.02
	$T_p\,(s)$	2.31	2.44	2.24	2.27	2.3 ± 0.09
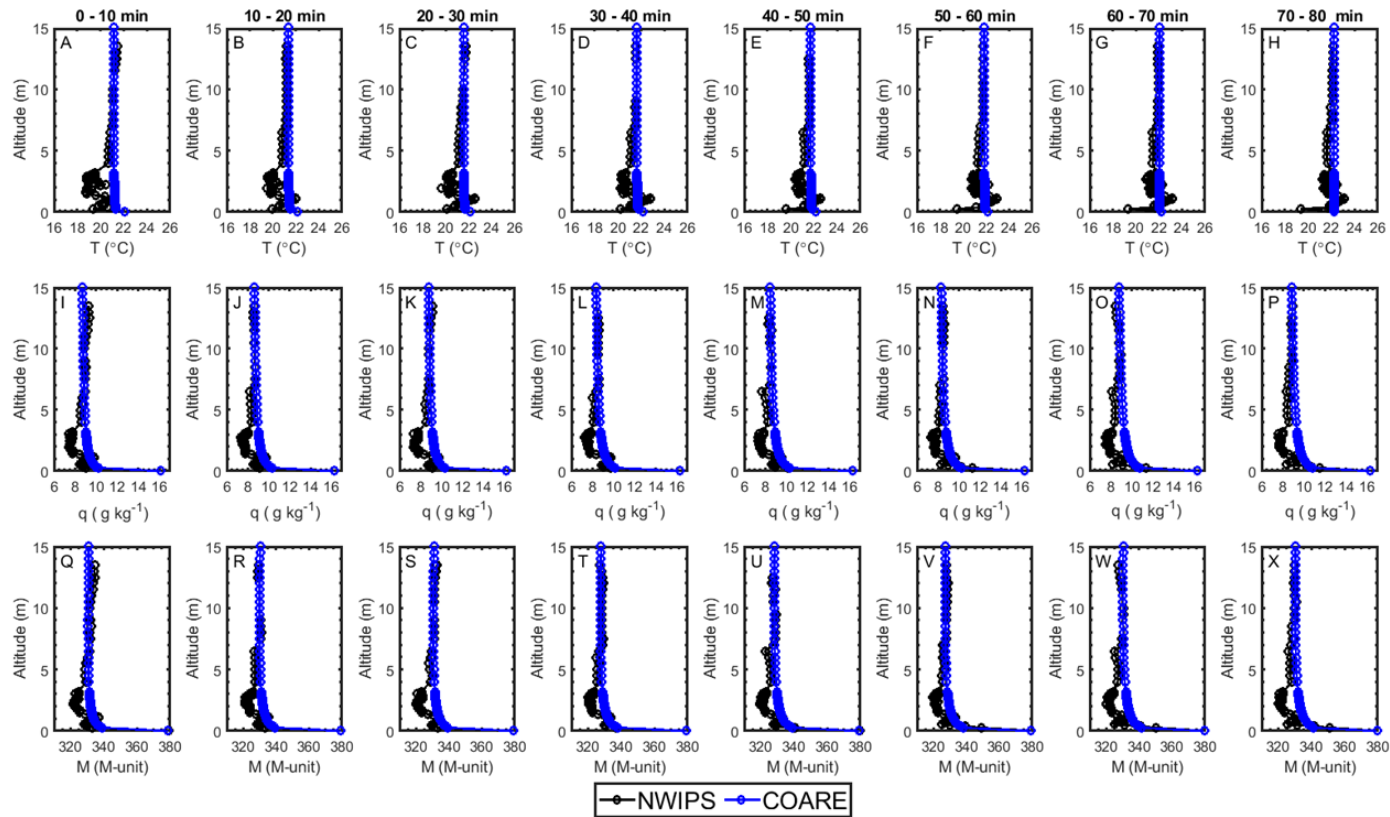
Figure 8 Ten-minute ensemble averaged NWIPS vertical profiles and corresponding MO theory profiles based on the COARE algorithm over the 80-minute experiment (time increasing from left to right). Panels (A - H) shows temperature (T) ; Panels (I – P) shows specific humidity (q); Panels (Q – X) shows modified refractivity (M). Measured ensemble profiles are black, whereas MO theory (COARE) profiles are blue (see legend).
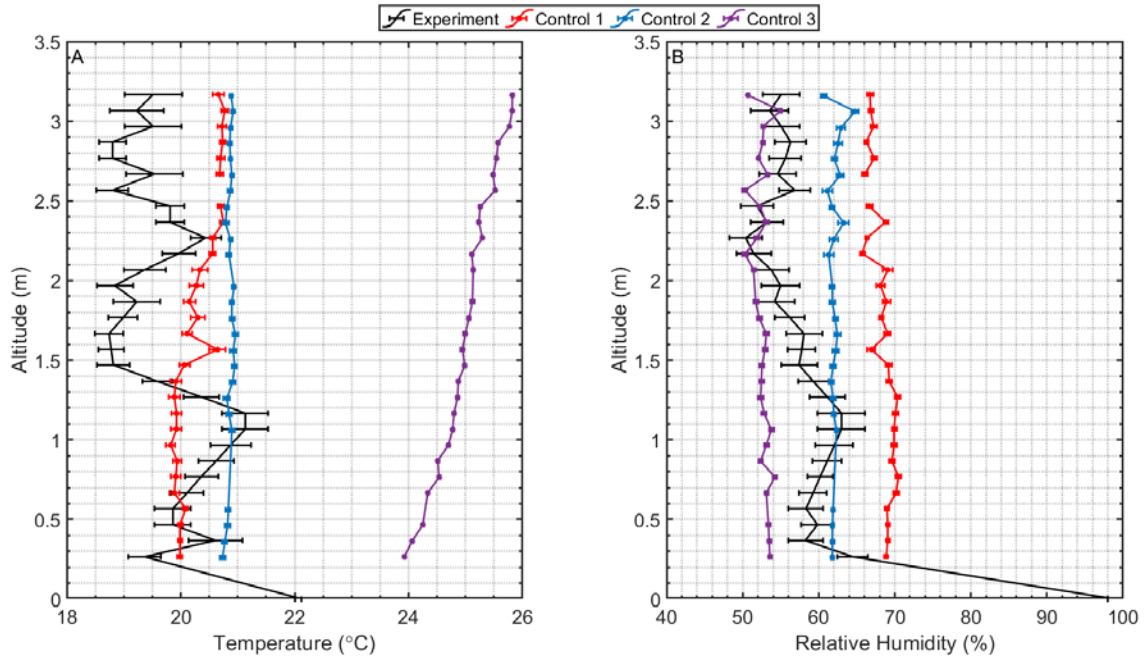
Figure 9 Example 10-minute ensemble averaged profiles of temperature (A) and relative humidity (B) for 0 – 10 minutes (Figure 8A) along with three controlled laboratory datasets for comparison (see legend). Error bars represent the standard deviation of the measurements.
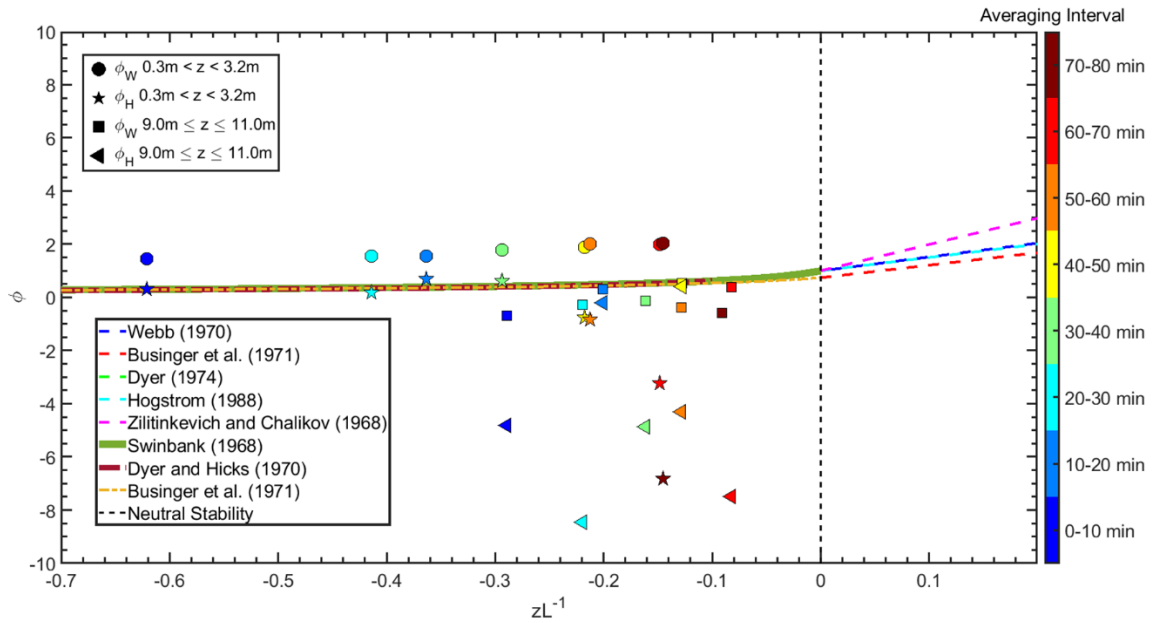
Figure 10 NWIPS estimated dimensionless gradient functions of water vapor and heat compared to the non-dimensional universal stability functions (colored lines) proposed by various authors. NWIPS-based universal gradient functions, shown as markers, the averaging interval (marker color) is indicated by the colorbar.
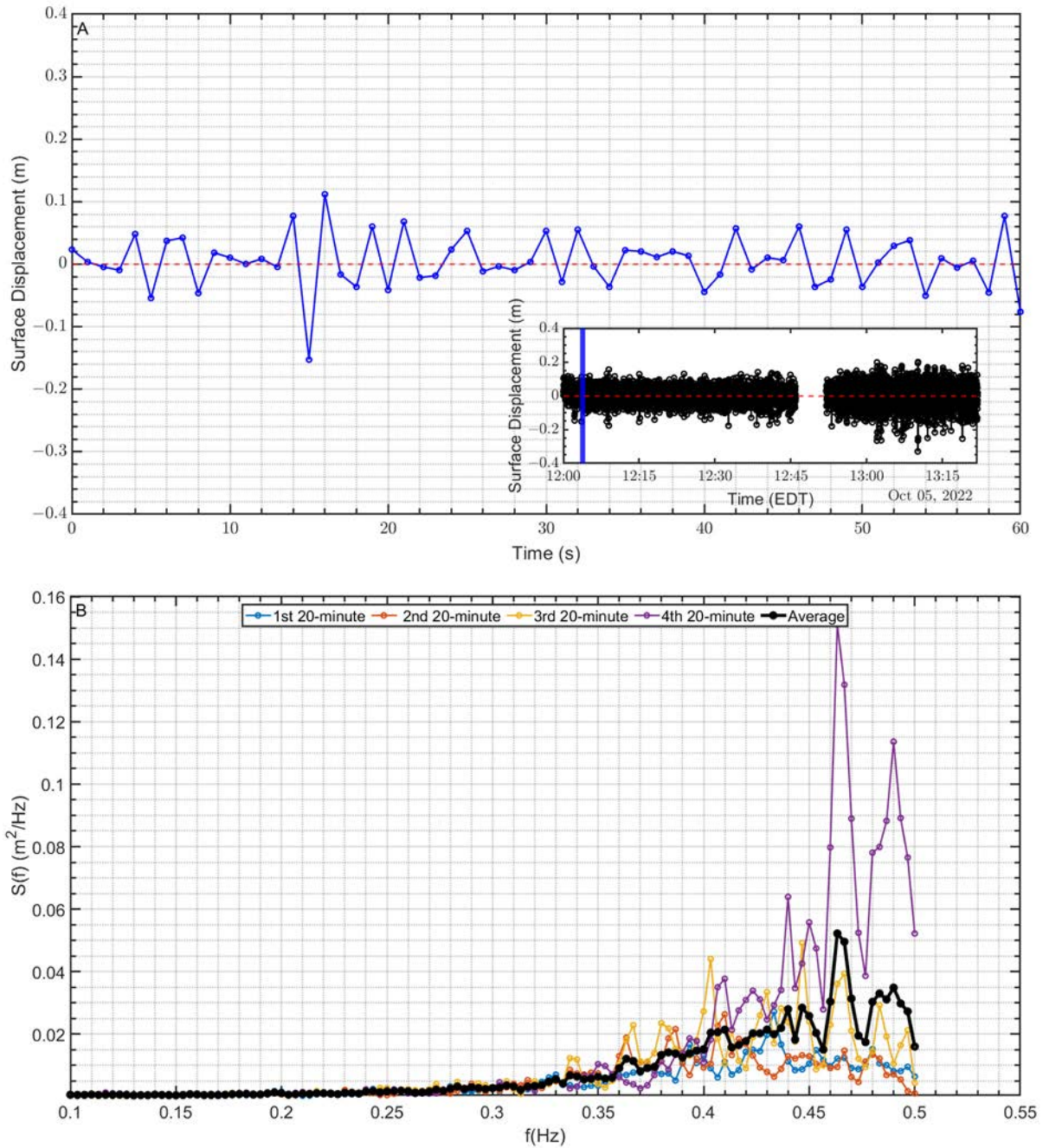
Figure 11 Time series of sea-surface displacement (A) and power spectral density (S(f); PSD) of sea surface displacement (B). Panel (A) shows an example 60 s surface displacement time series indicated by the blue swath in the panel inset showing the entire time-series. Panel (B) show wave spectra for each 20-minute segment. The solid black line indicates the average of the four 20-minute PSDs.
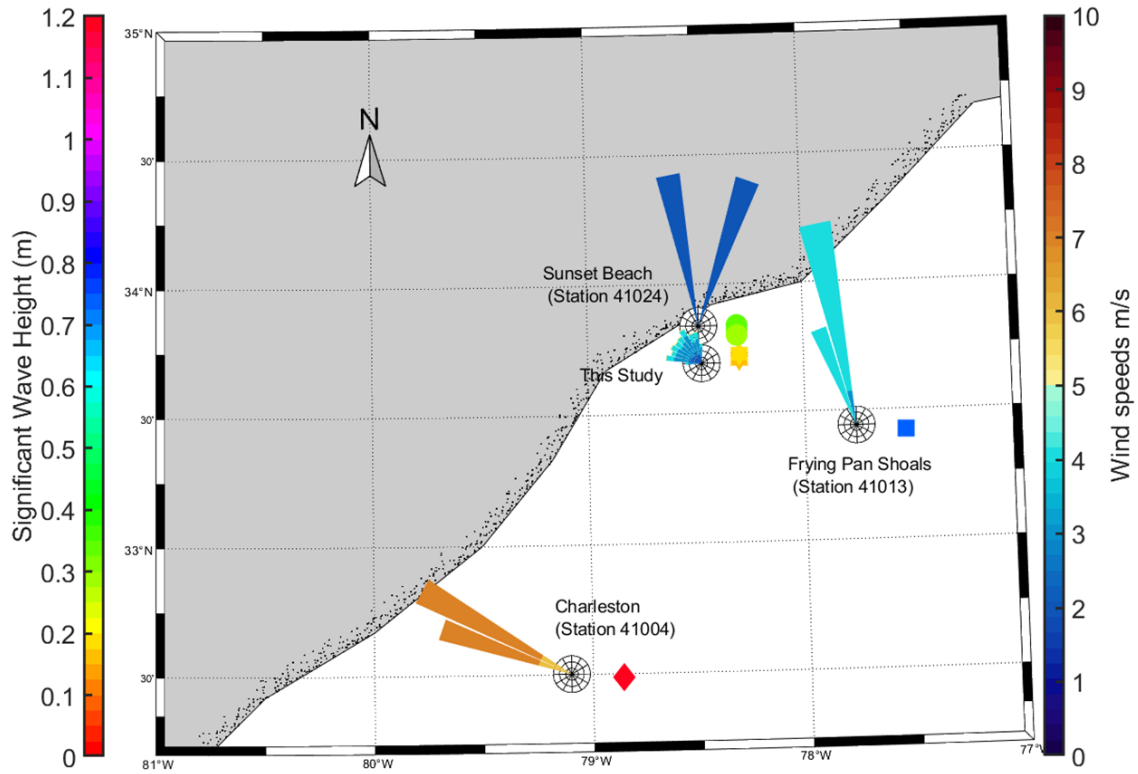
Figure 12 Lambert projection overview map of wind speeds and significant wave heights from nearby NDBC wave buoys and this study. The wind rose plots are located at the buoy coordinates and the H_s are indicated by the colored markers to the right of the respective buoy. Wind speed is represented only by color referenced to the right-axis colorbar and H_s is referenced to the left-axis colorbar.
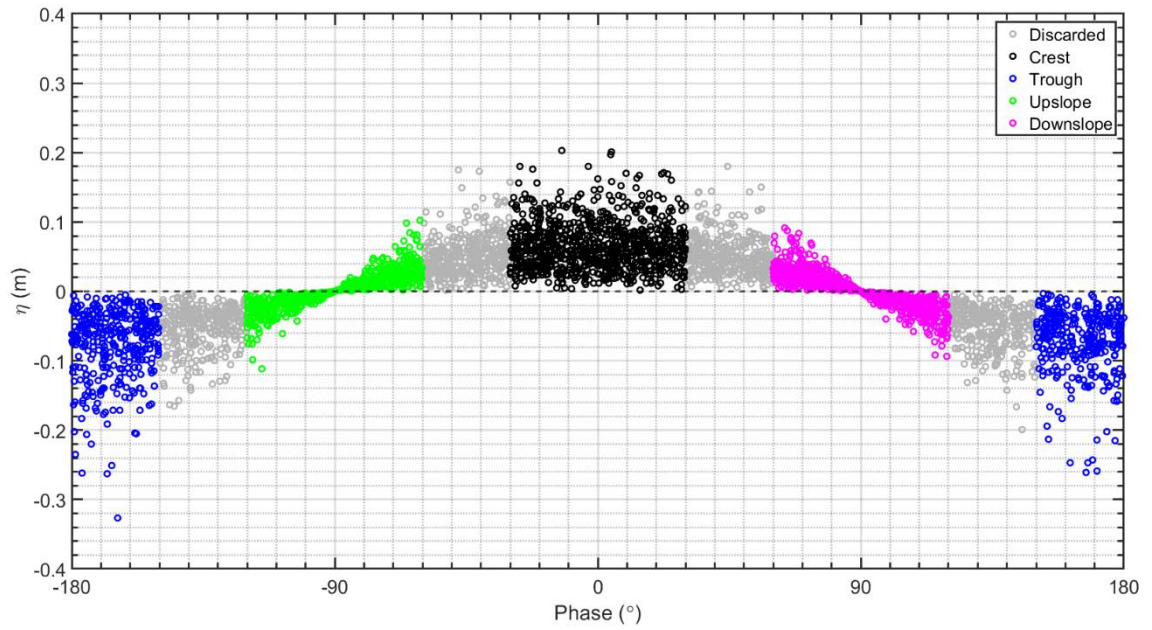
Figure 13 Surface displacement versus phase determined from the Hilbert transform. Wave phase bin is denoted by color (see legend).
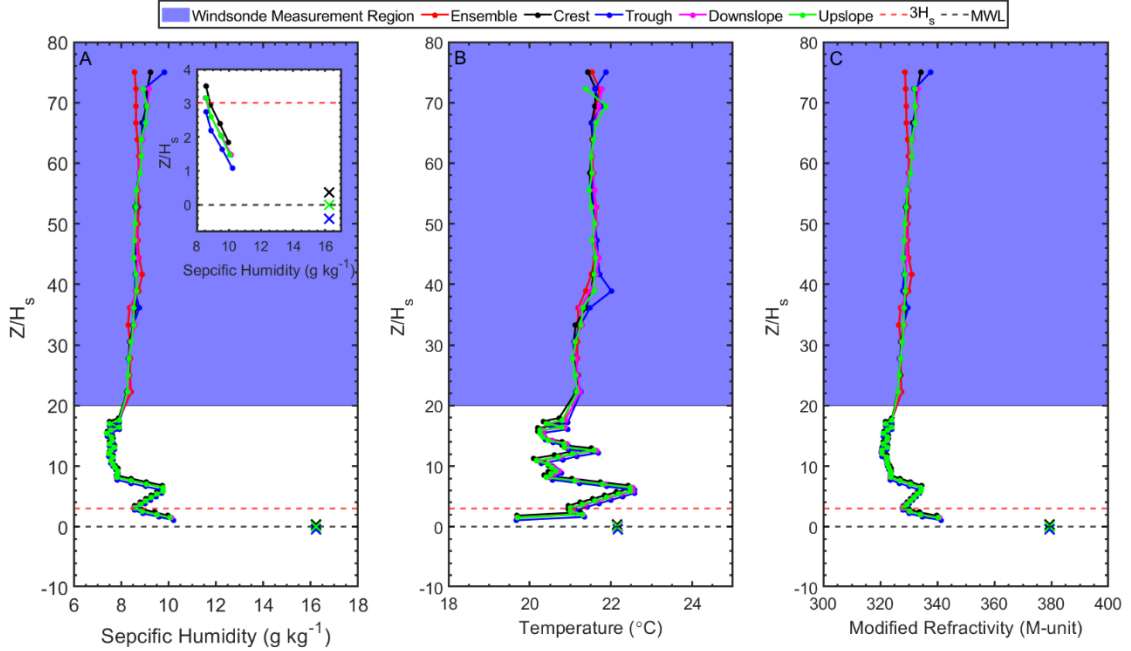
Figure 14 Phase-averaged vertical profiles for (A) specific humidity, (B) temperature, and (C) modified refractivity at the crest (black), trough (blue), downslope (magenta) and upslope (green), and the 80-minute ensemble average profile (red). Inset in (A) highlights the vertical shift of the profiles over phase. The black dashed line represents the mean water level (MWL); whereas, the red dashed line represents $Z = 3H_s$. The $\times$ markers represent the sea surface value for the corresponding profile. Altitude is normalized with significant wave height (H_s) on the vertical axis.
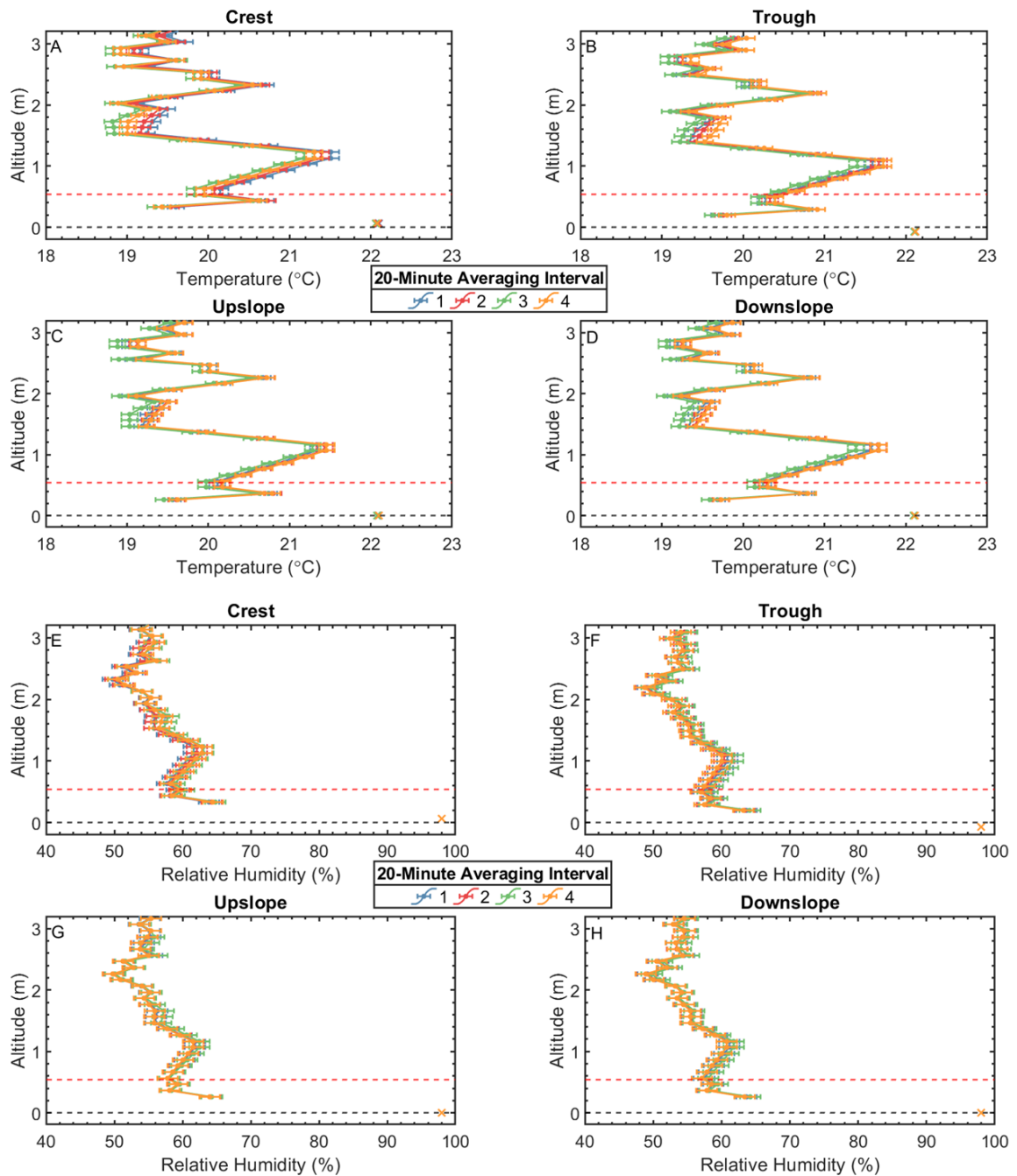
Figure 15 Phase averaged vertical profiles of temperature (A-D) and relative humidity (E-H) for four 20-minute segments corresponding to the periods of the wave spectra shown in Figure 11B. Colored lines correspond to each 20-minute window with segment 1 representing 0-20 minute, and so-on. The black dashed line and red line indicate the location of mean water level (MWL) and 3H$_S$, respectively. Error bars show manufacturer specified accuracy.

3 Temperature and Humidity Vertical Distributions over a Wavy Surface $\qquad$ 63

4 Discussion

The previous chapter focused on investigating vertical scalar distributions over ocean wind-waves, assessing both ensemble and wave phase-averaged results. Our findings revealed the presence of complex humidity and temperature structures near the ocean surface in these mean scalar fields. Further, we observed that variations in the sea surface elevation primarily result in vertical shifts of profiles as a function of wave phase. This vertical shifting causes these structures in the mean field to vary in elevation over the course of a wave cycle. Ten-minute ensemble average profiles were compared to MO theory, implemented via COARE. Below 3 m, comparisons of direct measurements with COARE showed discrepancies – most notably for humidity as these discrepancies for humidity directly translated to changes in refractivity due to its dominance in the computation of modified refractivity (eq 1). In other words, in this range ($z <$ 3 m), despite the presence of unique and complex temperature structures, it is the distributions of humidity that primarily shape the vertical modified refractivity profiles. Although temperature certainly contributes to the profiles, the variations in humidity exert a stronger influence on the overall shape and characteristics of these profiles (Figure 8Q-X).

Accurate estimation of refractivity vertical distributions is vital for accurate propagation loss (PL) predictions in range and altitude; hence the features and discrepancies noted in

Chapter 3 could lead to inaccuracies in the prediction of radar system performance (Lentini and Hackett, 2015; Sirkova, 2012). Thus, in this chapter, we explore the impact of these observations on EM wave propagation predictions to help evaluate the significance of these observations on prediction of radar system performance near the ocean surface. Lastly, the observations of refractivity and their implications on PL predictions lead to some recommendations for improvement of NWIPS in the future.

This chapter is structured as follows: first, in § 4.1, the PL simulation is described as well as how evaporation duct heights (EDH; z_d) are computed from modified refractivity profiles. Following this methodological overview, aspects of ten-minute ensemble averaged (§ 4.1.1) and wave phase-averaged (§ 4.1.2) modified refractivity vertical profiles and their impacts on PL predictions are discussed. Lastly, in section 4.2, improvements of NWIPS for future field experiments are discussed.

4.1 Propagation Loss Predictions

Several modified refractivity profiles are considered: ten-minute ensemble-averaged NWIPS (0-10 min profile; Figure 8Q), 80-minute ensemble averaged NWIPS, 80-minute wave phase-averaged NWIPS, and COARE estimated profiles (COARE uses 10-minute ensemble averaged bulk inputs). All eight, 10-minute averaging windows were similar (Figure 8Q-X); thus, we arbitrarily select the 0–10-minute ensemble average profile for the analysis in §4.1.1. Likewise, the wave phase-averaged profiles are similar at individual

phases for the various 20-minute segments (Figure 15), therefore only the eighty-minute (phase and ensemble) average (Figure 14) is utilized for analysis in § 4.1.2.

NWIPS profiles are blended with a COARE profile at higher altitudes to ensure profiles span the entire PL simulation altitude range. Blending of the NWIPS measured profiles occurs by shifting the COARE profile by the difference between modified refractivity at the 10 m altitude between NWIPS and COARE. The 10-minute ensemble averaged NWIPS profile (Figure 8Q) is blended with a COARE profile based-on 10-minute averaged bulk inputs, whereas the 80-minute (phase and ensemble) averaged NWIPS profiles are blended with a COARE profile which uses 80-minute ensemble averaged bulk inputs. Subsequently, a 5-point moving mean filter is implemented over the blending junction $(9 \text{ m} \leq z \leq 11 \text{ m})$ to smooth any discontinuity between the NWIPS and COARE profiles. Below 9 m the profile is exclusively the measured data; whereas above 11 m the data is exclusively that of the respective COARE profile. Figure 16 shows the 10-minute ensemble averaged NWIPS, 80-minute (phase and ensemble) averaged NWIPS, and the COARE profile implemented in propagation simulations. For reference, also shown in Figure 16, is the COARE profile used for the blending of the 80-minute phase- and ensemble-averaged NWIPS data (although no propagation simulations using this COARE profile exclusively are performed).

Refractivity profiles are used in an EM propagation simulation, the Variable Terrain Radio-wave Parabolic Equation (VTRPE) simulation (Ryan, 1991). VTRPE utilizes a split-step rotated Green's function parabolic equation derived from Maxwell's equation to obtain the

complete wave solution of the EM field (Ryan, 1991). The simulation domain covers 50 m in altitude and 60 km in range with a spacing of 10 cm and 10 m, respectively (500 × 6000 points). A vertical polarized, Gaussian antenna pattern containing two side-lobes with a beam width of 15° was used. PL simulations were performed at 9 GHz (X-band; 3.3 cm wavelength) and 22 GHz (K-band; 1.3 cm wavelength). These radar frequencies are used because X-band is commonly used in maritime navigation and surveillance, and K-band is also examined because of its smaller wavelength that may be more sensitive to smaller-scale atmospheric processes in comparison to X-band. Evaluating effects on two frequencies enables some insight into the sensitivity of the results to the radar frequency. In other words, the two selected frequencies may respond differently to the observations made in Chapter 3.

The location where the gradient of modified refractivity is zero is by definition the evaporation duct height (EDH). EDs have significant impacts on radar systems operating above 3 GHz (Shi et al., 2015a; 2015b), thus accurate estimation of EDH is critical for accurate PL predictions. To estimate EDH from COARE modified refractivity profiles is relatively straightforward by just determining the closest altitude where the slope of modified refractivity changes sign; however, estimating the EDH from the measured data, which exhibit frequent changes in slope of vertical modified refractivity profiles is problematic (Figure 8Q-X). To overcome this challenge, for NWIPS-based profiles, the EDH is estimated using a non-linear least squares fit of modified refractivity to a log-linear function, as performed by Yang et al. (2017):

$$M = f_0 z - f_1 \ln(z + 0.001) + f_2 \qquad (27)$$

where f_0, f_1, and f_2 are empirical constants determined from the fit. The fit-profile is then used to compute the EDH in the same manner as the COARE profiles. An example of a log-linear fit to the first 10-minute ensemble NWIPS profile (Figure 8Q) is presented in Figure 17 along with the associated COARE profile.

The estimated EDHs obtained from NWIPS and COARE differ significantly, with the log-linear fit to the first, ten-minute ensemble averaged NWIPS data (Figure 8Q) yielding a 3.2 m EDH and COARE profiles containing an 8.5 m EDH. The M-deficits (also known as duct strength) between the two methods differ as well: 54 M-units and 48 M-units for NWIPS and COARE, respectively. However, the most apparent disparity between the profiles lies in the curvature or shape of the profiles.

The average second order derivative with altitude (ASOD; $\overline{\frac{d^2M}{dz^2}}$) has previously been used by Pastore et al., (2021) to represent the profile shape from 0.5 m to z_d. The ASOD for COARE and NWIPS is 1.1 M-units m^{-2} and 3.6 M-units m^{-2}, respectively. Pastore et al. (2021) using several different modified refractivity estimation methods, including direct measurements using the Marine Atmospheric Profiling System (MAPS), obtained smaller ASODs . It is worth noting that unlike the MAPS data from CASPER-East utilized by Pastore et al. (2021), NWIPS is capable of capturing small-scale changes in surface humidity as the surface is approached due to its higher vertical spatial resolution and instantaneous profile sampling (versus winching an instrumented balloon); thus the NWIPS data is considered a more accurate representation of instantaneous modified

refractivity profiles at altitudes below a few meters. The small-scale features of the vertical profile, and these differences in profile curvature can drive differences in PL predictions.

The differences in EDH between methods lead to different maximum trapped EM wavelengths. To estimate maximum trapping wavelength the following estimates are used from Kerr, (1951):

$$\lambda_{max} = 0.014z_d^{\frac{3}{2}} \tag{28}$$

and from Turton (1988):

$$\lambda_{max} = \sqrt{\frac{2}{3}(3.77 \times 10^{-3})z_d \; \delta M} \tag{29}$$

where z_d is evaporation duct height (units of feet eq 28; units of meters eq. 29) and δM, M-deficit. Following eq 28 from Kerr (1951) the maximum trapped wavelength for COARE and NWIPS is 2.1 cm (14.5 GHz) and 0.47 cm (63.7 GHz), respectively. Following eq 29 from Turton (1988) the maximum trapped wavelength for COARE and NWIPS is 1.61 cm (18.6 GHz) and 0.93 cm (32.2 GHz), respectively. Based on these estimates of maximum trapping wavelength, only COARE refractivity profiles for K-band frequency would result in trapping. This difference in trapping demonstrates how the observed differences in refractivity can result in very different propagation predictions.

Based on these EDH estimates, propagation simulations were divided into a few different scenarios with respect to the transmitter height, where transmitter heights are simulated at: (i) 3.2 m - at the EDH (estimated from the log-linear fit) for NWIPS and below COARE

EDH, (ii) 8.5 m - at the COARE EDH and above NWIPS EDH, and (iii) 10.5 m - above

EDH for both NWIPS and COARE. A scenario of a transmitter being below both NWIPS

and COARE duct heights was not considered due to the low duct height for NWIPS.

4.1.1 Propagation Loss Predictions for Ensemble Vertical Modified Refractivity Profiles

First, a range independent refractivity scenario is investigated. It utilizes a single

refractivity profile over range over a smooth ocean surface. PL predictions for the 10-

minute ensemble NWIPS and COARE modified refractivity profiles (Figure 16) are

presented in Figures18 for X-band and Figure 19 for K-band.

Comparison of PL patterns for X-band for the various transmitter heights reveals that

COARE modified refractivity vertical profiles lead to less propagation loss (PL) than the

10-minute ensemble NWIPS blended modified refractivity profiles especially at low

altitude long range. Differences for both frequencies are most significant for the lowest

transmitter height. For K-band, COARE and NWIPS PL predictions are similar for the

higher two Tx; trapping is observed for K-band COARE refractivity profiles for Tx = 3.2

m, as predicted. Most of the differences, of course, stem from the different duct heights of

the two profiles. In the case of the Tx=10.5 m, above both duct heights, the differences in

PL predictions are generally the smallest. The notable differences between the COARE and

NWIPS PL at low altitudes is likely also driven by the stronger vertical gradients exhibited

by the measured 10-minute ensemble average NWIPS modified refractivity profiles. It is

also evident that small scale features of the NWIPS-based refractivity cause fine scale

variability in the PL predictions that are not present for the COARE profiles. Additionally, it is worth noting that although most of the observed differences are beyond the geometric horizon, line-of-sight differences are observed for the lowest Tx. Overall, these comparisons suggest that differences in the near-surface modified refractivity estimates can impact PL predictions, especially at low altitude long range.

Transmitters located directly at the EDH represent an anomalous geometry; however as discussed previously, a transmitter located below 3.2 m is relatively low and is why it is selected in this study as the maximum transmitter height for a likely trapping scenario. To investigate how dependent results associated with a Tx = 3.2 m are on this anomalous geometry, PL comparisons with predictions for a Tx = 2.0 m were performed (not shown). In the X-band operating frequency, no significant differences were observed ; however, in the K-band frequency, the alternating pattern of high and low PL beyond the horizon were not observed for Tx = 2.0 m. As a result, the long-range PL over the horizon exhibited better agreement with COARE PL for Tx= 2.0 m. Thus, the presence of the alternating pattern, which is observed only when EDH is at the transmitter height, is likely a consequence of this unique geometry. In addition, this result suggests higher operating frequencies are more susceptible to this anomalous configuration. Nonetheless, all other observations related to the Tx = 3.2 m height generally persist when at Tx = 2.0 m.

To further investigate the impact of small-scale variability/features on propagation loss (PL), we focus on transmitter heights of 10.5 m and 3.2 m and evaluate modified refractivity profiles with incorporation of these features to various degrees. The 10-minute

ensemble NWIPS modified refractivity profiles have particularly prominent features at altitudes of ~1 m and 2-3 m, as shown in Figure 20A and 21A. The feature at ~1m indicates a smaller duct embedded in the larger evaporation duct and the feature between 2-3 m showing small oscillatory variations.

Three modified refractivity profiles are simulated: the 10-minute ensemble NWIPS profile, the same profile smoothed with a 5-point Gaussian filter (Smooth), and this latter profile with the feature at ~1 m removed (Featureless). Removal of the feature at ~1 m is done visually, but in a manner to preserve the overall shape and to avoid mirroring the COARE profile shape. To remove the feature at z = ~1 m, the data at 0.5 m $< z <$ 1.5 m is removed from the vertical profile and the gap interpolated using splines in an attempt to preserve shape of the profile. This process is repeated again at a slightly higher altitude (1.0 m $< z < $ 2.3 m). A two-step spline process was performed in lieu of removing the data over the entire range (0.5 m $< z <$ 2.3 m), because it better preserves the profile shape visually. To avoid fitting the data (and mirroring COARE profile shape) to determine EDH, as done in §4.1, for this analysis only, we define the EDH as the altitude of minimum modified refractivity. Thus, the EDHs in this analysis, by this definition, occur at 2.3 m, 2.2 m, and 2.1 m for the Ensemble, Smooth, and Featureless profiles, respectively. The similar duct heights mean that observed differences in PL predictions are not driven by duct height differences, allowing investigation into the role of the small-scale refractivity features in propagation predictions. These three profiles are shown in Figure 20A and 21A, and PL predictions are presented in Figures 20B-K and 21B-K for X-band and K-band, respectively.

When comparing the propagation loss (PL) patterns at different frequencies and transmitter heights in Figures 20 and 21, the largest differences are between the Ensemble (NWIPS) and COARE PL, consistent with the results in Figure 18 and 19. Most of this difference stems from the differing duct heights between NWIPS-based profiles and COARE. Clearly, the removal of the features makes little difference in the propagation predictions for X-band; for K-band there is increased PL at low altitude long range as the small-scale features are progressively removed. This difference between the impacts at the two different frequencies is likely related to the differences in the maximum trapping wavelength between the two frequencies. These results are also demonstrated in Figures 20J-K and 21J-K.

4.1.2 Propagation Loss Predictions for Phase Resolved Vertical Modified Refractivity

Propagation loss is predicted using the 80-minute (ensemble and phase-averaged) profiles discussed in Chapter 3 (Figure 14), and predictions are compared for profiles at various wave phases and with the 80-minute ensemble average NWIPS modified refractivity profiles. First, a range independent refractivity scenario is investigated. It utilizes a single refractivity profile over range over a smooth ocean surface. Simulations are performed for two transmitter heights: 10.5 m (above the NWIPS EDH) and 3.2 m (at NWIPS EDH). Like §4.1.1, we investigate PL predictions for both X-band and K-band frequencies.

To quantify differences among wave-phase averaged profiles, we utilize the mean absolute difference of PL (MAD) over certain regions of the domain, which provides a statistical

measure of discrepancies between PL predictions for the various wave phases. Figure 22 depicts four regions over which the mean absolute difference is calculated. The regions of interest are the near-surface/near-range (0 m $\leq z \leq$ 25 m; 0 km $\leq r \leq$ 30 km); near-surface/long-range (0 m $\leq z \leq$ 25 m; 30 km $\leq r \leq$ 60 km); high altitude/near-range (25 m $\leq z \leq$ 50 m; 0 km $\leq r \leq$ 30 km); and high altitude/long range (25 m $\leq z \leq$ 50 m; 30 km $\leq r \leq$ 60 km). This approach is preferred over evaluating PL along single or multiple range transects, as the chosen transects may not be representative of the overall results throughout the propagation domain, or region of interest. Results are shown in Figures 23 and 24 as well as Table 5.

Results are frequency and transmitter height dependent. In general, less differences are observed between the ensemble and wave phases for X-band for both transmitter heights compared to K-band which shows non-negligible differences at both transmitter heights. For X-band at both simulated transmitter heights, the MADs are generally below 10 dB and often close to a typical measurement accuracy of 5 dB (Goldhirsh and Dockery, 1998). Largest discrepancies are observed for K-band with a transmitter above the EDH, especially in the long range and low altitudes (Table 5). The differences in the PL predictions between the ensemble and wave phase-averaged refractivity for K-band suggest K-band propagation is more sensitive to the location of small-scale features of the refractivity profile near the surface (see Figure 17), which is consistent with the results shown in Figure 21 (comparing PL with various levels of small-scale features included).

These results demonstrate that differences in PL predictions are observed using phase-averaged profiles relative to PL based on the ensemble. However, these simulations are unrealistic in the sense that, for example, a single wave phase profile would not exist homogenously over range. Thus, to further investigate whether PL prediction differences exist when using phase-averaged refractivity relative to an ensemble refractivity, a range inhomogeneous case is examined. It is possible that variation/oscillation of features associated with the profile (e.g., EDH) over range will result in different effects than those shown in Figures 23 and 24.

To implement range dependent refractivity over a wavy surface, the 80-minute wave phase-averaged NWIPS-COARE blended profiles are utilized to build a heterogeneous refractivity environment assuming a monochromatic wavy (sinusoidal) surface. The wave phase-averaged NWIPS-COARE blended profiles are located at their respective phase locations along a single wavelength and repeated in range. The modified refractivity profiles are coupled to the "terrain" in range, where the prescribed terrain surface properties are representative of sea-water (i.e., temperature (~22°C) and salinity (35 ppt)). However, it should be noted that this approach does not account for the diffusive and scattering effects which result from the presence of capillary waves over the ocean. The initial terrain phase (at r = 0 km) corresponds to the crest wave phase. Recall from § 3.2, that the phase-averaged surface displacement at the crest-phase and trough-phase was 0.06 m and -0.07 m, respectively. The upslope and downslope phases were not displaced relative to MWL. Despite the asymmetry in wave crest and trough amplitudes, potentially due to sensor positioning errors (Chapter 3), the measured phase-averaged displacements are used as the

displacements of the terrain at the crest and trough, respectively, in order to match the measured conditions as precisely as possible. This terrain, and the resulting shifts of the modified refractivity profiles, results in a duct height range of $3.13 \text{ m} \leq Z_d \leq 3.26 \text{ m}$. For comparison, the ensemble averaged NWIPS profiles are fixed to the same above-mentioned terrain surface, but do not vary with wave phase; in other words, the duct height shifts with the surface but the refractivity profile is always the same. Again, we simulate for both X-band and K-band, and transmitter heights of 10.5 m and 3.2 m. This setup is illustrated in Figure 25.

Figure 26 shows PL predictions based-on the phase-averaged refractivity in comparison to using an 80-minute ensemble refractivity over a wavy surface. Similar to the results in Figure 23, the comparisons show little effects from the phase-averaged refractivity relative to the ensemble at X-band for both transmitter heights. In contrast, K-band PL predictions do differ depending on whether the phase-averaged or ensemble profile is simulated over the wavy surface – also similar to the results in Figure 24. Discrepancies for K-band are especially large at long range.

To further explore the impact of the differences between the wave phase-averaged refractivity profiles and the ensemble profiles over a wavy surface, we simulate a more severe sea-state based on the World Meteorological Organization's sea-state code 4. The low wave conditions observed during the NWIPS experiment may be one of the reasons that differences in PL predictions are not observed in Figure 27 for X-band, but do exist in the long range for K-band. Sea-state code 4 is categorized as "moderate" with wave heights

ranging from 1.25-2.5 m. On the Beaufort scale, it falls between a high-end sea-state 4 and a low-end sea-state 5, referred to as "Moderate" to "Fresh Breeze" (World Meteorological Organization, 1970). For this simulation, a wave height and wavelength of 2.0 m and $L_w = 56.2$ m ($T_P = 6$ s) are used. For this analysis, a transmitter height of 3.2 m is used, which corresponds to the estimated evaporation duct height (EDH) from NWIPS, as shown in Figure 17. This setup results in an EDH range of 2.2 m $\leq Z_d \leq$ 4.2 m. The corresponding PL patterns are presented in Figure 27.

The results shown in Figure 27 are remarkably similar to those shown in Figure 26, suggesting the magnitude of the shift of small-scale features of the profile does not change PL predictions significantly. Lastly, comparisons of propagation predictions using the NWIPS 80-minute ensemble refractivity over a smooth surface to that over the NWIPS-based wavy surface (with shifting evaporation duct height over range) are presented in Figure 28. Interestingly, this comparison shows differences in similar locations within the domain as shown in Figures 26 and 27, but are much larger in magnitude (sometimes exceeding as much as 50 dB). This demonstrates that the vertical shifting of the duct height (and/or introduction of a wavy surface at the bottom boundary) causes larger differences in propagation predictions than the observed differences in refractivity with phase.

4.2 Improvement to NWIPS

The discussion in §4.1 highlights the importance of the observed differences in modified refractivity near the ocean surface on PL predictions. Understanding the relationship between sea-surface variability and its role in creating distinct near-surface structures can help improve the accuracy of PL predictions and enhance the performance of radar systems operating in maritime environments. A major limitation of the findings in this dissertation are that it represents only one experiment at one location on one day. Thus, more data under a wide variety of environmental conditions at a variety of locations is needed to draw more definitive conclusions on the universality of the results presented herein. Specifically, different atmospheric stabilities and wave conditions should be explored. However, in order to obtain more robust NWIPS data, several improvements to the NWIPS platform are needed.

NWIPS was developed as a proof-of-concept platform on a limited budget that is not reliable and robust enough to sustain long-term deployment. One of the needed areas of improvement is more robust electronics integration and a stable data acquisition system. These improvements would progress the reliability of NWIPS, and improved time synchronization could be accomplished through incorporation via GPS signal. Furthermore, a telemetry package would enable real-time measurement evaluation and provide insights on damage to the lowest altitude sensors enabling their replacement immediately upon failure, or equivalently switch over to a back-up sensor. In this experiment, we approached this issue with back-up sensors (that were initially covered),

but we had to guess when the original sensor may have been damaged; real-time data would enable sensor replacement to be more precise.

Although the onboard SHT-85 sensors were extensively tested against a Gill MaxiMet weather station, under a wide range of environmental conditions (Stanek and Hackett, 2021), and are cheap so that sensors can be replaced at low cost, an improved sensor housing is needed to make them durable enough to withstand harsher conditions. We speculate based on the results presented herein that the maximum operating sea-state would be a function of the sensors and not the platform, which is why this improvement is so critical.

In terms of the data acquired, the nearby weather station on the R/V CE was useful, but a mast-mounted weather station would be ideal, particularly because it would provide a wind speed and direction at the buoy location, and also enable correction to the SHT-85 measurements as needed. In this study, surface displacement was attained via pressure measurements and the hydrostatic relationship, but a more accurate and common method to obtain surface displacement would be better, such as displacement from buoy acceleration. To obtain displacement from acceleration, experimental testing to obtain response amplitude operators (RAOs) of NWIPS is required to accurately evaluate the heave motion of the buoy. With known RAOs, the existing onboard AHRS system would be able to provide surface displacement more accurately.

Table 5 *MAD (dB) between PL for 80-minute ensemble-averaged and 80-minute wave-phase-avereaged modified refractivity for each of the four phases and regions (Figure 22).*

Region	Phases	X-band (9 GHz)		K-band (22 GHz)	
		Tx = 10.5 m	Tx = 3.2 m	Tx = 10.5 m	Tx = 3.2 m
Near Surface/Near Range (I)	Crest	4.4	4.1	9.7	6.9
	Downslope	3.1	3.7	8.1	6.1
	Trough	3.4	3.4	7.6	6.5
	Upslope	3.9	3.7	8.6	7.2
Near-Surface/Long Range (II)	Crest	4.2	3.3	24.9	8.3
	Downslope	3.1	2.5	21.8	8.1
	Trough	3.5	3.3	22.3	9.6
	Upslope	3.8	3.4	24.1	9.8
High Altitude/Long Range (III)	Crest	7.2	3.7	22.1	9.9
	Downslope	5.4	2.9	17.8	9.1
	Trough	5.6	3.6	16.4	11.0
	Upslope	6.3	3.7	18.9	11.5
High Altitude/Near Range (IV)	Crest	1.5	2.6	4.0	5.0
	Downslope	0.9	1.7	2.7	3.9
	Trough	1.1	2.2	2.9	4.3
	Upslope	1.2	2.4	3.2	4.7
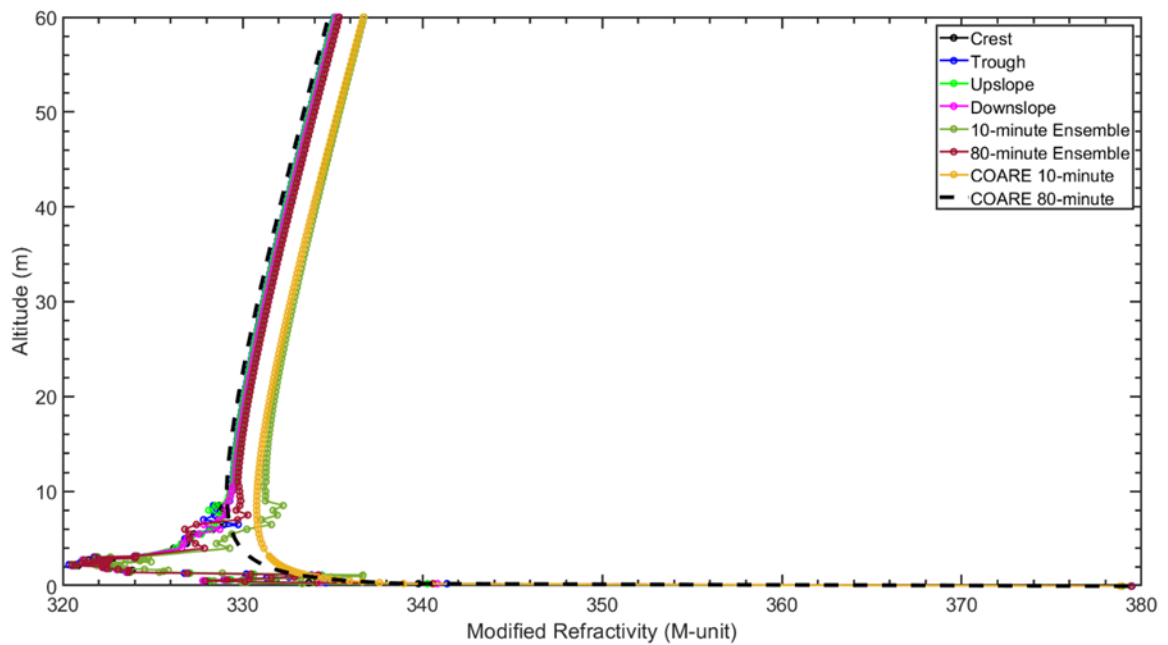
Figure 16 Modified refractivity profiles implemented in VTRPE. The 10-minute Ensemble NWIPS and COARE 10-minute modified refractivity profiles are utilized in § 4.1.1; whereas, the 80-minute Ensemble NWIPS, and 80-minute phase-averaged NWIPS for the crest, downslope, trough, and upslope phases, are utilized in § 4.1.2. The COARE 80-minute profile is added for reference and is used for upper altitude modified refractivity in the (blended) 80-minute ensemble and phase-averaged NWIPS data.
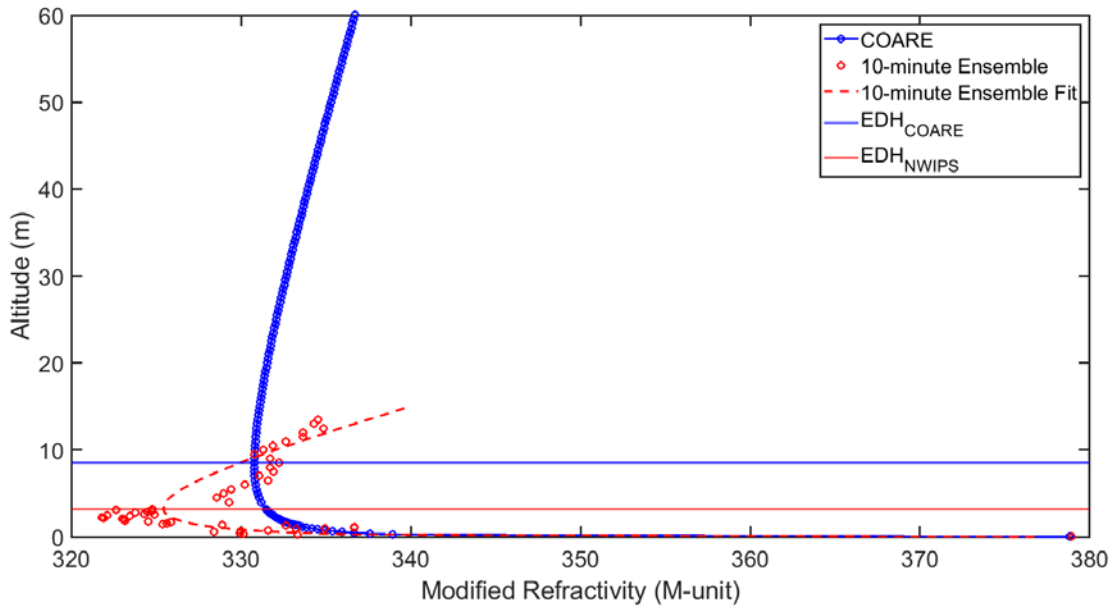
Figure 17 Non-linear least squares fit of NWIPS 10-minute ensemble data (Figure 8Q) to eq (27) to obtain an EDH estimate from NWIPS data. The measured data are represented by red circles. The resulting profile fit of NWIPS is represented by the red dashed line and EDH estimates are indicated by solid horizontal lines. Colors correspond to each data set type (see legend for color representation). The NWIPS – Fit and COARE EDHs are 3.2 m and 8.5m, respectively.
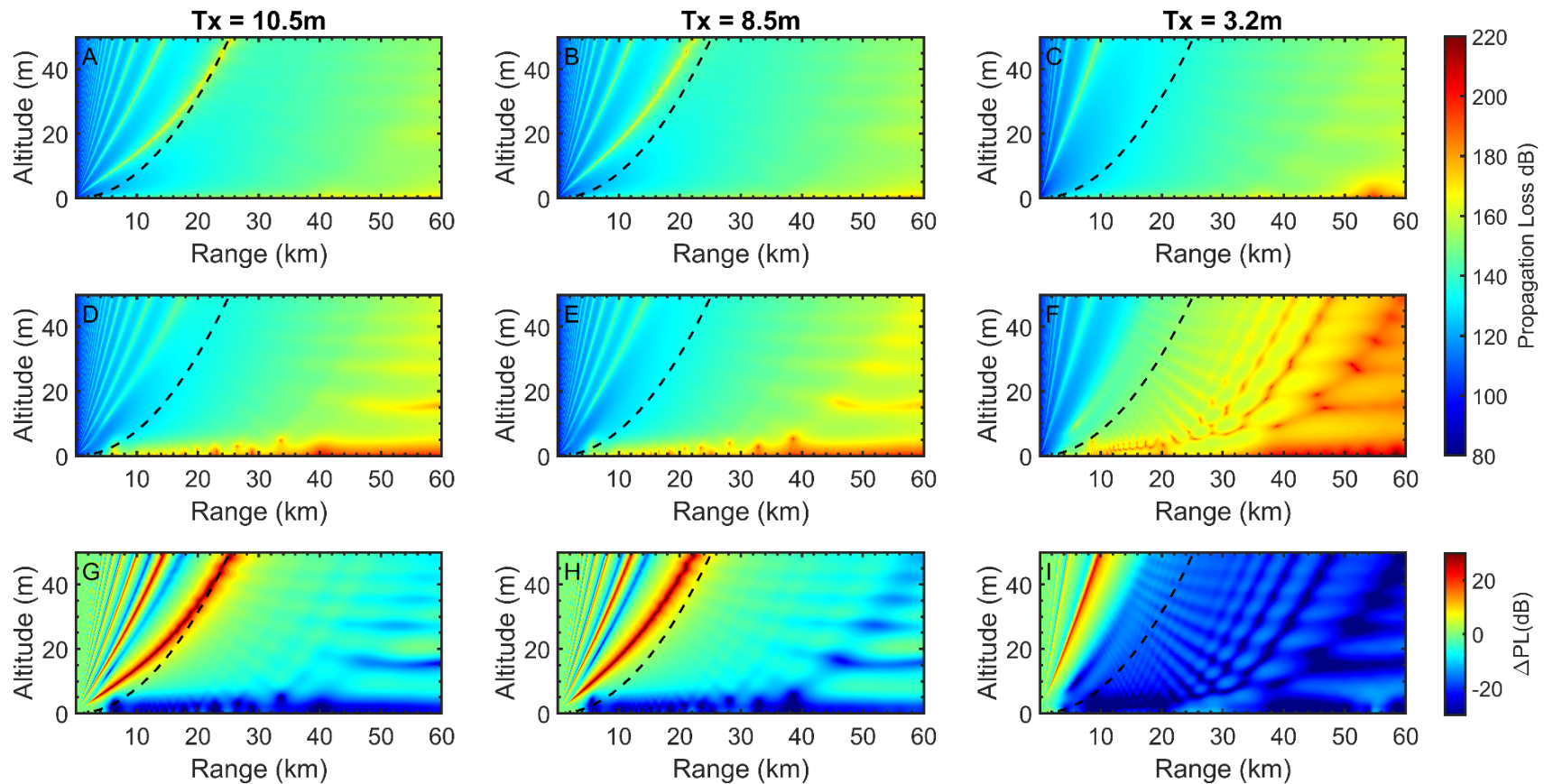
Figure 18 X-band PL predictions for COARE and 10-minute ensemble averaged NWIPS-COARE blended modified refractivity vertical profiles. Transmitter (Tx) heights are listed at the top of each column. Panel(A-C) shows PL from COARE modified refractivity; Panels (D-F) shows PL from ensemble average NWIPS-COARE blended modified refractivity; and Panels (G-I) show the differences between A and D, B and E, and C and F, respectively. Black dashed line represents the geometric horizon. Negative values for ΔPL indicate lower PL for COARE than NWIPS, whereas positive values indicate higher PL for COARE.
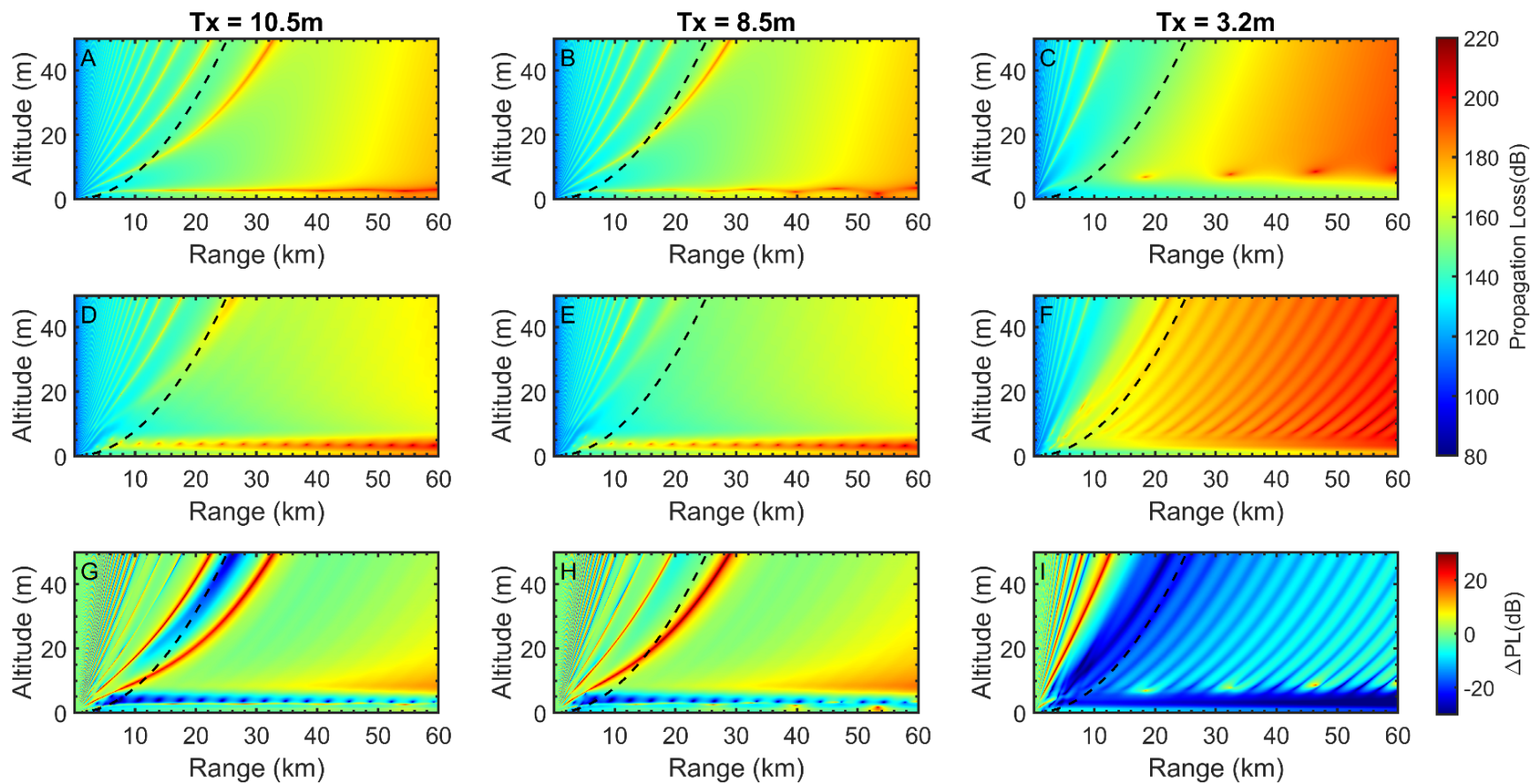
Figure 19 *K-band PL predictions for COARE and 10-minute ensemble average NWIPS-COARE blended modified refractivity profiles. All other aspects of the figure are as described in Figure 18 caption.*
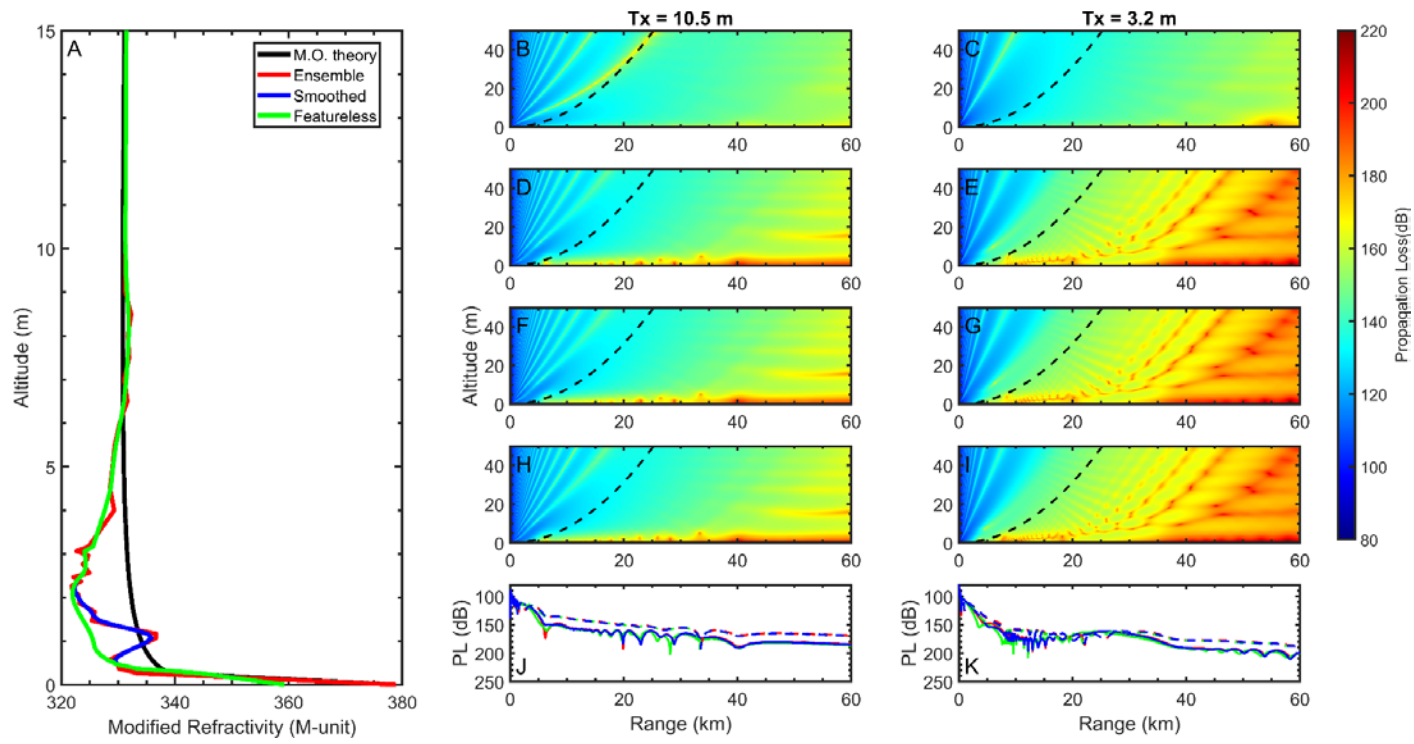
Figure 20 Comparison of X-band PL predictions for ensemble NWIPS modified refractivity profiles with various degrees of small-scale features included in the profiles. (A) Modified refractivity versus altitude for the 10-minute ensemble of the measured NWIPS data (red) and is labeled as Ensemble; Smoothed (blue) utilizes a 5-point Gaussian smoothing function on the Ensemble profile to remove inflections at approximately 2 < z < 3 m; Featureless (green) utilizes a spline interpolation applied to the Smoothed profile to remove the feature present at z = ~1m. Panels (B-C) show PL patterns for COARE; Panels (D-E) show PL patterns for Ensemble; Panels (F-G) show PL patterns for Smoothed; and Panels (H-I) show PL patterns for Featureless. The geometric horizon is indicated by a black dashed line on the PL pattern subfigures. Panels (J-K) show PL at receiver heights of 2 m (dashed) and 13 m (solid) for each data set type (see legend in A for color representation). Transmitter heights are indicated above each column. Colorbar indicates PL (dB).

4 Discussion   85
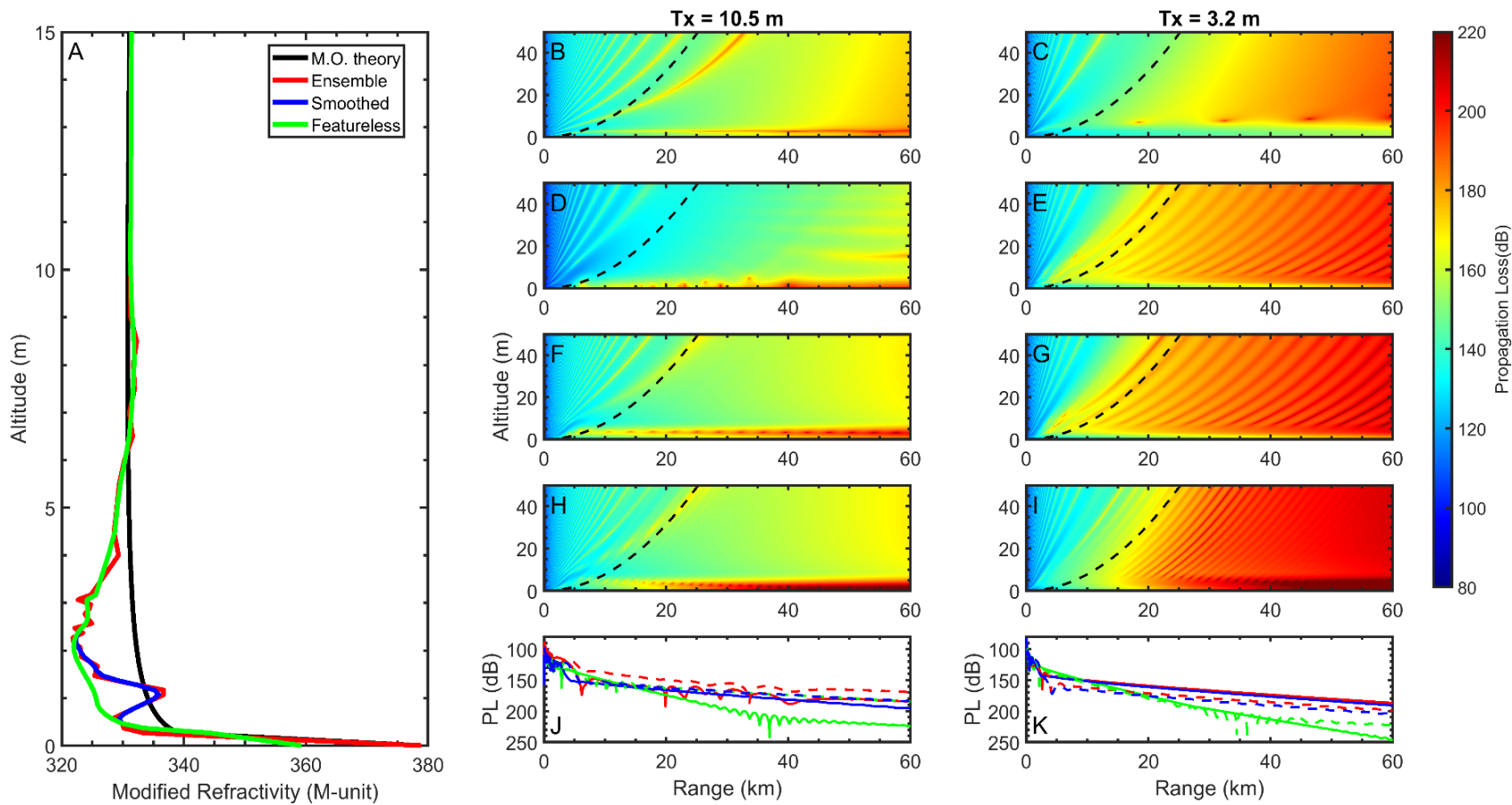
Figure 21 *Comparison of K-band PL predictions for ensemble NWIPS modified refractivity profiles with various degrees of small-scale features included in the profiles. All other aspects of the figure are as described in Figure 20 caption.*
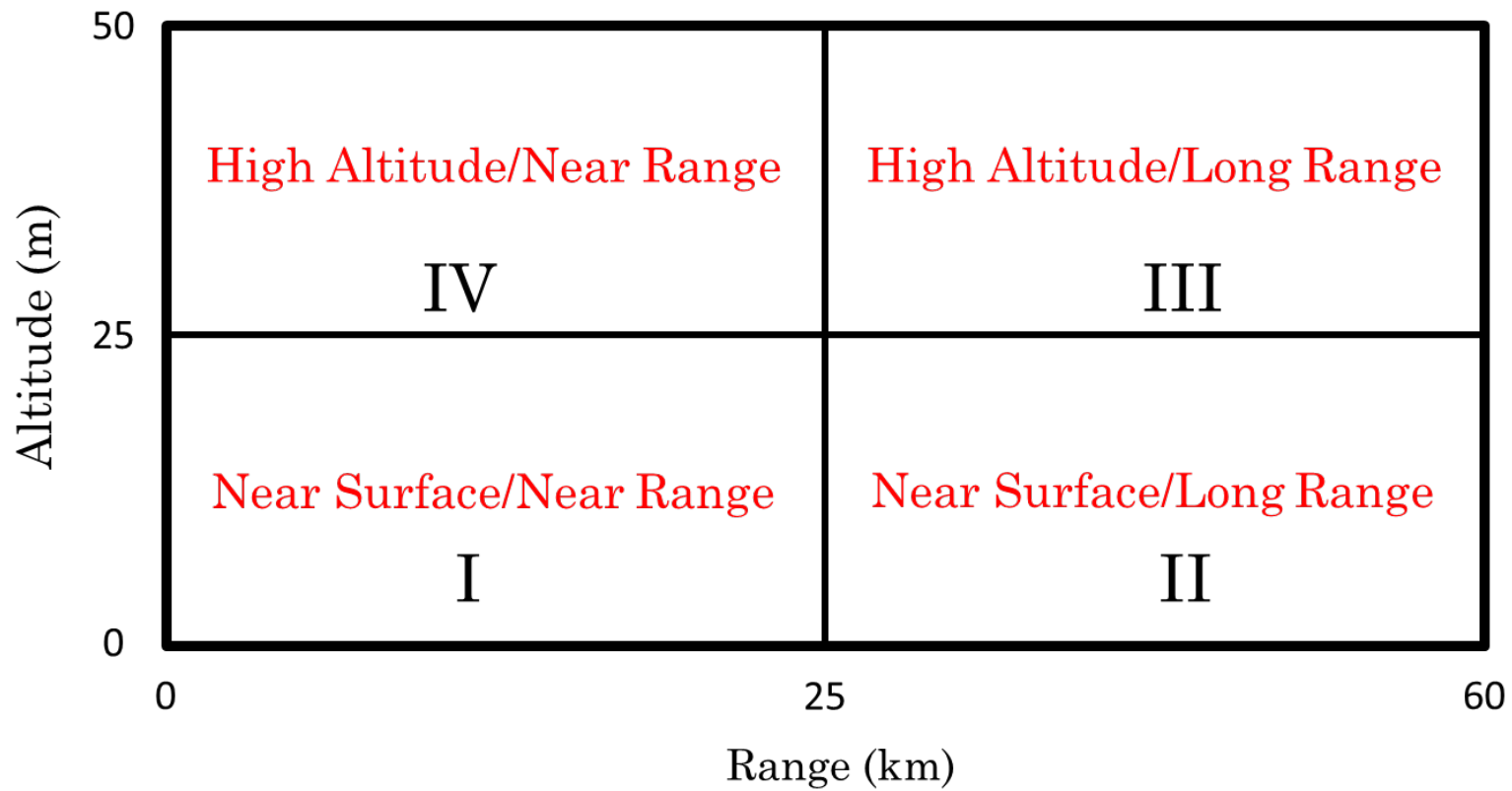
Figure 22 *Regions of interest over which mean absolute difference of PL is computed.*
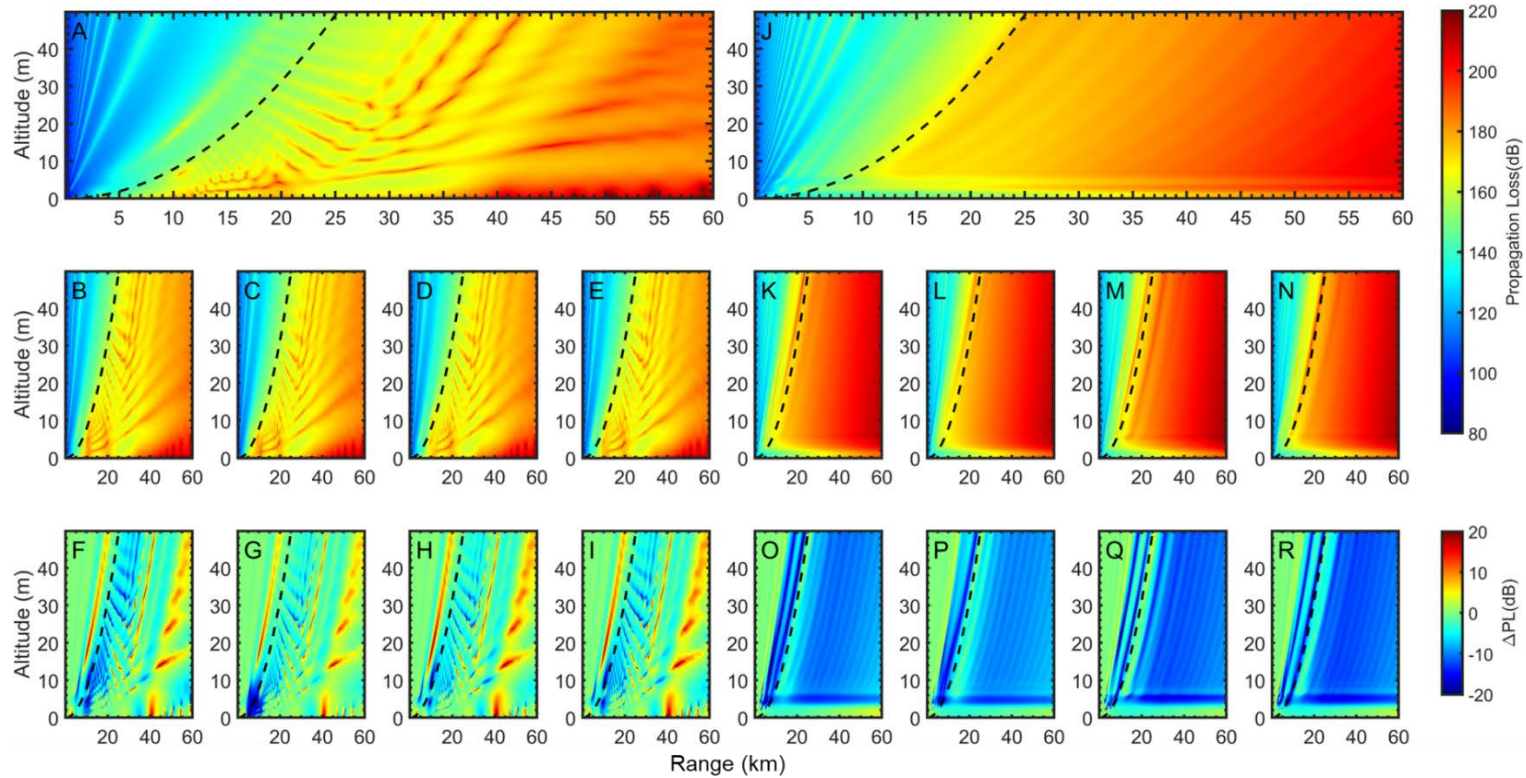
Figure 23 PL for a transmitter height of 3.2 m. Panels (A-I) show PL for X-band, whereas Panels (J-R) show PL for K-band. Panels (A,J) are PL based-on the ensemble averaged modified refractivity vertical profile (Figure 19). Panels (B-E; K-N) are the PL patterns based on the phase-averaged profiles for the crest, downslope, upslope, and trough, respectively. Panels (F-I; O-R) are differences between PL for the ensemble-average refractivity and PL for the respective wave-phase refractivity. The ordering for Panels (F-I; O-R) follows Panels (B-E; K-N).
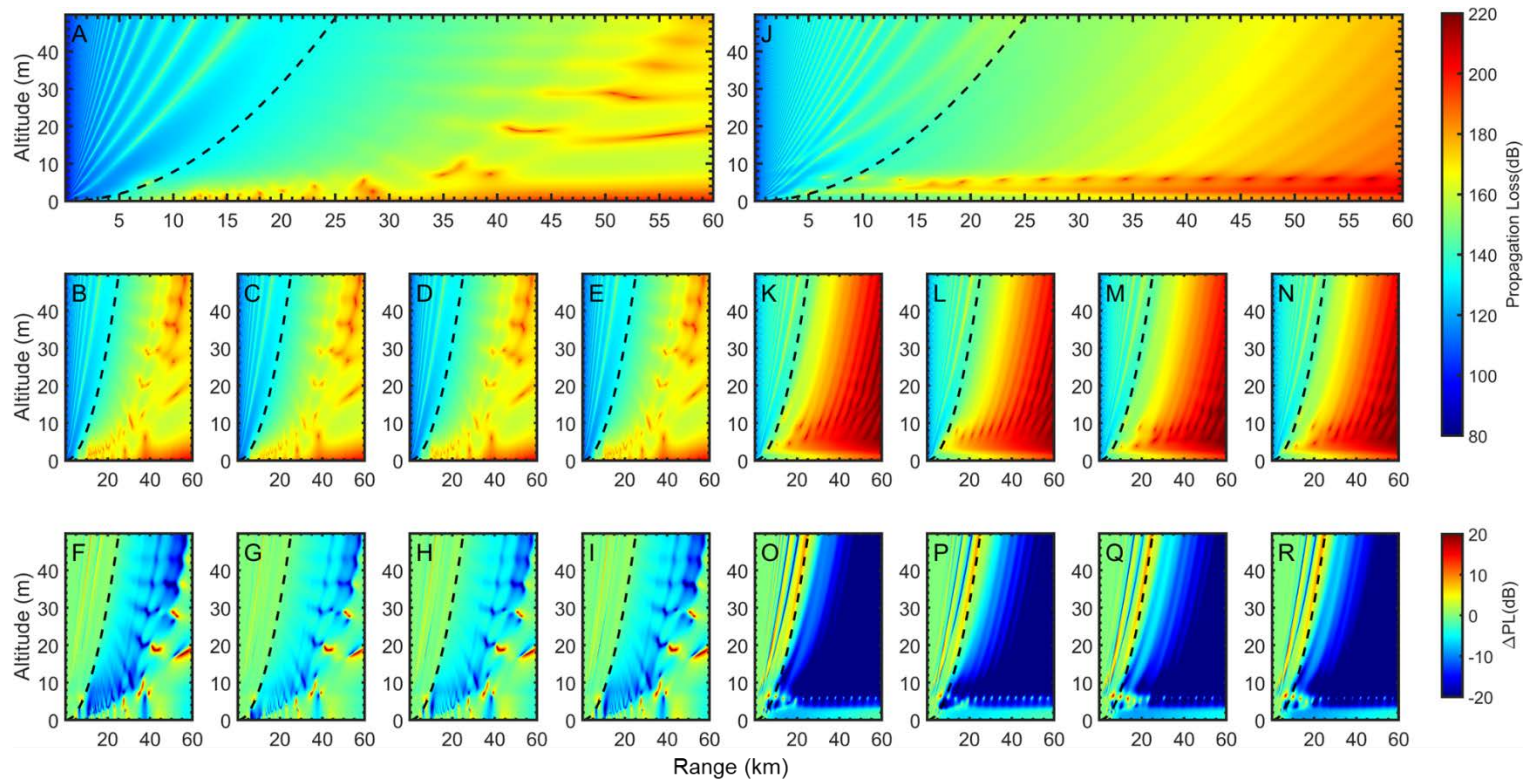
Figure 24 *PL predictions for a transmitter height of 10.5 m. All other aspects of the Figure are the same as Figure 23.*
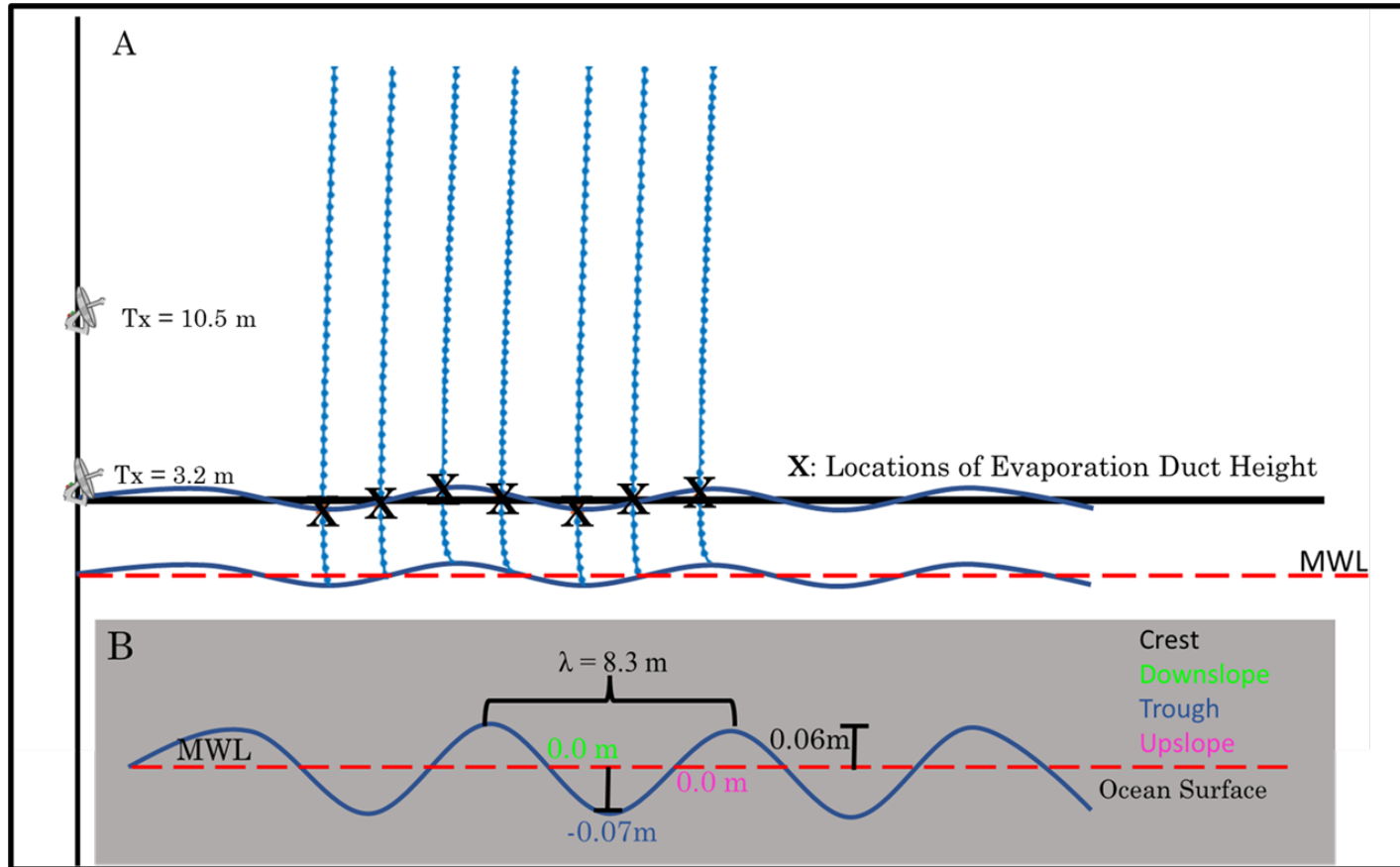
Figure 25 Simulation setup for the inhomogeneous refractivity scenario (Panel A). The phase-averaged profiles (not shown here) are spaced $\frac{1}{4}L_w$ apart over a monochromatic wavy surface as illustrated in A. Panel (B) is a zoom in of the terrain surface implemented in the simulation. Phase-averaged surface displacements relative to MWL from NWIPS are used and color coded . This setup results in the following duct height range: $3.13\ m \leq Z_d \leq 3.26\ m$.
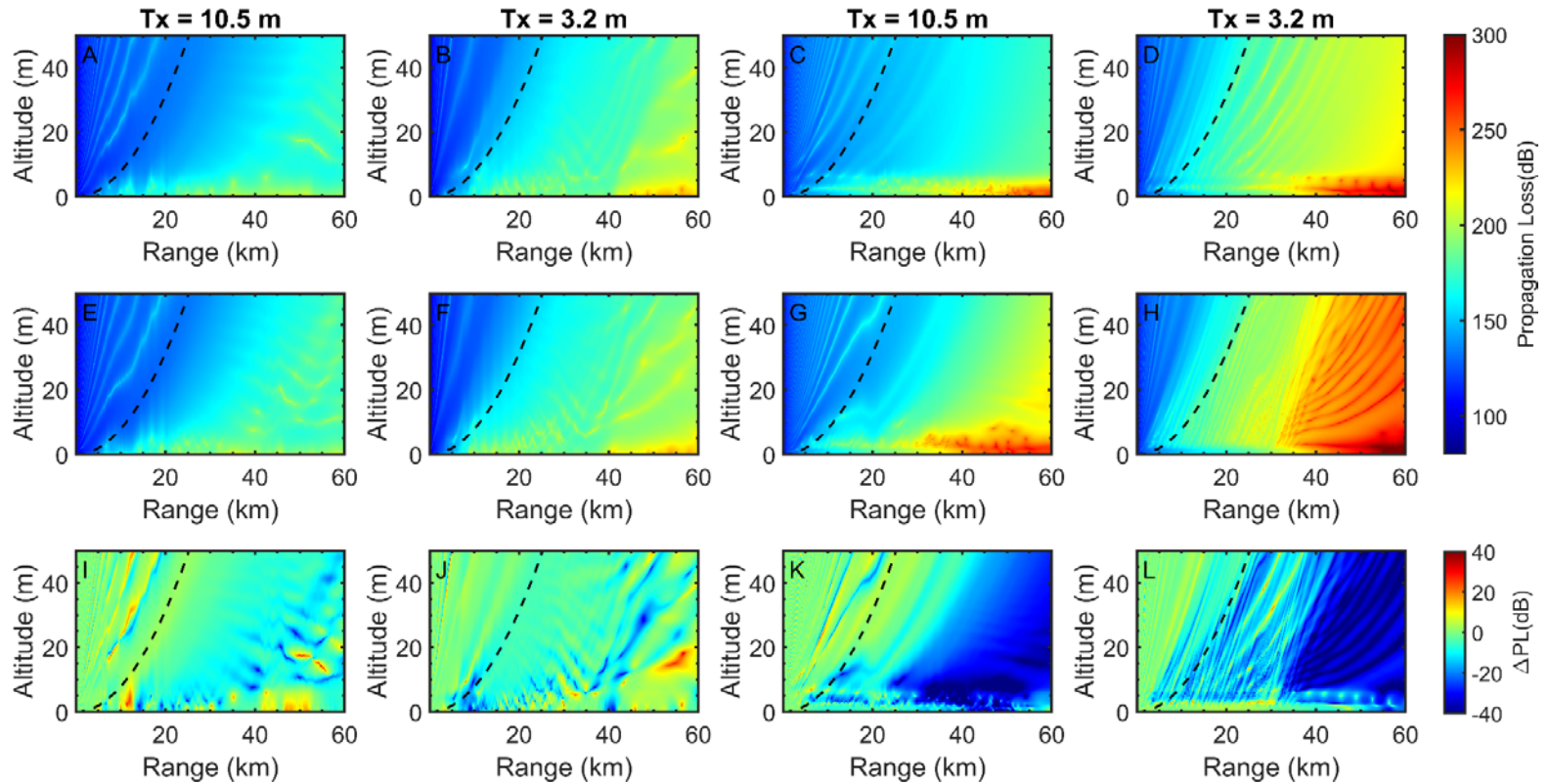
Figure 26 PL patterns for X-band and K-band at transmitter heights of 10.5 m and 3.2 m. Transmitter heights are shown above each column. X-band results are shown in the first two columns, whereas the last two columns show K-band results. Panels(A-D) represent PL for ensemble modified refractivity profiles, whereas Panels (E-H) represent wave phase-averaged profiles. The dashed black line represents the geometric horizon. Panels (I-L) show respective PL differences between ensemble and phase-averaged PL patterns. A negative value indicates PL was larger for wave phase-averaged PL compared to ensemble PL.
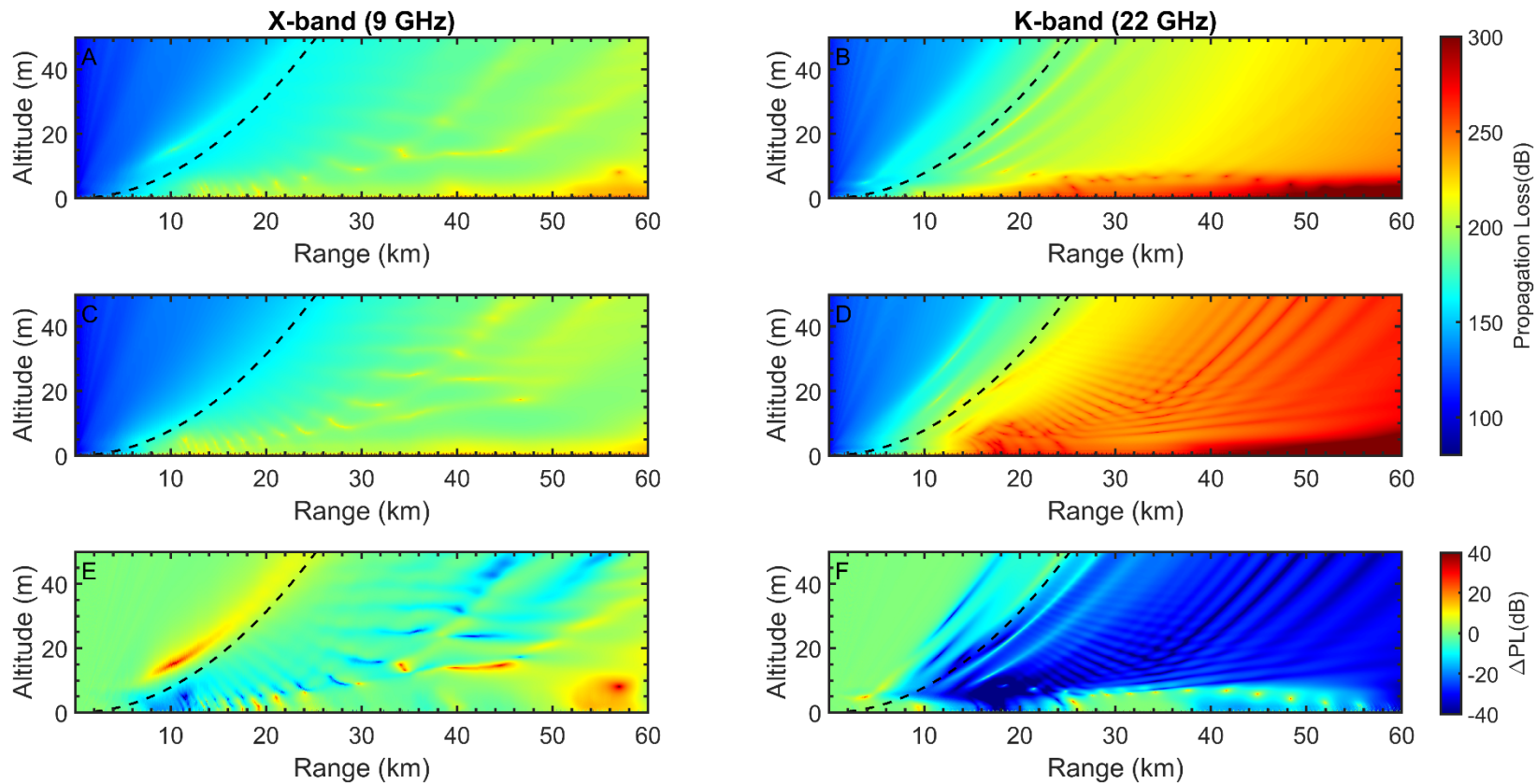
Figure 27 PL for sea state 4 scenario. Panels (A,B) correspond to NWIPS-COARE blended ensemble averaged modified refractivity, whereas Panels (C,D) correspond to NWIPS-COARE blended wave phase-averaged modified refractivity. The dashed black line corresponds to the geometric horizon. Panels (E,F) show PL difference between ensemble and phase-averaged refractivity.
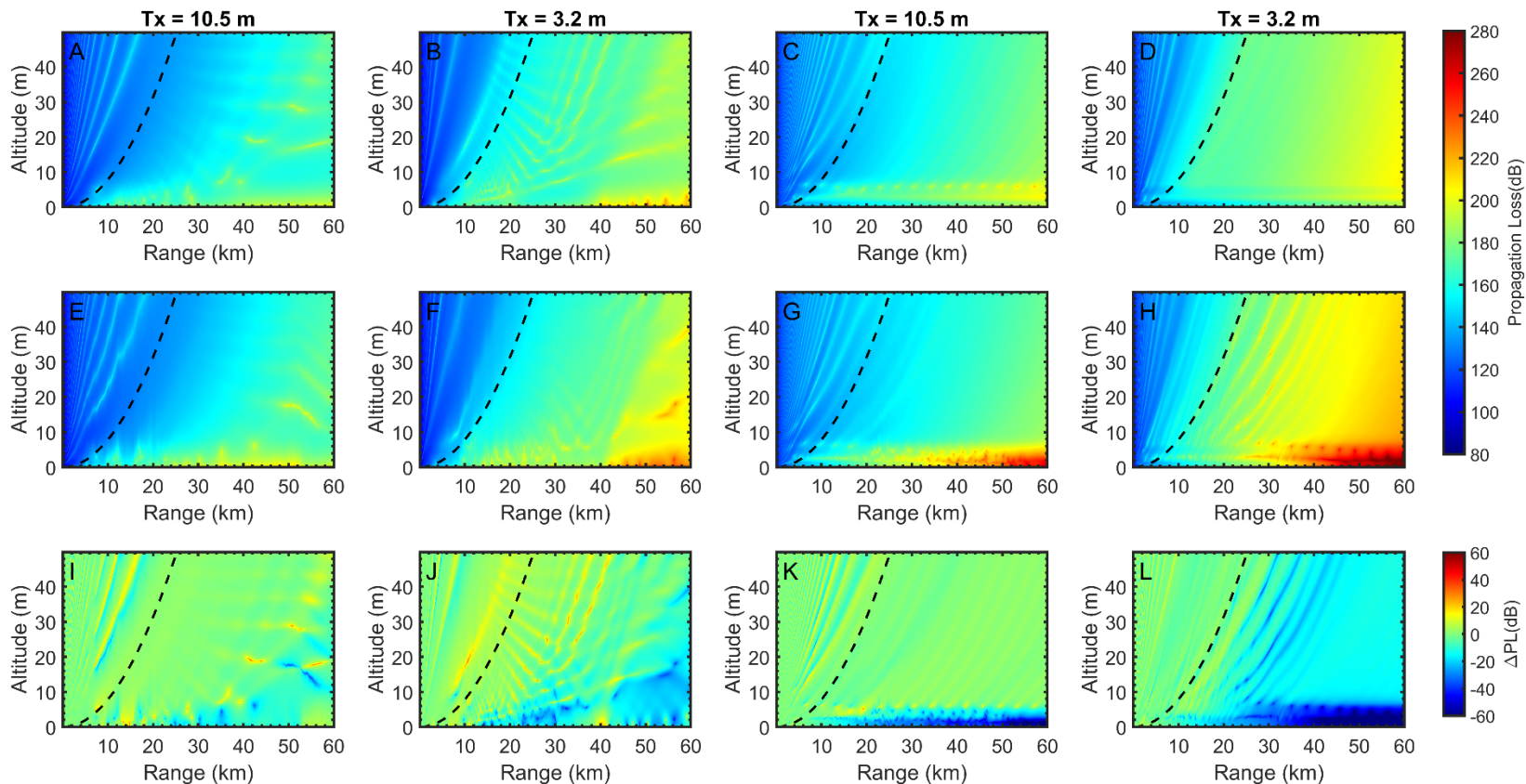
Figure 28 Comparisons of PL predictions for X-band (Panels A-B; E-F;I-J) and K-band (Panels C-D,G-H,K-J) using the NWIPS 80-minute ensemble over a smooth surface (Panels A -D) to those over the NWIPS-based wavy surface (E-H). PL differences between the two propagation predictions is shown in Panels (I-L). A negative ΔPL indicates the wavy-surface prediction resulted in larger PL. The dashed black line represents the geometric horizon. Transmitter heights are indicated above each column.

5 Summary and Conclusions

The research described in this dissertation includes the development and deployment of a measurement platform capable of high spatial and temporal sampling of temperature and humidity above the ocean surface enabling measurement of wave-coherent vertical scalar profiles within the lowest altitudes of the MASL (Chapter 2). The NWIPS consists of a 2.4 m diameter discus-type buoy with a triangular vertical mast housing 30 temperature and humidity SHT-85 sensors spaced 0.10 m apart and covering ~3 m in altitude from the sea surface (Figure 3B). In addition, NWIPS utilizes a tethered balloon for up to 4 upper altitude measurements (up to 15 m). NWIPS is oriented into the wind via two mast mounted windsocks to minimize contamination of the measurements by the buoy. A water pressure sensor is used to estimate sea surface displacement time series, and when combined with the relatively fast sampling rate of the thermodynamic sensors (1 Hz), it enables estimation of instantaneous wave-coherent vertical distributions of temperature and humidity.

Although only a short time series (80-minutes) was acquired from NWIPS in the experiment, it is the first attempt to obtain high-resolution, wave-coherent vertical measurements of temperature and humidity. NWIPS is a low-cost platform, which utilizes simple, inexpensive, and off-the-shelf sensors and electronics for the mast. The low cost of onboard sensors means that they can be replaced multiple times during a deployment as

inevitably damaged by sea spray and sea salt (DeCosmo et al., 1996). In addition, it implements lightweight and cost-effective materials allowing for easy transport and deployment from smaller vessels. Many NWIPS features attempt to address some of the shortcomings of previously implemented marine surface layer measurement platforms, for example, a lack of high vertical spatial resolution (Ortiz-Suslow et al., 2021) and measurements not extending to the sea surface (below ~0.5 m; Kang and Wang, 2016; Wang et al., 2018; Ortiz-Suslow et al., 2021).

The goal of the measurements were to investigate near-surface wave-coherent vertical scalar profiles and better understand how these distributions are influenced by ocean waves. Both ensemble and phase-averaged profiles were examined. Ten-minute ensemble averaged profiles of temperature and humidity were compared to MO theory, implemented via COARE 3.0, and time evolution of the 10-minute ensemble over the experiment was investigated. Phase-averaged temperature and humidity profiles were compared with comparably-averaged ensemble profiles, and steadiness of the phase-averaged profiles over twenty-minute time periods was presented. The high-resolution ensemble and phase-averaged vertical profiles of temperature and humidity allow study of the implications such near surface distributions have on propagation loss predictions over the marine atmospheric surface layer.

In Chapter 3, 10-minute ensemble averaged NWIPS profiles, above 4 m, showed remarkable similarity to MO theory-based profiles (Table 3). However, below 4 m, MO theory and NWIPS profiles differed due to the presence of small-scale features in the latter.

Temperature profiles showed the presence of persistent, unique, and complex structures in this near surface region, and are consistent with the development of warm/cool pockets as reported in laboratory and numerical modeling studies (Kruse and von Rohr (2006); Zhang et al. (2021); and Yang and Shen (2017)). To further understand potential sources of discrepancies between MO theory and NWIPS measurements, universal gradient functions are estimated from the data using scaling parameters for flux estimates from COARE and measured vertical gradients, and are compared to various empirical formulations from prior studies (Figure 10). This comparison is performed using NWIPS data from two altitudes – one at the classically used 10 m height, and one representing an average covering altitudes between 0.3-3.2 m. NWIPS data qualitatively agree with these empirical curves for the water vapor estimates. Water vapor universal functions based-on NWIPS data showed a consistent positive bias for the data used at the lower altitude range (below 3m) relative to the empirical curves, while data from 10 m showed reasonably good agreement. Less agreement was observed for temperature universal gradient functions with about half of the NWIPS-based estimates showing significant (order of magnitude) disagreement with empirical curves, mostly from the 10 m altitude. These results are limited by the assumption that the scaling parameters (related to turbulent fluxes) estimated from COARE are consistent with those that would be produced for the NWIPS-measured mean gradients – when this assumption breaks down discrepancies may result.

Comparisons between wave-phase averaged profiles showed profile "uniformity," – i.e., profiles were mostly similar irrespective of wave phase (Figure 14). Differences between wave-phases are primarily a consequence of the vertical shifting of the surface, thus leading

to vertical positioning differences of small-scale features as a function of wave phase. Lastly in Chapter 3, we examined steadiness of phase-averaged profiles over typical sea-state averaging time periods of 20-minutes. Here, it was shown that wave phase-averaged vertical profiles of temperature and humidity were steady over the course of the experiment (Figure 15), consistent with the similar wave conditions during the experiment. At the latter 20-minute segments, wave heights begin to increase, during which time, for temperature, some small differences are observed below 3 m – potentially indicating shifting location/intensity of hot/cold pockets during wind sea development.

Chapter 4 discusses how the observations presented in Chapter 3 can impact propagation loss predictions. Temperature and humidity profiles are used to compute modified refractivity, which are used in propagation simulations. Propagation simulations included transmitter heights: above both NWIPS and COARE (MO theory) estimated EDHs, at the COARE EDH, and at the NWIPS estimated EDH, for both X-band and K-band frequencies. EDHs from COARE and that based-on NWIPS data differed substantially at 8.5 m and 3.2 m, respectively. Under the assumption of homogeneity of refractivity over range, and over a smooth sea surface, PL predictions using COARE modified refractivity produced less PL at low altitude long range for K-band when compared to PL predictions for a 10-minute ensemble averaged NWIPS profile (blended with COARE at altitudes above 10 m) (Figure 19). X-band propagation predictions were comparatively similar for COARE and NWIPS ensemble refractivity (Figure 18).

To explore the role of small-scale features present in NWIPS but not in COARE modified refractivity, PL predictions are compared for ensemble NWIPS modified refractivity profiles with varying degrees of these small-scale features included (Figure 20). The greatest differences in PL predictions remained between COARE and any of the ensemble NWIPS; removal of the small-scale features from the NWIPS profiles did not change the PL predictions significantly for X-band. This result indicates that the differences in PL predictions between COARE and NWIPS for X-band are almost entirely driven by the different duct heights and M-deficits. K-band results did show some differences as the small-scale features of the NWIPS profile were removed; this difference in sensitivity of the PL predictions to these features could be related to differences in maximum trapping wavelength for X- and K-band (as no trapping is predicted or observed for X-band), or simply related to the smaller wavelength for K-band.

Discussion of the phase-averaged profiles included PL simulations, assuming refractivity homogeneity over range, using the 80-minute NWIPS ensemble profile and comparing it to PL predictions for 80-minute wave phase-averaged modified refractivity profiles for four phases: crest, trough, upslope, downslope (Figure 23 and 24). It was shown that for X-band PL differences between wave phase-averaged and ensemble averaged refractivity were generally below 10 dB and close to the typical measurement accuracy of 5 dB (Goldhirsh and Dockery, 1998; Table 5), indicating that these differences are negligible. In contrast, K-band results showed that the ensemble and phase-averaged refractivity can cause differences in PL at long range, with the largest discrepancies observed for the lower transmitter height (3.2 m).

This analysis was extended by investigating a heterogeneous refractivity scenario in which wave phase-averaged profiles were coupled to a sinusoidal terrain with prescribed water properties (i.e., temperature and salinity), and compared with a homogenous refractivity scenario using the 80-minute ensemble over the same surface. This comparison revealed that propagation predictions do not differ between the two scenarios for X-band, but do for K-band at long range. The different small-scale features of the profile for each phase resulted in differences in PL predictions, consistent with the prior finding that the small-scale features impact K-band propagation predictions. These results are confirmed and found to be similar in magnitude when using a larger sea surface displacement for the terrain – further indicating that these differences result from small-scale features of the modified refractivity rather than general vertical shifting of the profiles. Comparison of propagation predictions using the NWIPS 80-minute ensemble refractivity over a smooth surface to that over the wavy surface (with shifting evaporation duct height over range; Figure 28) demonstrates that vertical shifting of the duct height (and/or introduction of a wavy surface at the bottom boundary) causes larger differences in propagation predictions than the observed differences in refractivity with wave phase.

Overall, these dissertation results provide critical information regarding how to more accurately model evaporation ducts over phase-resolved ocean surfaces at low altitudes. One of the most unique aspects of the NWIPS measurements is their high vertical resolution with coverage to altitudes below 0.5 m. These high-resolution low altitude measurements revealed the presence of considerable structure in both the mean temperature and humidity fields just above the ocean surface. As previously mentioned, such structure

has never been directly measured but is consistent with LES simulations (Wagner et al., 2011) and laboratory studies (Kruse and von Rohr, 2006) of wind over waves. It was demonstrated that commonly used bulk surface layer models, such as COARE, do not account for such structure when used to extrapolate measurements to the surface for the purposes of propagation simulations. PL simulations at K-band were demonstrated to be sensitive to such small-scale structure near the ocean surface indicating that prediction errors could occur when using COARE extrapolated profiles over rough ocean surfaces. In contrast, these structures were shown to have relatively little influence on X-band propagation predictions. It was also shown that vertical refractivity profiles do not vary significantly with wave phase and linear extrapolation of the mean refractivity between the wave crest and trough in propagation simulations is reasonable for these sea states. While similar, phase-averaged profiles did shift relative to mean sea level in-phase with the surface undulation. This result implies that certain features of the profile, such as the duct height, varies over range due to the undulation of the sea surface. Not accounting for this effect in propagation simulations was shown to generate non-negligible differences in propagation predictions.

Although these measurements were able to provide these aforementioned new insights, there are some limitations and important gaps remaining. First and foremost, the data collected in this study are very limited in duration and location. As discussed in this dissertation, there are many measurement challenges associated with making direct measurements in this region, thus, even these short duration measurements at one location are helpful. But, many more measurements under a much wider range of conditions are

needed to validate many of the conclusions drawn in this research. Furthermore, more information regarding conditions not observed are important to capture. For example, the sea states in this study were not large enough, nor duct heights low enough, to examine what occurs when the wave height exceeds the duct height. This situation in particular warrants further examination and study. Additionally, further study on how the observed low altitude small-scale structure varies with atmospheric stability and wave conditions is also paramount.

6 References

Alappattu, D., Wang, Q., Yamaguchi, R., Lind, R., Reynolds, M., Christman, A. 2017. Warm layer and cool skin corrections for bulk water temperature measurements for air-sea interaction studies. *Journal of Geophysics Research* 122: 6470-6481.

Anderson, K., Brooks, B., Caffrey, P., Clarke, A., Cohen, L., Crahan, K., Davidson, K., De Jong, A., De Leeuw, G., Dion, D., Doss-Hamel, S., Fredrickson, P., Friehe, C., Hristov, T., Khelif, D., Moerman, M., Reid, J., Reising, S., Smith, M., Terrill, E., and Tsintikidis, D. 2004. The RED Experiment: an assessment of boundary layer effects in a trade winds regime on microwave and infrared propagation over the sea. *Bulletin of the American Meteorological Society* 85(9): 1355-1365.

Babin, S. and Dockery, G. 2002. LKB-based evaporation duct model comparison with buoy data. *Journal of Applied Meteorology* 41(4): 434-446.

Babin, S., Young, G., and Carton, A. 1997. A new model of the oceanic evaporation duct. *Journal of Applied Meteorology* 36: 193-204.

Banner, M. and Melville, W. 1976. On the separation of air flow above water waves. *Journal of Fluid Mechanics* 77: 825-842.

Bean, B. and Dutton, E. 1968. Radio Meteorology. *Dover Publications*.

Belcher, S. and Hunt, J. 1998. Turbulent flow over hills and waves. *Annual Review of Fluid Mechanics* 30: 507-538.

Bhat, G. 2003. Measurement of air-sea fluxes over the Indian Ocean and the Bay of Bengal. *Journal of Climate* 16(4): 767-775.

Bourassa, M., Vincent, D., and Wood, W. 1999. A flux parameterization including the effects of capillary waves and sea state. *Journal of the Atmospheric Sciences* 56(9):1123 – 1139.

Bradley, E., Coppin, P., and Godfrey, J. 1991. Measurements of sensible and latent heat flux in the western Equatorial Pacific Ocean. *Journal of Geophysical Research* 96: 3375-3389.

Brumer, S., Zappa, C., Brooks, I., Tamura, H., Brown, S., Blomquist, B., Fairall, C., Cifuentes-Lorenzen, A. 2017. Whitecap coverage dependence on wind and wave statistics observed during SO GasEX and HiWinGS. *Journal of Physical of Oceanography* 47: 2211–2235.

Brutsaert, W. 1982. Evaporation into the atmosphere. Reidel, Dordecht, p. 299.

Buck., A. 1981. New equations for computing vapor pressure and enhancement factor. *Journal of Applied Meteorology* 20(12): 1527-1532.

Buckley, M. and Veron, F. 2019. The turbulent airflow over wind generated surface waves. *European Journal of Mechanics, B/ Fluids* 73: 132-143.

Businger, J. 1973. Turbulent transfer in the atmospheric surface layer, in workshop on Micrometeorology, ed. By D. Haugen, *American Meteorology Society,* Boston, 67-100.

Businger, J., Wyngaard, J., Izumi, Y., and Bradley, F. 1971.Flux-profile relationships in the atmospheric surface layer. *Journal of the Atmospheric Sciences* 28:181-189.

Chaffin, J., Bell, W., and Teng, C. 1992. Development of NDBC's Wave Processing Module. Proceedings of MTS 92, MTS, Washington, D.C. p. 966-970.

Charnock, H. 1955. Wind stress on a water surface. *Quarterly Journal of the Royal Meteorological Society* 81: 639-640.

Cherret, R. 2015. Capturing characteristics of atmospheric refractivity using observations and modeling approaches. *Dissertation – Naval Postgraduate School,* Monterey, CA.

Craig, K. and Levy, M. 1991. Parabolic equation modeling of the effects of multipath and ducting on radar systems. *Institute of Electrical and Electronics Engineers Proceedings, Part F* 138(2): 153-162.

Cronin, M., Gentemann, C., Edson, J., Ueki, I., Bourassa, M., Brown, S., Clayson, C., Fairall, C., Fararr, J., Gille, S., Gulev, S., Josey, S., Kato, S., Katsumata, M., Kent, E., Krug, M., Minnett, P., Parfitt, R., Pinker, R., Stackhouse, P., Swart, S., Tomita, H., Vandemark, D., Weller, R., Yoneyama, K., Yu, L, and Zhang, D. 2019. Air-sea fluxes with a focus on heat and momentum. *Frontiers in Marine Science* 6: 430.

Davidson, K., Guest, P., Mabey, D., Fredrickson, P., and Anderson, A. 2003. The use of kite observations to study air-sea interaction-controlled atmospheric surface layer profiles during the RED experiment. *12th Conference on Interactions of the Sea and Atmosphere* Long Beach, CA. 10-13 February, 2003.

DeCosmo, J., Katsaros, K., Smith, S., Anderson, R., Oost, W., Bumke, K., Chadwick, H. 1996. Air-sea exchange of water vapor and sensible heat: the humidity exchange over the sea (HEXOS) results. *Journal of Geophysical Research C: Oceans* 101(c5): 12001-12016.

Donelan, M., Babanin, A., Young, I., and Banner, M. 2006. Wave-follower field measurements of the wind-input spectral function. Part II: parametrization of the wind input. *Journal of Physical Oceanography* 36: 1672-1689.

Drennan, W. 2006. On parameterizations of air-sea fluxes. WIT Transactions on State of the Art in Science and Engineering. Vol. 23. WIT Press.

Ducrozet, G., Bonnefoy, F., Le Touze, D., and Ferrant, P. 2007. 3-D HOS simulations of extreme waves in open seas. *Natural Hazards Earth Systems Science* 7: 109-122.

Dyer, A. 1974. A review of flux-profile relationships. *Boundary Layer Meteorology* 7: 363-372.

Dyer, A. and Bradley, E. 1982. An alternative analysis of flux-gradient relationships at the 1976 ITCE. *Boundary Layer Meteorology* 22: 3-19.

Dyer, A. and Hicks, B. 1970. Flux-gradient relationships in the constant flux layer. *Quarterly Journal of the Royal Meteorological Society* 96: 715-721.

Earle., M. 1996. Nondirectional and directional wave data analysis procedures. NDBC Technical Document 96-01. Stennis Space Center, MS.

Fairall, C, Bradley, E. and Hare, J. 2003. Bulk parameterization of air-sea fluxes: updates and verification for the COARE algorithm. *Journal of Climate* 16(4): 571-591.

Fairall, C. and Edson, J. 1994. Recent measurements of the dimensionless turbulent kinetic energy dissipation function over the ocean, paper presented at the Second Int. Conf. on Air-Sea Interaction and Meteorology and Oceanography of the Coastal Zone, *American Meteorological Society.,* Lisbon, Portugal, Sept. 22-27.

Fairall, C., Bradley, E., Rogers, D., Edson, J. and Young, G. 1996. Bulk parametrization of air-sea fluxes for Tropical Ocean and Global Atmosphere Coupled Ocean – Atmosphere Response Experiment. *Journal of Geophysical Research* 101: 3747-3764.

Fang, P., Zhao, B., Zeng, Z., Yu, H., Lei, X., and Tan, J. 2018. Effects of wind direction on variations in friction velocity with wind speed under conditions of strong onshore wind. *Journal of Geophysical Research - Atmospheres* 123: 7340–7353.

Francis, O., Atkinson, D. 2012. Synoptic forcing of waves states in the southeast Chukchi Sea, Alaska, at an offshore location. *Natural Hazards* 62: 1169-1186.

Fredrickson, P. 2015. Software design describing for the Navy Atmospheric Vertical Surface Layer Model (NAVSLaM). Version 1.1. Prepared for the Naval Oceanographic Office. *Systems Integration Division.*

Garbe , C., Rutgersson, A., Boutin, J., de Leeuw, G., and et al. 2013. Transfer across the air-sea interface. In Liss, P. and Johnson, M. (eds) Ocean-atmosphere interactions of gases and particles. *Springer.*

Garratt, J. 1992. The Atmospheric Boundary Layer. *Cambridge University Press.*

Garratt, J., 1977. Review of drag coefficients over oceans and continents. *Monthly Weather Review* 105: 915-929.

Geernaert, G., Larsen, S., and Hansen, F. 1987. Measurements of the wind stress, heat flux, and turbulence intensity during storm conditions over the North Sea. *Journal of Geophysical Research* 92(c12): 13127-13139.

Gerbi, G., Trowbridge, J.,Edson, J., Plueddemann, E., Terray, E., and Fredricks, J. 2008. Measurements of momentum and heat transfer across the air–sea interface. *Journal of Physical Oceanography* 38: 1054-1072.

Gill, G. 1983. Comparison testing of selected naturally ventilated solar radiations shields. NOAA Data Buoy Office Report, Contract NA-82–0A-A-266; NOAA: Bay St. Louis, MS, USA.

Godfrey, J. and Beljaars, A. 1991. On the turbulent fluxes of the buoyancy and moisture at the air-sea interface at low wind speeds. *Journal of Geophysical Research* 96(C12): 0-5.

Goldhirsh, J., and Dockery, G. 1998. Propagation factor errors due to the assumption of lateral homogeneity. *Radio Science* 33(2): 239– 249.

Grachev, A. and Fairrall, C. 1996. Dependence of the Monin-Obuhkov stability parameter on the bulk Richardson number over the ocean. *Journal of Applied Meteorology and Climatology* 36 (4): 406-414.

Hackett, E., Luznik, L., Nayak, A., Katz, J., and Osborn, T. 2011. Field measurements of turbulence at an unstable interface between current and wave Bottom Boundary Layers. *Journal of Geophysical Research* 116. C02022.

Hanafusa, T. 1971. A new method of on-site data analysis of turbulent transports near the ground. *Contributions of the Geophysical Institute – Kyoto University* 11: 35 -45.

Hasse, L. 1963. On the determination of the vertical transports of momentum and heat in the atmospheric boundary layer at sea. *Department of Oceanography, Oregon State University.*

Hasse, L. 1971. The sea-surface temperature deviation and the heat flow at the sea-air interface. *Boundary Layer Meteorology* 1: 368-379.

Hogstrom, U. 1988. Nondimensional wind and temperature profiles in the atmospheric surface layer: a re-evaluation. *Boundary Layer Meteorology* 42: 55-78.

Janssen, P. 2004. The Interaction of Ocean Waves and Wind. Cambridge University Press.

Jiang, Q. 2020. Influence of swell on marine surface-layer structure. *Journal of Atmospheric Sciences* 77(5): 1865-1885.

Jiang, Q. and Wang, Q. 2021. Characteristics and Scaling of the stable marine internal boundary layer. *Journal of Geophysical Research – Atmospheres* 126 (21): e2021JD035510.

Kang, D. and Wang, Q. 2016. Optimized estimation of surface layer characteristics from profiling measurements. *Atmosphere* 7 (14).

Karimian, A., Yardim, C., Haack, T., Gerstoft, P., Hodgkiss, W., and Rogers, T. (2013). Toward the assimilation of the atmospheric surface layer using numerical weather prediction and radar clutter observations. *Journal of Applied Meteorology and Climatology* 52 (10): 2345–2355.

Katz, J. and Zhu, P. 2017. Evaluation of surface layer flux parameterizations using *in-situ* observations. *Atmospheric Research* 194: 150–163.

Kerr, D. 1951. *Propagation of Short Radio Waves.* New York, NY, USA: McGraw-Hill, p. 20.

Kharif, C., Giovanangeli, J., Touboul, J., Grare, L., and Pelinovsky. 2008. Influence of wind on extreme wave events: experimental and numerical approaches. *Journal of Fluid Mechanics* 594: 209-247.

Kitaigorodsky, S. and Volkov, Y., 1965. On the roughness parameters of the sea surface. *izv. Acad. Sc. U.S.S.R. Atmospheric and Oceanic Physics.,* 1, English Translation p. 973-988.

Kondo, J. 1975. Air-sea bulk transfer coefficients in diabetic conditions. *Boundary Layer Meteorology* 9: 91-112.

Kruse, N. and von Rohr, P., 2006. Structure of turbulent heat flux in a flow over a heated wavy wall. *International Journal of Heat and Mass Transfer* 49: 3514-3529.

Kuhn, S. and von Rohr, P. 2008. Experimental investigation of mixed convective flow over a wavy wall. *International Journal of Heat and Fluid Flow* 29 (1): 94-106.

Lang, N. 1987. The empirical determination of a noise function for NDBC buoys with strapped-down accelerometers. Proceedings of OCEANS 87, IEEE, New York, NY, p. 225-228.

Lentini, N. and Hackett, E. 2015. Global sensitivity of parabolic equation radar wave propagation simulation to sea-state and atmospheric refractivity structure. *Radio Science* 50(10): 1027-1049.

Li, Q., Bou-Zeid, E., Vercauteren, N., and Parlange, M. 2018. Signatures of air-wave interactions over a large lake. *Boundary Layer Meteorology* 167: 445–468.

Magnavox, 1986, Amendment no. 1 to the technical manual for Data Acquisition and Telemetry (DACT)," Magnavox Electronics Systems Co., Fort Wayne, IN, 26 pp.

McKenna, S. and McGillis, W. 2004. The role of free-surface turbulence and surfactants in air-water gas transfer. *International Journal of Heat Mass Transfer* 47: 539-553.

Miller, A. and Street, R. 1978. On the existence of temperature waves at a wavy air-water interface. *Journal of Geophysics Research* 83: 1353-1365.

Mueller, J. and Veron, F. 2010. Bulk formulation of the heat and water vapor fluxes at the air-sea interface, including nonmolecular contributions. *Journal of Atmospheric Science* 67(1): 234-247.

Mueller, J. and Veron, F. 2014. Impact of sea spray on air-sea fluxes. part II: feedback effects. *Journal of Physical Oceanography* 44(11): 2835-2853.

Newgard, J. and Hay, A. 2007. Turbulence intensity in the wave boundary layer and bottom friction under (mainly) flat bed conditions. *Journal of Geophysical Research* 112(c9).

Ohlmann, J. and Siegel, D. 2000. Ocean radiant heating. Part II: parametrizing solar radiation transmission through the upper ocean. *American Meteorological Society* 30: 1849-1865.

Okuda, K. 1982. Internal flow structure of short wind waves. part I. on the internal velocity structure. *Journal of the Oceanographic Society of Japan* 38: 28-42.

Oncley, S., Friehe, C., LaRue, J., Businger, J., Itsweire, E., and Chang, S. 1996. Surface-layer fluxes, profiles, and turbulence measurements over uniform terrain under near-neutral conditions. *Journal of Atmospheric Science* 53: 1029-1044.

Oost, W., Komen, G., Jacobs, C., and van Wort, C. 2001. New evidence for a relation between wind stress and wave age from measurements during ASGAMAGE. *Technical report 2001-5, Royal Dutch Meteorological Institute (KNMI),* The Netherlands.

Ortiz-Suslow, D., Kalogiros, J., Yamaguchi, R., and Wang, Q.2021. An evaluation of the constant flux layer in the atmospheric flow above the wavy air-sea interface. *Journal of Geophysical Research – Atmospheres* 26: 2834.

Pastore, D., Greenway, P., Stanek, M., Wessinger, S., Haack, T., Wang, Q., and Hackett, E. 2021. Comparison of atmospheric refractivity estimation methods and their influence on radar propagation predictions. *Radio Science* 56: e2020RS007244.

Paulus, R. 1990. Evaporation duct effects on sea clutter. *Institute of Electrical and Electronics Engineers Transactions on Antennas and Propagation* 38(11): 1765-1771.

Phillips, W. and Wu, Z. 1994. On the instability of wave-catalysed longitudinal vortices in strong shear. *Journal of Fluid Mechanics* 272:235–254.

Reul, N., Branger, H., and Giovanangeli. 1999. Air flow separation over unsteady breaking waves. *Physics of Fluids* 11(7): 1959-1961.

Reul, N., Branger, H., and Giovanangeli, J. 2008. Air flow structure over short-gravity breaking waves. *Boundary Layer Meteorology* 126: 477-505.

Rutgersson, A., Smedman, A., and Hogstrom, U. 2001. Use of conventional stability parameters during swell. *Journal of Geophysical Research* 106(c11): 27117-27134.

Ryan, F. 1991. Analysis of electromagnetic propagation over variable terrain using the parabolic wave equation. No NOSC/TR-1453 *Naval Ocean Systems Center,* San Diego, California.

Saunders, P. 1967. The temperature of the ocean-air interface. *Journal of the Atmospheric Sciences* 24: 269-273.

Schooley, A. 1975. Simple method for measuring relative humidity, water, and air temperatures within a few millimeters of wind-generated water waves. *Journal of Physical Oceanography* 5(3): 519-522.

Shabani, B., Nielsen, P., and Baldock, T. 2014. Direct measurements of wind stress over the surf zone. *Journal of Geophysical Research – Ocean* 119: 2949–2973.

Shi, Y., Yang, K., Yang, Y., and Ma, Y., 2015a. Experimental verification of effect of horizontal inhomogeneity of evaporation duct on electromagnetic wave propagation. *Chinese Physics B*, 24 (4): 044102.

Shi, Y., Yang, K., Yang, Y., and Ma, Y. 2015b. Influence of obstacle on electromagnetic wave propagation in evaporation duct with experiment verification. *Chinese Physics B* 24(5): 6.

Sirkova, I. 2012. Brief review on PE method application to propagation channel modeling in sea environment. *Open Engineering* 2(1): 19-38.

Skolnik, M. 2001. Introduction to Radar Systems. McGraw Hill, New York, NY.

Smith, S. 1989. Water vapor flux at the sea surface. *Boundary Layer Meteorology* 47: 277-293.

Smith, S., 1988. Coefficients for sea surface wind stress, heat flux, and wind profiles as a function of wind speed and temperature. *Journal of Geophysical Research* 93 (15): 467-472.

Sobey, R., 1992. The distribution of zero-crossing wave heights and periods in a stationary sea state. *Ocean Engineering* 19 (2): 101-118.

Soloviev, A. and Schlüssel, P. 1994. Parametrization of the cool skin of the ocean and of the air-ocean gas transfer on the basis of modelling surface renewal. *Journal of Physical Oceanography* 24(6): 1339-1346.

Soloviev, A. and Schlüssel, P. 1996. Evolution of cool skin and direct air-sea gas transfer coefficient during daytime. *Boundary Layer Meteorology* 77: 45-68.

Stanek, M. 2018. Characterization of a turbulent boundary layer in open channel flow using particle image velocimetry. Masters - Thesis, Coastal Carolina University.

Stanek, M. and Hackett, E. 2021. Towards obtaining high-resolution vertical distributions of temperature and humidity near the ocean surface: a low-cost platform design. In Proceedings of the 7th Young Coastal Scientists and Engineers Conference—Americas, Myrtle Beach, SC, USA, 29–31 October 2021.

Stanek, M., Pastore, D., Wessinger, S., Hackett, E. 2021. Near-surface vertical distributions of temperature and humidity in the marine atmospheric surface layer. American Geophysical Union Conference – New Orleans, LA, USA, 12 – 17 December 2021.

Stanek, M., Pastore, D., and Hackett, E. 2023. A novel near-surface wave-coherent instantaneous profiling system for atmospheric measurements. *Sensors 23. 4099.*

Steele, K. and Earle, M. 1991, Directional ocean wave spectra using buoy azimuth, pitch, and roll derived from magnetic field components. *Journal of Oceanic Engineering, IEEE:* 427-433.

Steele, K. and Mettlach, T. 1994. NDBC wave data - current and planned. Proceedings Ocean Wave Measurement and Analysis, WAVES 93 Symposium, ASCE, New York, NY, p. 198-207.

Steele, K., Wang, D., Teng, C., and Lang, N. 1990. Directional-wave measurements with NDBC 3-meter discus buoys. National Data Buoy Center, Stennis Space Center, MS.

Steele, K., Wolfgram, P., Trampus, A., and Graham, B. 1976. An operational high resolution wave data analyzer system for buoys. Proceedings of OCEANS 76, IEEE, New York, NY.

Sui, C., Li, X., Lau, K., and Adamec, D. 1997. Multiscale air – sea interactions during TOGA COARE. *Monthly Weather Review* 125: 448- 462.

Sullivan, P. and McWilliams, J. 2002. Turbulent flow over water waves in the presence of stratification. *Physics of Fluids* 14: 1182-1195.

Sullivan, P. and McWilliams, J. 2010. Dynamics of winds and currents coupled to surface waves. *Annual Review of Fluid Mechanics* 42: 19-42.

Sullivan, P., McWilliams, J., and Patton, E. 2014. Large-eddy simulation of marine atmospheric boundary layers above a spectrum of moving waves. *Journal of the Atmospheric Sciences* 71(11): 4001-4027.

Tanner, B. 1990. Automated weather stations. *Remote Sensing Review* 5: 73–98.

Taylor, P. and Yelland, M. 2001. The dependence of sea surface roughness on the height and steepness of the waves. *Journal of Physical Oceanography* 31: 572-590.

Tennekes, H. and Lumley., J. 1972. A First Course in Turbulence. MIT Press, Cambridge, Massachusetts.

Tian, Z. and Choi, W. 2013. Evolution of deep-water waves under wind forcing and wave breaking effects: numerical simulations and experimental assessment. *European Journal of Mechanics, B/Fluids* 41: 11-22.

Turton, J., Bennetts, D., Farmer, S. 1988. "*An Introduction to radio ducting.*" Meteorology Magazine Vol. 117, p. 245-254, January.

Veron, F., Melville, Lenain, L. 2008. Wave-coherent air-sea heat flux. *Journal of Physical Oceanography* 38(4): 788-802.

Veron, F., Melville, W., and Lenain, L. 2011. The effects of small-scale turbulence on air-sea heat flux. *Journal of Physical Oceanography* 41(1): 205-220.

Wagner, C., Kenjeres, S., and von Rohr, P. 2010. Dynamic large eddy simulations of momentum and wall heat transfer in forced convection over wavy surfaces. *Journal of Turbulence* 12 (7): 1- 27.

Wang, Q., Alappattu, D., Billingsley, S., Blomquist, B., Burkholder, R.., et al. 2018. CASPER: Coupled air–sea Processes and Electromagnetic Ducting Research. *Bulletin American Meteorological Society* 99: 1449-1471.

Webb, E. 1982. Profile relationships in the superadiabatic surface layer. *Quarterly Journal of the Royal Meteorological Society* 108(457): 661-688.

Wick, G. 1995. Evaluation of the variability and predictability of the bulk-skin SST difference with application to satellite measured SST. PhD. Dissertation. *University of Colorado.*

Wieringa, J. 1980. A reevaluation of Kansas mast influence on the measurements of stress and cup anemometer over-speed. *Boundary Layer Meteorology* 18: 411-430.

Witting, J. 1971. Effects of plane progressive irrotational waves on thermal boundary layers. *Journal of Fluid Mechanics* 50(2): 321-334.

Witting, J. 1972. Temperature fluctuations at an air-water interface caused by surface waves. *Journal of Geophysical Research* 77: 3265-3269.

Woodcock, A. 1941. Surface cooling and streaming in shallow fresh and salt waters. *Journal of Marine Resources* 4: 153-161.

World Meteorological Organization. 2011. *Manual on Codes* (WMO-NO 306), Volume I. Geneva.

Wyngaard, J., Cote, O., and Izumi, Y. 1971. Local free convection similarity and the budgets of shear and heat flux. *Journal of Atmospheric Science* 28: 1171-1182.

Yaglom, A. 1977. Comments on wind and temperature flux-profile relationships. *Boundary Layer Meteorology* 11: 89-102.

Yang, D. and Shen, L. 2017. Direct numerical simulation of scalar transport in turbulent flows over progressive surface waves. *Journal of Fluid Mechanics* 819: 58-103.

Yang, S., Li, X., Wu, C., He, X., and Zhong, Y., 2017. Application of the PJ and NPS evaporation duct models over the South China Sea (SCS) in winter. *PLoS One* 12(3): e0172284.

Zhang, E., Wang, X., and Liu, Q. 2021. Numerical investigation on the temporal and spatial statistical characteristics of turbulent mas transfer above a two-dimensional wavy wall. *International Journal of Heat and Mass Transfer* 184: 122260.

Zhao, Z.-K., Liu, C., Li, Q., Dai, G., Song, Q., and Lv, W. 2015. Typhoon air-sea drag coefficient in coastal regions. *Journal of Geophysical Research – Ocean* 120: 716–727.

Zhuang, H., Yang, X., and Wu, Z. 2018. A parameterization scheme for air-sea surface interface design and stand-alone. *Journal of the Atmospheric Sciences* 75 (7): 2359-2383.